博士論文

Investigation on MCCI phenomena with multi-physics MPS simulation model

(MPS 解析モデルによる MCCI 現象に関する研究)

柴鵬輝

Investigation on MCCI phenomena with multi-physics MPS simulation model

A dissertation submitted to

The University of Tokyo

In partial fulfillment of the requirements

For the degree of

Doctor of Philosophy

In

NUCLEAR ENGINEERING AND MANAGEMENT

By

Penghui Chai

July 201

Contents

Acronyms

Symbol	Description
α	Thermal diffusive
β	Thermal expansion coefficient
ϕ	Scalar
ρ	Density
υ	Dynamic viscosity
ω	Weight function
λ	Laplacian coefficient
C	Surface tension coefficient
C_p	Specific heat
C_{ps}	Specific heat in solid condition
C_{pl}	Specific heat in liquid condition
d	Space dimension's number
D	Diffusion coefficient
F	Source term of momentum equation
h	Enthalpy
h_s	Enthalpy in solidus temperature
h_l	Enthalpy in liquidus temperature
K	Thermal conductivity
m	Mass
M	Molar mass
N	Amount
P	Pressure
q	Thermal release from the redox reaction
Q	Source term of energy equation
Ra	Rayleigh number
T	Temperature
T_s	Solidus temperature
T_l	Liquidus temperature
t	Time
u	Velocity
$\boldsymbol{u}$	Vector parameter
W	Weight fraction
V	Volume
Total_corium	The total amount of corium particles

Total_crust   The total amount of crust particles
Total_melt   The total amount of initial corium particles

Figure list

Table list

1. Introduction

1.1. Molten Core-Concrete Interaction

1.1.1. General introduction of MCCI

During a core melt severe accident with subsequent failure of the pressure vessel, the molten core materials would discharged into the reactor cavity at the bottom and interact with the concrete. Due to the high temperature and the decay heat of the corium, the concrete wall in the reactor pit would be gradually ablated and threaten the integrity of the containment.

MCCI (Molten Core-Concrete Interaction) process and the consequences are of essential importance for the safety analyses of existing Gen II reactors. Besides, MCCI process defines the initial condition and boundary condition to control the molten materials in different core retention concepts, and it's very important for the Gen III reactors development. There is a new retention concept in EPR, for example, where a temporary retention channel is utilized[1].

Molten materials consist of uranium dioxide in the fuel, zirconium in the fuel rod cladding and carbon steel and stainless steel in other structures. Take a typical commercial reactor of 1300 MW as an example, there are about 120 t of oxides (UO_2, ZrO_2 .) and 80 t of metal (Fe, Cr, Ni, Zr) in the corium. The corium would be heated up by the decay heat, which is generated in the oxide fraction of the corium. It may lead to the melt-through of the base mat over a period of several days, depend on the geometry conditions. Besides, the release of steam, hydrogen and other non-condensable gases from concrete decomposition increases the containment pressure and may also result in the accumulation of flammable hydrogen concentrations, with the possible consequence of containment over-pressurization. In another word, even when the mitigation measurements are effective, the melt may

result in catastrophic large fission product release and land contamination due to containment failure. Therefore, it is essential important that the gas generation and ablation behaviors of MCCI be studied.

1.1.2.Phenomenology

The MCCI process can be depicted by Figure 1-1. Generally, the main issues with MCCI during severe accident conditions are 1) concrete ablation, 2) gas generation, 3) chemical reaction between the melt pool and concrete 4) possible stratification between the metallic and oxide in the melt pool and 5) crust formation and breach. The detail will be discussed in the following text.
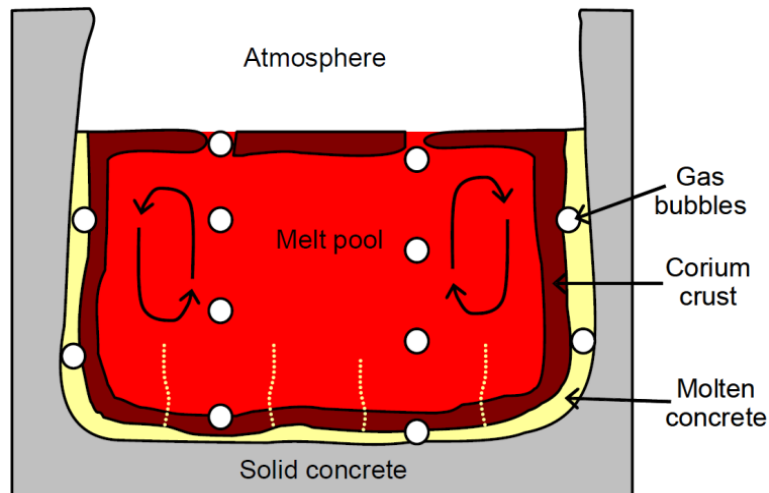
Figure 1-1. General illustration of the MCCI process

➢ **Concrete ablation**

The temperature of the melt core is higher than the melting point of the concrete, and the corium would keep being heated up by the decay heat. Thus, if there is no effective measurement to remove the heat, the temperature of the corium will increase and trigger the concrete dissolution. More precisely, the main constituents of core melt, or corium, are UO_2, ZrO_2, Zr, Fe, Cr and Ni, and it would be heated up until reaching at least partial melting (or even total melting) of oxide materials (UO_2, ZrO_2) and of metal released from the reactor vessel (temperature around 2200°C, while the

melt temperature of pure oxides and metal materials are about 2700°C and 1350-1900°C respectively) causing the buildup of a corium pool. The thermal generated from the fission products is converted to the corium pool boundary and gradually ablate the concrete wall. This is so called ablation process. For most types of concrete, dissolution occurs between around 1200°C and 1450°C. With the process concrete mixing into the corium, the solidus and liquidus temperature of the mixture would also change.

➢ **Crust formation and breach**

With the concrete heated up by the hot corium, the corium is also cooled down by the cold concrete and possible crust may form at the interface. The crust is probably porous to the gas from the concrete side, and provides thermal resistance between the corium and concrete. Because of the inside decay heat, the crust may re-melt after several hours. And possible eruption may also take place with the crust breach.

➢ **Stratification in the melt pool**

The liquid concrete and oxide phase in corium are miscible with each other, but the metallic phase is immiscible with the oxides. Thus possible stratification may exist in the melt pool. At the beginning, the metal may lay on the top of the pool since due to its smaller density compare to the oxides. But with the concrete mixing into the oxides, the density of the oxides is tend to become smaller and smaller, and eventually, the oxides may lighter than the metal and going to relocate at the top. On the other hand, because of the intense stirring of the liquid by the generating gas bubbles, the oxides and metal are tend to be mixed with each other. More experimental research is needed to investigate the detail about this phenomenon.

➢ **Chemical reaction**

Some chemical reactions take place in the melt pool during the MCCI process, which would also affect the ablation and temperature behavior of the corium. The

redox reaction would take place between the decomposition bubbles from melt concrete and the metallic materials in the mixture, and release the heat as another internal source heat except the decay heat. These redox chemical reactions are mainly

$$Zr + 2H_2O \rightarrow ZrO_2 + 2H_2 + 6.3MJ/kg_{Zr}$$
$$Zr + 2CO_2 \rightarrow ZrO_2 + 2CO + 5.7MJ/kg_{Zr}$$
$$2Cr + 3H_2O \rightarrow Cr_2O_3 + 3H_2 + 3.6MJ/kg_{Cr}$$
$$2Cr + 3CO_2 \rightarrow Cr_2O_3 + 3CO + 2.8MJ/kg_{Cr}$$
$$Fe + H_2O + 3.0kJ/kg_{Fe} \rightarrow FeO + H_2$$
$$Fe + CO_2 + 480kJ/kg_{Fe} \rightarrow FeO + CO$$
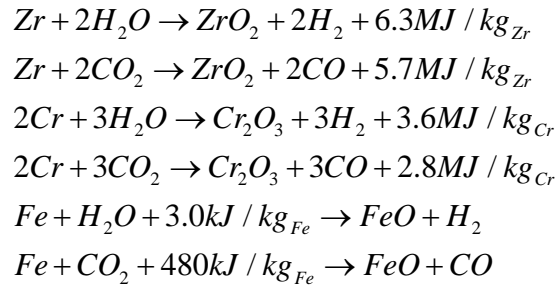
Some other chemical reactions may also affect the results

$$Zr + SiO_2 \rightarrow ZrO_2 + Si + 1.6MJ/kg_{Zr} \ (T < 1870^o C)$$
$$Zr + 2SiO_2 + 4.7MJ/kg_{Zr} \rightarrow ZrO_2 + 2SiO(g) \ (T > 1870^o C)$$
$$3Zr + 2Fe_2O_3 \rightarrow 3ZrO_2 + 4Fe + 5.8MJ/kg_{Zr}$$
$$Si + 2H_2O \rightarrow SiO_2 + 2H_2 + 15MJ/kg_{Si}$$
$$Si + 2CO_2 \rightarrow SiO_2 + 2CO + 14MJ/kg_{Si}$$
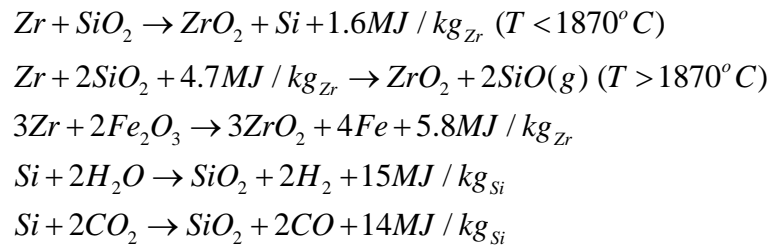
Among these reactions, Zr would be first oxidized, and Si, Cr, and Fe is following successively. The amount of Fe_2O_3 and Fe_3O_4 generated in the oxidation reactions are too small to be considered. The chemical reaction heats were obtained from the Outotec software: HSC chemistry[2].

➢ **Gas generation and movement**

Plenty of bubbles (mainly hydrogen and carbon monoxide) are generated from the chemical reaction. When these bubbles rising up, it would enhance the stirring of the liquid pool, the heat transfer between the corium and concrete and the diffusion process of concrete mix into the corium. Therefore, the movement and temperature behavior of bubbles in the melt pool should be studied. On the other hands, due to the important role played by the concrete decomposition gases, it is also indispensable to discuss the concrete behavior at high temperature condition, which will be discussed in the next section.

> **Parameters affecting the ablation behavior**

The melt pool behavior during the process is controlled by many aspects, such as the composition of the corium, the type of the concrete, the decay power of the corium pool and the velocity of the superficial gases. Besides, the material properties changes along the temperature and composition of the melt, which makes the research more complicated. For example, the heat transfer is effected by the viscosity of the corium, higher viscosity means weaker heat transfer. However, the viscosity of the corium changed sharply against the temperature since it is between the solidus temperature and liquidus temperature. In addition, the thermochemical properties would also change during the process due to the concrete mixed into the corium. Figure 1-2 shows the solidus and liquidus temperature of the mixture against its concrete mass fraction. A rapid decrease of solidus temperature against the weight fraction of concrete can be observed. In another word, the crust would not supposed be formed anymore after enough concrete mixed into the corium pool. Other material properties of mixture used in the simulation will be discussed in Chapter 4.
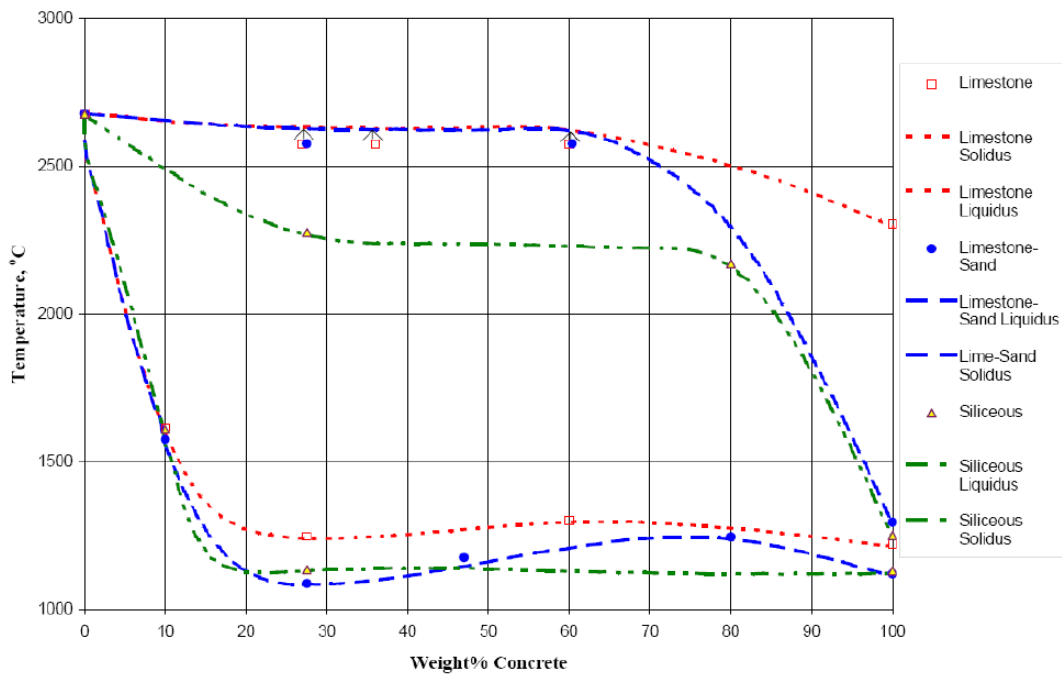
Figure 1-2. Solidus and liquidus temperatures of UO_2-ZrO_2-concrete mixtures[3]

1.1.3. Concrete behavior at the high temperature condition

In the following text, some important chemical reaction in the process of concrete decomposition will be introduced (Barometric pressure is assumed. The temperature of the chemical reaction would change against the environmental pressure).

100 ºC: Loss of evaporable water.

$$H_2O(l) + 2258kJ / kg_{H2O} \rightarrow H_2O(g)$$

100 ºC - 850 ºC: Dehydration of hydrates

$$3CaO \cdot 2SiO_2 \cdot 3H_2O \rightarrow 2CaO \cdot SiO_2 + CaO \cdot SiO_2 + 3H_2O(g)$$
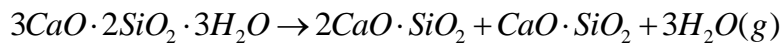
400 ºC – 600 ºC: Dehydration of calcium hydroxide

$$Ca(OH)_2 + 1340kJ / kg_{Ca(OH)2} \rightarrow CaO + H_2O(g)$$

574 ºC: Crystalline transformation from α- to β-quartz

$$SiO_2(\alpha) + 12kJ / kg_{SiO2} \rightarrow SiO_2(\beta)$$
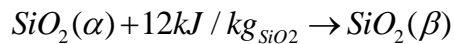
600 ºC -900 ºC: Decomposition of calcium carbonate

$$CaCO_3 + 1637kJ / kg_{CaCO3} \rightarrow CaO + CO_2(g)$$

1200 ºC – 1500 ºC: melting of the concrete

1423 ºC: Melting of quartz

$$SiO_2(s) + 130kJ / kg_{SiO2} \rightarrow SiO_2(l)$$
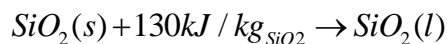
Based on these reactions, we can conclude that the gas bubbles generated from the concrete decomposition are mainly water vapor and carbon dioxide. Different amount of gases are generated based on the different types of concrete. Limestone

concrete generate more carbon dioxide, while the siliceous concrete generate almost only water vapor. Therefore, the type of the concrete is one of the key parameter in most MCCI experiment series.

Heat capacity is a very important parameter to calculate the heat transfer from the corium to concrete. Figure 1-3 shows the specific heat of different types of concrete from room temperature to melting temperature. We can see from the figure that the specific heat is increasing sharply against the temperature to all kinds of concrete. And it mainly shows higher specific heat of siliceous concrete than that of limestone type.
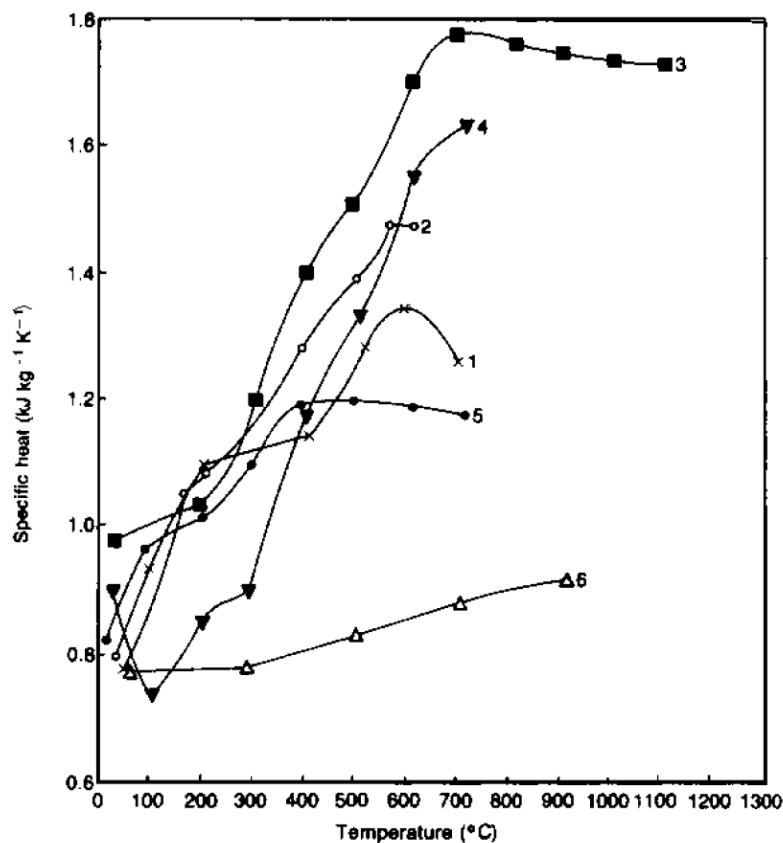
Figure 1-3. Measured specific heat of siliceous (curves 2 and 3), limestone (1, 4 and 5) and granite (6) aggregate concretes[4]

Besides specific heat, thermal conductivity is another important parameter which affect the heat transfer between the corium and concrete. For siliceous concrete, the thermal conductivity is about 2.5 W/m·K at room temperature and decrease to about

1.3 W/m·K at 800 ℃ and approximately constant until melting[4]. Similarly, to limestone concrete, the conductivity is about 2 W/m·K at room temperature and approximately equal to that of siliceous concrete above 100 ℃[4]. The conductivity of molten concrete is 1.0~1.2 W/m·K[4].

1.2. Review of the previous experimental research on MCCI

In order to resolve the scientific issues discussed above, extensive experimental research has been conducted since 1980s. In the following text, some important experiment and their achievement would introduced to show the background of the research of this paper.

1.2.1.Early experimental research

Table 1 shows some important experiments conducted before 1990s. In this period, simulant materials were used in most of the experiments instead of UO_2. The objective of these experiments is to analyze the concrete behavior, the ablation rate in the axial direction and the release of the fission product.

Electrical heating technique were used to simulate decay heat power in the most of the experiments. Since the axial direction ablation rate were focused on in this period, all the experiments were conducted in 1 dimensional, except BETA series. Based on these 1D experiments results, the typical ablation rate on axial direction is several centimeters per hour. Besides, the evidence of strong release of gas bubbling in the melt pool was also obtained. On the other hands, the only 2D experiment, Beta Series, also shows the pronounced ablation rate on axial direction. Figure 1-4 shows the results of BETA v1.8 crucible and BETA section v3.2 crucible[5], which has a big mass fraction of limestone. From the figure of gas release of different types of concrete, limestone concrete shows very strong gas ejection during the process. An important finding of the experiment is the release of hydrogen also after onset of

partial solidification of the metal melt. The overall gas release rate reduced after the beginning due to the lower ablation velocity.
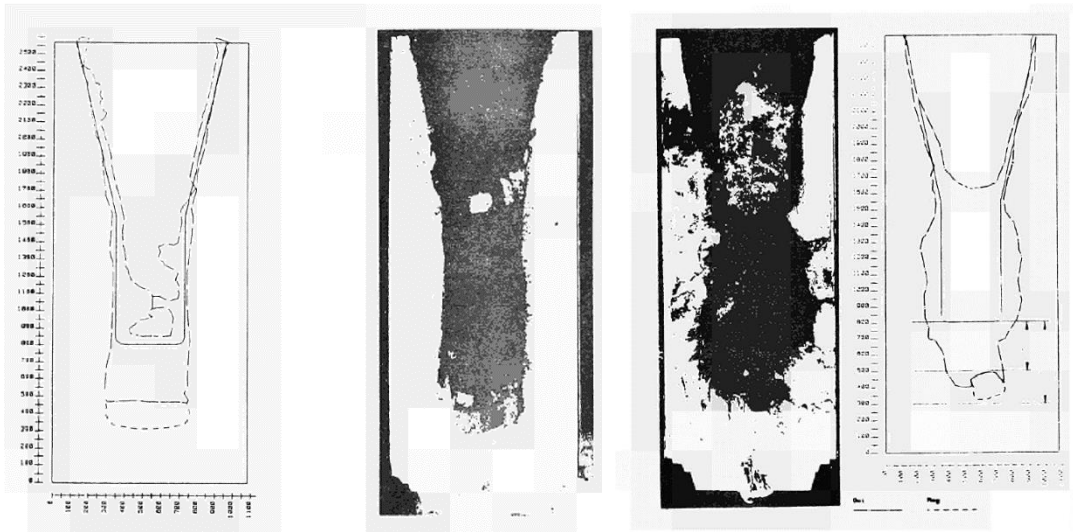
Figure 1-4. Posttest views of BETA experiments performed with alumina t iron melts. Left: BETA v1.8 test; Right: BETA v 3.2 test.

Because the decay heat is only provided by the metal in these experiments, which is opposite as that in the real scenario. Thus these results may not be directly applicable to the MCCI analysis.

The release of the gas from the case which applied limestone concrete is much higher than that using the other types of concrete due to the high mass fraction of $CaCO_3$. The carbon dioxide and the water vapor would interact with the metal phase in the melt pool. The oxidation of Zr and Cr is a strong exothermic process and generate H_2 and CO, which pressurize the space inside the cavity. The gas release is depend on the decay heat power and the concrete composition.

The advanced containment experiment (ACE) [6] is designed to measure the release of the fission products during the MCCI process. Besides, the temperature of the melt was also measured to analyze the thermal behavior of the melt. The facility of the experiments are shown in Figure 1-5. Results indicate the ablation rate is about 4mm/min in L1, L2, L4 test, and 1mm/min in L5, L7.
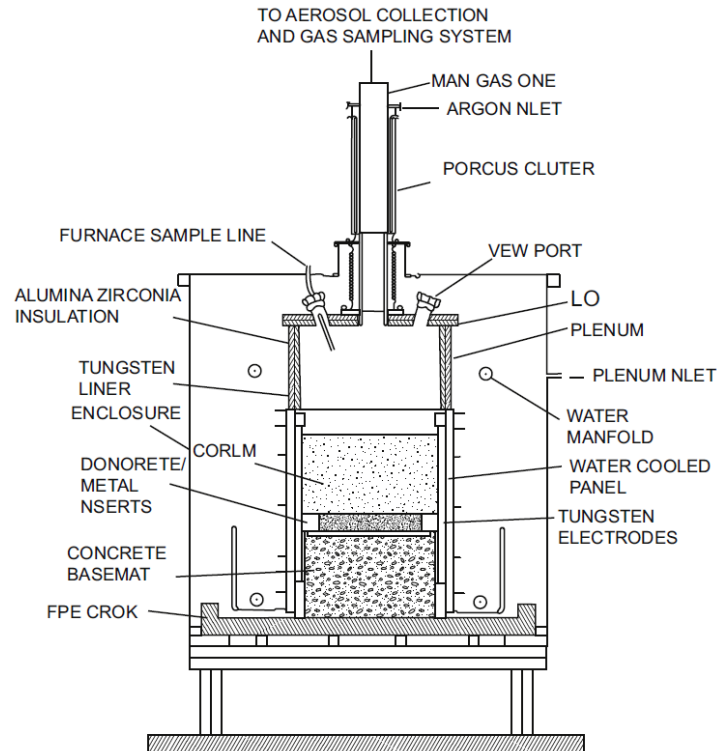
Figure 1-5. The test section of ACE experiment series.

Most of the experiments show the evidence of formation of the interfacial crust between the corium and water pool at the top. The crust would prevent heat transfer from corium to the water pool and continue to erode the concrete toward downward. In addition, eruption from the top crust was observed like volcanos. Figure 1-6 shows the test section of M1B in the MACE experiment[7]. The eruption is mainly due to the aggregation of the gas bubbles in the melt pool.

ACE [6]test provided the evidence of aerosol release during the interaction. Although the detail production mechanism is not clear from the experimental results, the evidence showed the aerosol is mainly made from concrete. Thus, it could support some empirical formula to calculate the release rate of aerosol during the process. However, more related experimental research is needed in the future.

Table 1. Early MCCI experiments

Program	Laboratory	Concrete	Corium	Crucible dimension	Geometry	Parameters
BETA[5]	KIT (Germany)	Siliceous, Limestone, serpentine	Fe, Zr, Cr, Ni, Al_2O_3, CaO	0.38m	2D	Decay power level
ACE[6]	Argonne National Laboratory (USA)	Siliceous, Limestone, Limestone-common sand	UO_2, ZrO_2 fission product simulants	0.5 x 0.5m	1D	Decay power level
SURC[8-10]	Sandia National Laboratory (USA)	Siliceous, Limestone Basaltic	Steel with Zr, UO_2, ZrO_2 and Cr fission product simulants	0.4m diameter	1D	Zr-SiO_2 condensed phase reactions
WETCOR[11]	Sandia National Laboratory (USA)	Limestone-common sand	Al_2O_3, CaO	0.32m diameter	1D	Overlying water pool
MACE[7]	Argonne National Laboratory (USA)	Siliceous, Limestone-common sand	UO_2, ZrO_2, Zr, Cr	0.3 x 0.3m to 1.2 x 1.2m	1D	Cool-ability issue, crust anchoring
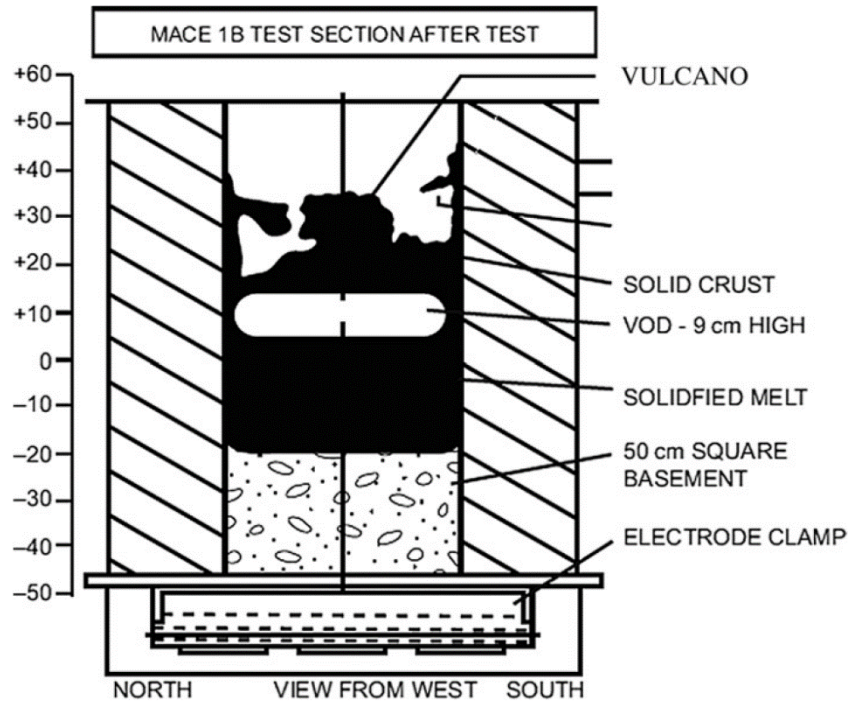
Figure 1-6. Eruption observed in M1B test[7]

1.2.2.Recent experimental research.

After 1990s, the experimental research on MCCI phenomena tend to focus on mainly two aspects: 1) ablation on lateral direction; 2) how the crust formation affect the ablation behavior, which is very important for long term erosion and the shape transform of the melt pool. The major recent experimental researches are stated in Table 1-2.

Compare to the early 1D experiment results, one of the most important finding in these tests is the ablation on lateral direction is stronger than that on axial direction. It can be seen clearly in CCI-3 test results (Figure 1-7)[12], where siliceous concrete was applied. In the opposite, more isotropic ablation behavior was observed in the experiment where limestone concrete was applied, like CCI-2 test (Figure 1-8)[12]. Similar conclusion can be found in VULCANO experiments. However, this conclusion need to be validated by additional experimental researches.
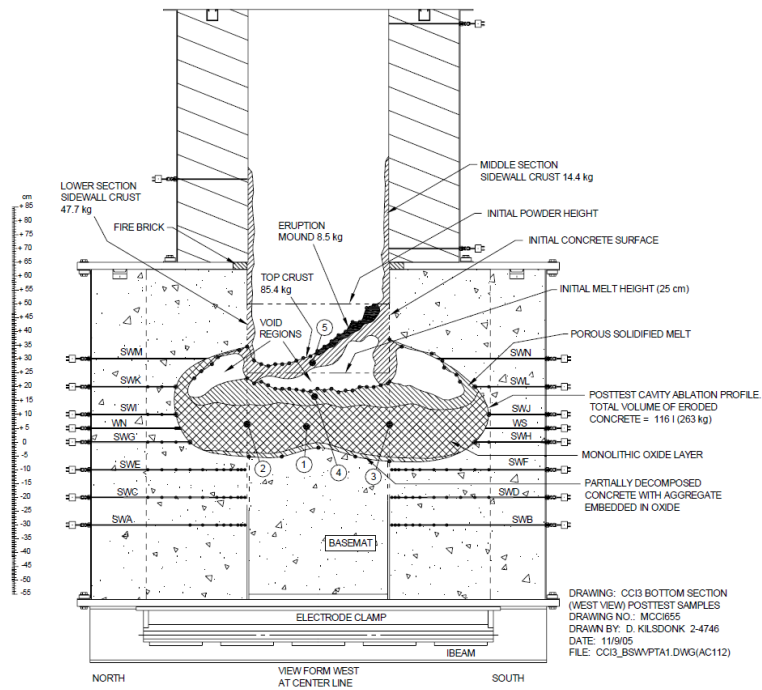
Figure 1-7. Sketch of anisotropic ablation in CCI-3 experiment[12]

COTELS experiment[13] indicates the water penetration affect the corium shape after the long term interaction. Less sidewall ablation can be seen from the results. However, the role of the crust formation, as well as their stability and breach, is still unknown yet. Another founding from the experiment is the different gas release from different types of concrete may affect the crust formation and stability. Moreover, the different mechanism of different concrete may also be the reason.

COMET experiments [14-16] investigated the phenomena of denser steel layer formed at the bottom of the melt pool. From the experiment, lower steel crust formation was observed (Figure 1-9). It is keep generating and removed through the whole process because of the gas bubble generation and its stirring effect to the melt pool. However, since the decay heat power is supposed to be an important parameter to analyze this phenomena, this experimental result is not perfect, because only metal phase was heated, not oxide. This phenomena requires more additional experiment to be confirmed.

Table 1-2 Recent Experimental MCCI research

Program	Laboratory	Concrete	Corium	Crucible dimension	Geometry	Parameters
CCI[12, 17]	Argonne National Laboratory (USA)	Siliceous, Limestone, Common Sand	UO_2, ZrO_2, SiO_2 with concrete	0.5 x 0.5m 0.5 x 0.79m	2D	Concrete type Time of top-flooding
VULCANO[18]	CEA (France)	Silica-rich, Limestone-rich	UO_2, ZrO_2, SiO_2, Ca	0.3m	2D	Concrete type Corium composition
COMET-L[14-16]	KIT (Germany)	Siliceous	Fe, Cr, Ni, Al_2O_3, CaO	0.6m diameter	2D	Decay power Time of top-flooding
COTELS[13]	NNC (Kazakhstan)	Siliceous	Oxide + Metal	0.26m 0.36m	2D	Concrete type Top flooding
ARTEMIS[19]	CEA (France)	Simulant (salt eutectic)	Simulant (salts)	0.29m	1D-2D	Gas generation Heat flux
HECLA[20]	VTT (Finland)	Siliceous	Stainless steel	0.28m	2D	Transient test
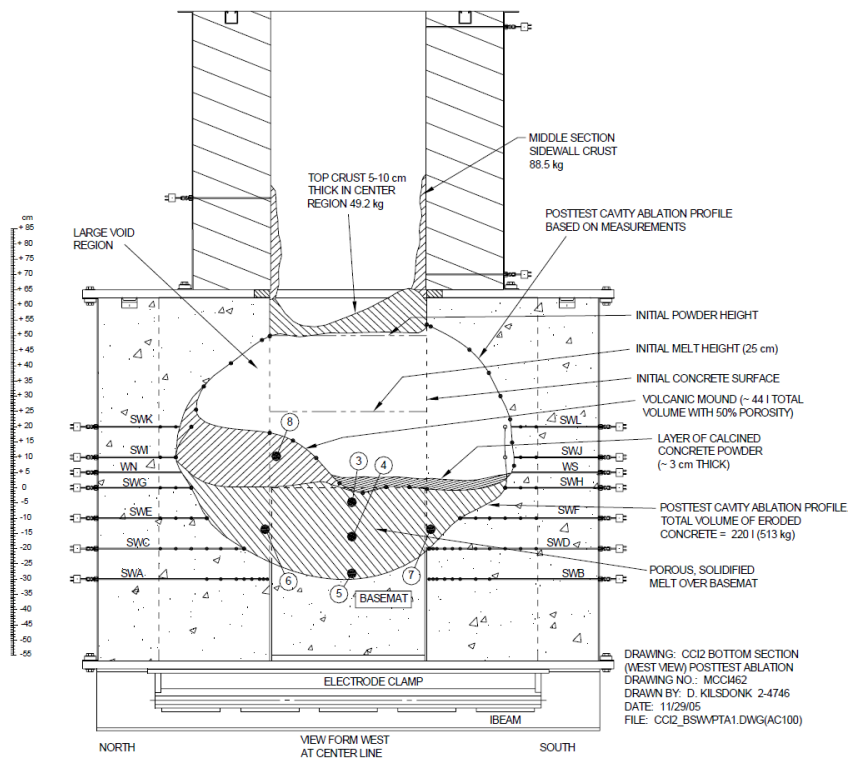
Figure 1-8. Sketch of isotropic ablation in CCI-2 experiment[12]

The stratification between the metal and oxide was investigated in VULCANO tests [18]. Based on the results, the test which used siliceous concrete (VBS-U2 and VBS-U3) observed the segregation in some part while the case which used limestone concrete (VBS-U1 test) didn't. Besides, the big space at the top is the evidence of the corium swelling during the experiment, as it is shown in Figure 1-10.
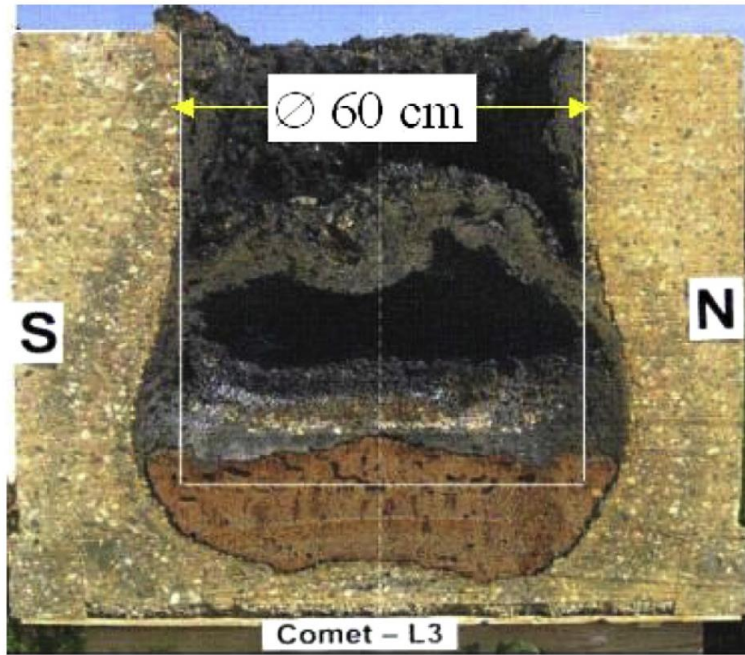
Figure 1-9. COMET-L3 test section[14]
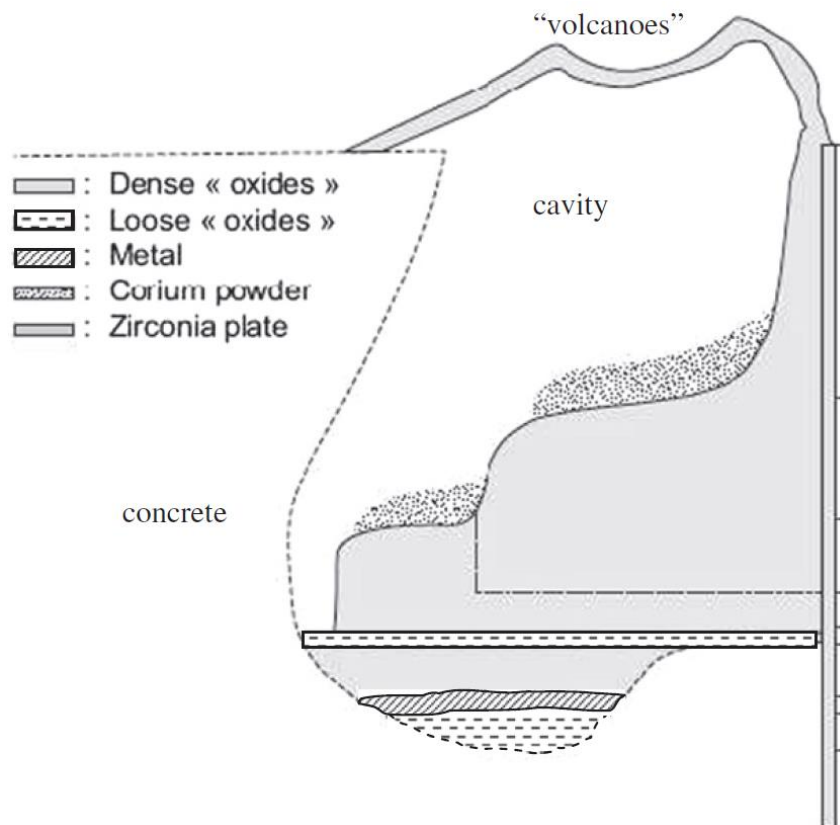
Figure 1-10. VULCANO VBS-U3 test section.[18]

1.3. Review of numerical simulation research on MCCI process

1.3.1. General introduction of the models

Large scale MCCI experiment is very difficult to perform because of the extreme experiment conditions and the corrosive corium. In addition, the measurement under such environment is also difficult, and some unexpected issues took place sometimes, such as melt splattering out of the test section. Thus, the numerical simulation could be another option way to investigate the detail phenomena during the MCCI process.

Table 1-3 state the major thermal hydraulic code applied for the MCCI simulation, as well as their main features, especially the heat transfer models. Different heat transfer models were applied in different codes, particularly in the part of interfacial heat transfer and crust formation model. Most of them has the validation results against the early large-scale experiments, which will be introduced in the following sections.

1.3.2. Validation against the early experiment

For 1D experiment simulation, MEDICIT code was applied to simulate ACE experiments. The results shows perfect fit with the experimental results both on the pool temperature and the axial ablation rate, as shown in Figure 1-11 [21]. However, the results is clearly affected by the choice of γ on both pool temperature and ablation rate.

For 2D simulation, Figure 1-12 shows the simulation results of CCI-2 experiments by using TOLBIAC-ICB code[22]. It shows the initial temperature is not well simulated in the code. However, after one hour, the temperature matches very well with the experiment. Indeed, for the initial temperature behavior of the melt pool, there is big uncertainties within different simulation codes, which will be discussed

later. The final sampling analysis gives the melt composition at the end of the experiment.
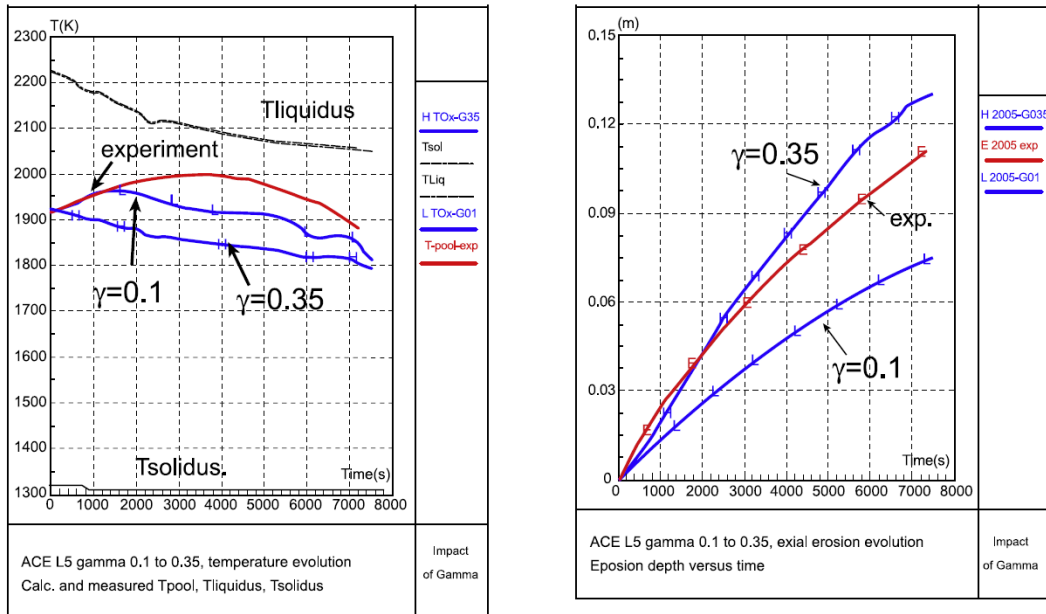
Figure 1-11. Comparison between MEDICIT code simulation results and ACE experimental results[21]
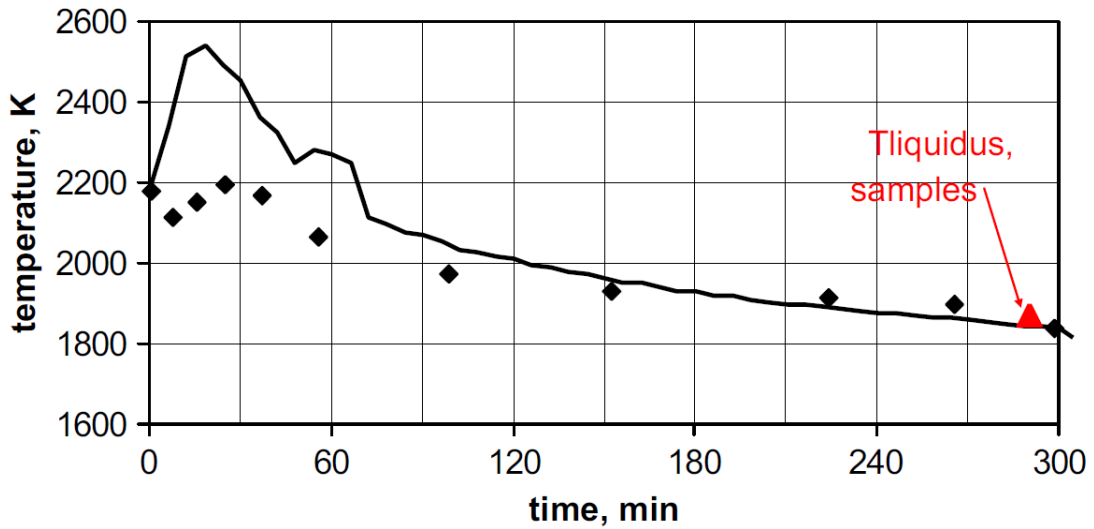
Figure 1-12. Comparison between the experiment results and the simulation results from TOLBIAC-ICB[22]

Possible stratification may exists during the long term MCCI process, where the melt phase is supposed to be located at bottom after several hours. Therefore in the early MCCI experiment, the axial ablation is pronounced due to the simulant decay

heat is released mainly from the metal phase, not the oxide. In order to resolve this issue, in some simulation codes, like TOLBIAC and MEDICIS, this behavior can be considered by assuming a thermal resistance near concrete/corium interface 3 times lower at bottom than that at the lateral interface. Figure 1-13 shows the blind simulation for COMET-L3 test[23]. Different results were obtained from different codes, and also shows big differ from the experimental data.
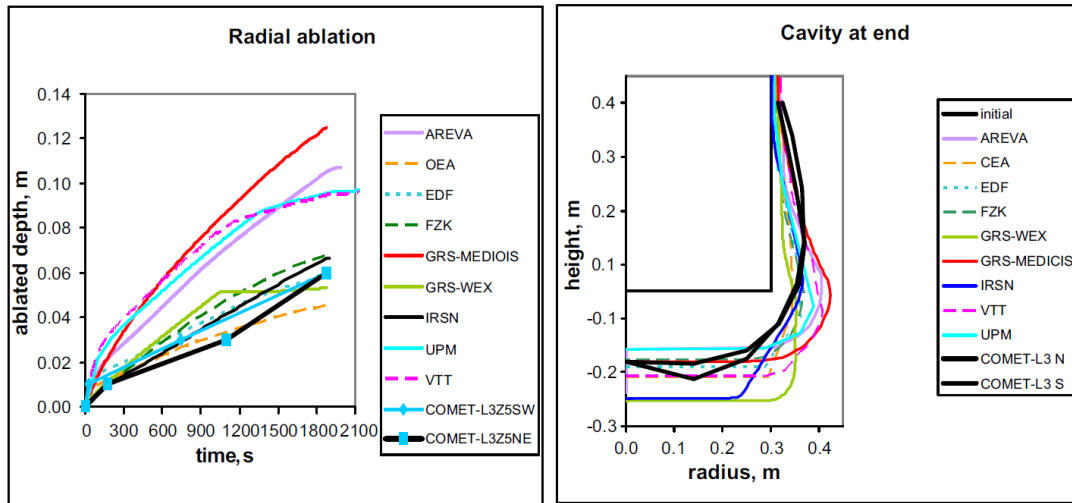
Figure 1-13. Simulation results by different simulation codes on both ablation kinetic and corium shape[23].

Another interesting simulation work is performed before CCI-2 experiment. Several simulation codes were organized by OECD to conduct a blind calculation to CCI-2 experiment using the exactly same input data[24]. This benchmark work is very important and the results were receivable. The comparison of the pool temperature between different codes are shown in Figure 1-14. Big differ can be observed. To specific, there are mainly three types of initial pool temperature behavior based on the result. TOLBIAC-CEA, TOLBIAC-EDF and MEDICIS IRSN shows a rapid increase in the first 10-20 minutes, COSACO and WEX shows a gradually decrease at the beginning, and MEDICIS GRS shows a sharp decrease within 10 minutes. Even after one hour, it still shows big deviation between different simulation results.

Table 1-3 Codes main models and assumptions

Code	ASTEC/MEDICIS by GRS	ASTEC/MEDICIS by IRSN	COSACO	COR-QUENCH	MELCOR	TOLBIAC-ICB	WECHSL WEX
Heat transfer at concrete/pool side	Correlation from exp. Results	BALI[25] + slag layer	BALI[25]	Kutateladze and Malenkov[26]	Slag layer	BALI[25]	Depending on the gas flow
Heat transfer at concrete/pool bottom	Correlation from exp. Results	BALI[25] + slag layer	BALI[25]	Kutateladze and Malenkov[26]	Kutateladze	BALI[25]	Depending on the gas flow
Heat transfer at pool upper interface	Correlation from exp. Results	BALI[25]	BALI[25]	Kutateladze and Malenkov[26]	Modified Kutateladze	BALI[25]	Depending on the gas flow
Heat transfer at oxide/metal interface	Greene and Irvine[27]	Greene	BALI[25]	Not used	Greene	BALI[25]	Werle[28]
Pool/crust interface temperature	$T_{solidus}$	$0.8\,T_{liquidus} + 0.2\,T_{solidus}$	Not used	$T_{solidus}$	$T_{solidus}$	$T_{Liquidus}$	$T_{sol}<T_{int}<T_{liq}$
Crust composition	Pool composition	Pool composition	Refractory material	Pool somposition	Pool composition	Refractory material	Pool composition
Stratification criterion	Not used	Modified BALISE	Density	Not used	Specific model	BALISE criterion[29]	Not used

The ablation rate is shown in Figure 1-15, where different results can be observed between the codes. According to the report, the ablation behavior is strongly affected by the empirical equations and the choice of the researcher: to choose an isotropic heat transfer or choose a predominant radial heat transfer compare to axial heat transfer.
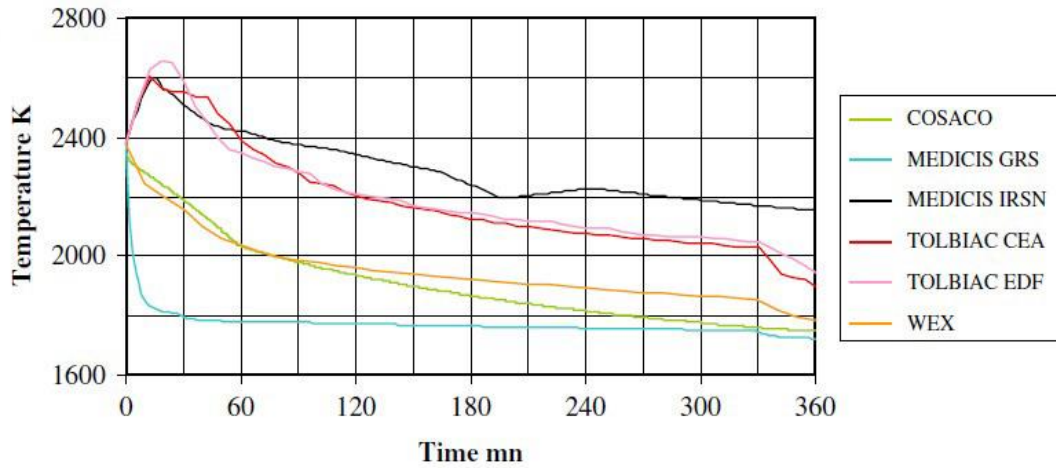
Figure 1-14. The benchmark work concerning CCI-2 experiment on pool temperature.[24]
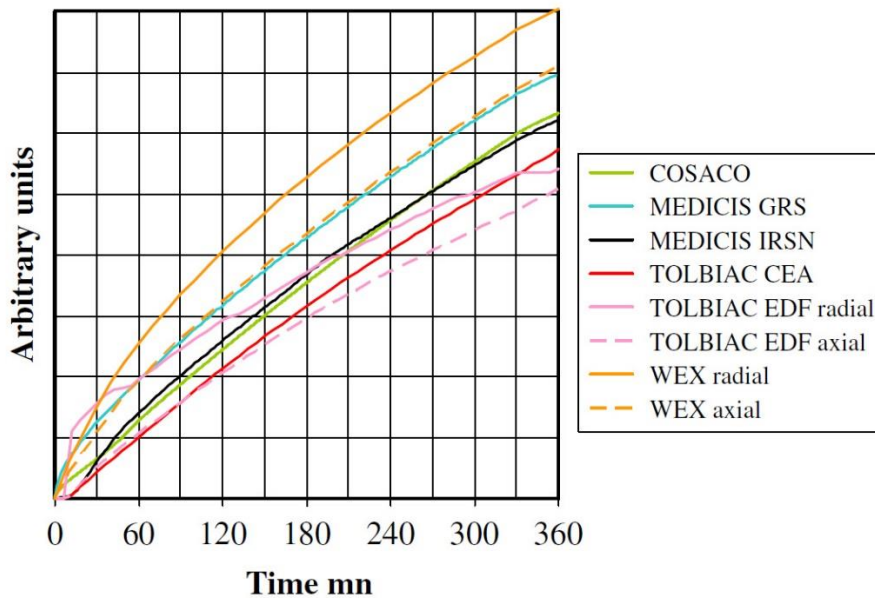
Figure 1-15. The benchmark work concerning CCI-2 experiment on ablation kinetic[24].

1.3.3. Uncertainties remain in the numerical simulation

Based on above information, we can conclude that although there are plenty of thermal hydraulic codes which can be applied to simulate MCCI process based on different empirical formula, big uncertainties can be seen from the different benchmark simulations due to the different models. Thus, to eliminate the uncertainty comes out from the different the empirical equations, several CFD codes are developed to precisely investigate the MCCI phenomena.

1.4. Review of the MCCI numerical simulation using MPS method

1.4.1. Why choosing MPS method

To avoid the uncertainty induced from the empirical equations, several numerical simulations were performed based on CFD method since 1990s. The following text will focusing on the numerical simulation conducted by using Moving Particle Semi-implicit (MPS) method. Compared to the other simulation methods, MPS method has its own particular merits for MCCI calculation:

1) Momentum and energy equations are solved without empirical formula;

2) Large deformation of interfaces can be analyzed easily without grid tangling;

3) No numerical diffusion since the convection terms are directly calculated by the motion of the particles.

The first one is the major advantage of CFD method compare to the thermal hydraulic code based on the empirical equations. While the 2) and 3) is the merits for particle method compare to the mesh method. These characteristics make the MPS method as a possible proper tool to investigate the MCCI process.

1.4.2. Previous MCCI simulation conducted by using MPS method

The SWISS-2 experiment was simulated by Koshizuka and Oka[30], in which heat transfer and phase-change models were developed to simulate the ablation behavior. The SWISS-2 experiment results was reported in 1987[31]. This experiment using the metallic mixture as the simulant of the corium. Refractory material is used on the side walls. Thus, this experiment is mainly focus on the axial ablation kinetics, as well as the heat transfer between the corium and concrete during the process. Based on the experimental setup, the calculation geometry is depicted in Figure 1-16. The simulation is x-y 2 dimensional though the experiment was performed by r-z 2 dimensional since the cylindrical coordinates cannot be used in MPS method. The size of the melt pool keeps exactly same as that in the experiment. The total number of the particles for corium, concrete and MgO are 513, 783 and 2025, respectively.
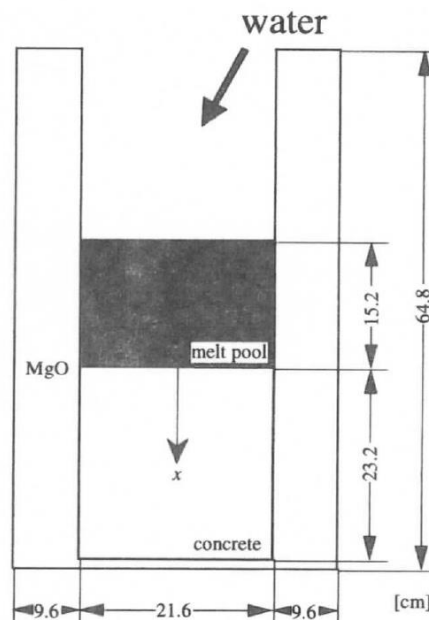
Figure 1-16. The calculation geometry of SWISS-2 experiment[30]
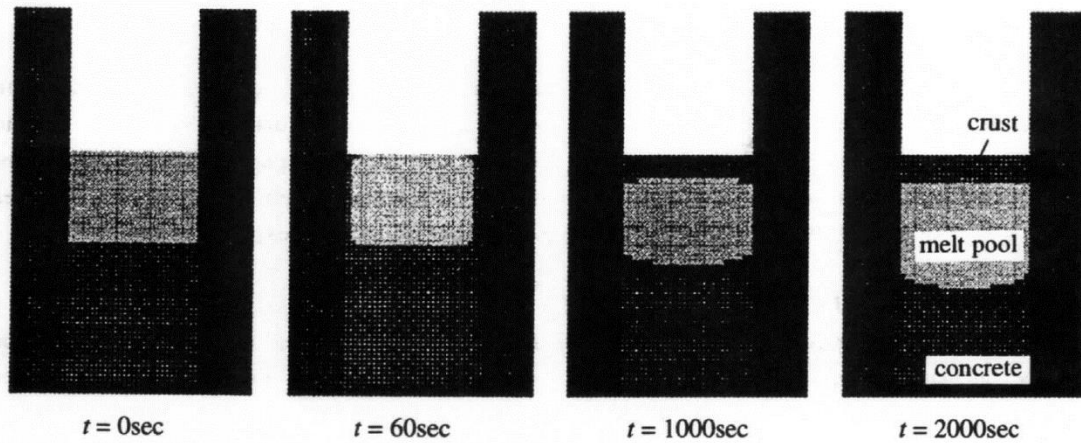
Figure 1-17. Ablation process and crust formation.[30]

Figure 1-17 shows the ablation process along the elapsed time[30]. Some debris particles are solidified at sidewall since 60sec, which are melted again at around 500sec and a layer of crust generated at the top of the melt pool. The thickness of the crust is constant till the end.
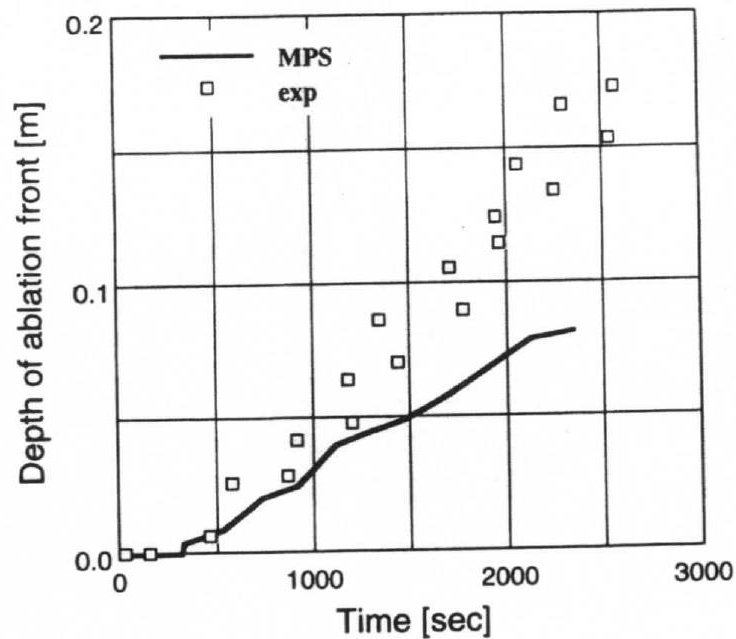
Figure 1-18. Ablation front in concrete[30]

Figure 1-18 shows the ablation front in the concrete[30]. The erosion does not take place in the first 300sec since the corium is cooled down by cold concrete at the beginning, which also observed from the experiment. After 300sec, we can see from

the figure that the simulation results is slower than that of the experiment. Based on the paper, this is mainly because the heat flux to the concrete is smaller in the calculation. The calculated temperature of the melt pool is much above the melting point since the natural convection is not considered, which made some thermal stored in the corium pool instead of transferred to the concrete.

Besides, another simulation with natural circulation model was also performed in the paper. The results shown in the Figure 1-19. Unfortunately, since the time step decreases to very small after insert the natural circulation model, the calculation didn't reach the end of the experiment to compare. However, a different crust shape at the top of the corium pool can be observed from the results.
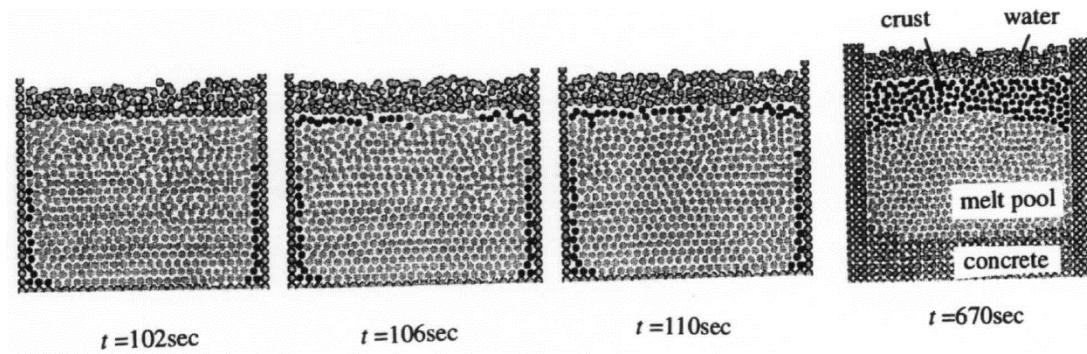
Figure 1-19. Crust formation with natural circulation model[30]

Another research was performed by X.Li in 2014[32]. SURC-2 and SURC-4 experiments were simulated in this research. SURC series tests were carried out by Sandia National Laboratory in 1980s, which aiming to provide a data base for MCCI with different concrete type and melt compositions. Similar as SWISS-2 experiment, SURC tests are focusing on only axial direction ablation. Figure 1-20 shows the geometry of the calculation, which is exactly similar as that in the SWISS-2 test.
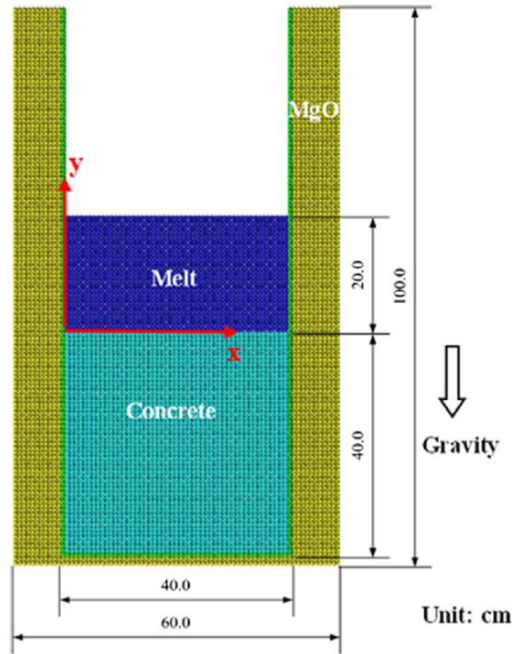
Figure 1-20. Configuration of the SURC-2 calculation[32].

Figure 1-21 shows the ablation process in the simulation. According to the simulation results, the downward erosion is kept going with the crust formation at the bottom. The concrete will be melted once it reaches the melting point. After that, the fluid concrete particles gradually rose, merged into the melt pool and floated at the top of the melt pool due to its smaller density compared to the molten corium.

Figure 1-22 depicts the ablation front comparison between experiment, MPS simulation and CONCOR[33] simulation results. Perfect agreement can be seen from the picture.

In addition, the paper discussed how the chemical reaction affect the ablation behavior, and conclude that the chemical reaction plays a very important role during the MCCI process. Unfortunately, it didn't explain very detail how to develop the model of the chemical reaction.
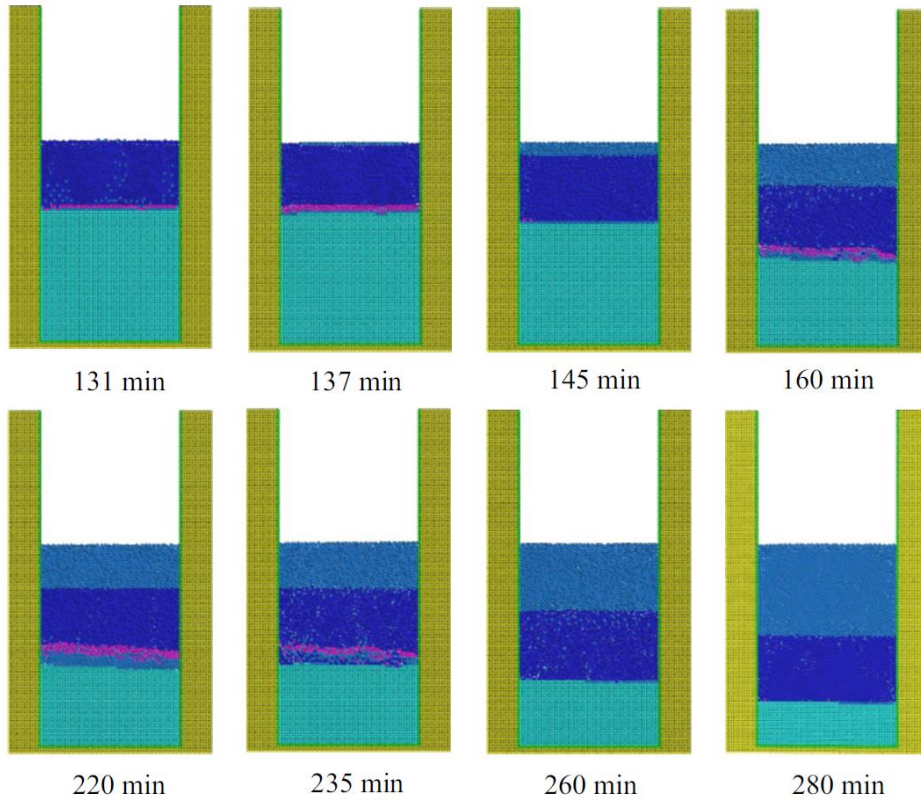
Figure 1-21. Ablation process from the calculation results[32].
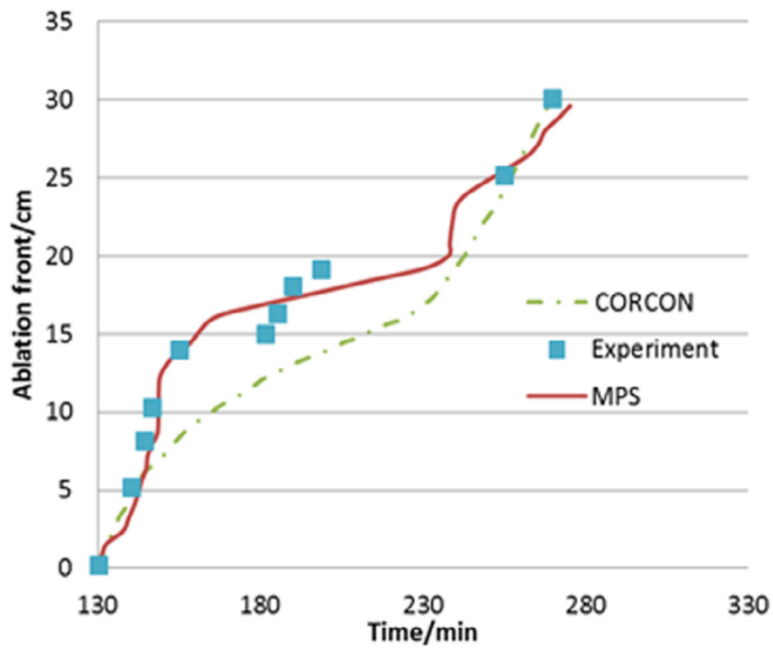
Figure 1-22. Comparison of the ablation kinetics[32].

1.4.3.Insufficient remains

Although previous simulation conducted by using MPS method obtained the reasonable results, there is a lot of space to improve.

1) In the SWISS-2 simulation, it did not conserve total mass and energy because it adopted the simplistic phase-change model, in which the material properties (density, specific heat and thermal conductivity) of concrete particles would directly changed to the corium particles' when they exceeded the melting temperature.

2) The simplified phase-change model was used in SURC-2 simulation. It made the concrete particles immiscible with the corium, where it should be miscible.

3) Based on the recent experimental research, the lateral ablation behavior plays an important, even dominant role during the process, but it was ignored in both simulations because of simulation object selection.

4) Chemical reaction model is not well developed and convincible. One chemical reaction model, which is more detail and physical, is needed to precisely analyze the phenomena.

5) Gas bubbling effecting in the experiment was ignored.

Therefore, MPS method need to be improved to fit on simulate the multi-physics phenomena during the MCCI process. That is the main objective of the research in this thesis.

1.5. Objective of this work

To precisely investigate the phenomena during the MCCI process, a new multi-physics simulation code based on MPS method is developed. Heat transfer model, phase change model, natural circulation model were implemented, and mixing

model, mass diffusion model, chemical reaction model and gas generation model were developed in the simulation. To validate the models are applicable for MCCI simulation, the validation work is also necessary. Thus, several specific experiment are simulated to validate the model. The research can be summarized as Table 1-4.

By developing the multi-physics models, the calculation is more physical and reliable to investigate the MCCI phenomena. In detail, the improvement compare to the previous numerical simulation conducted by MPS method is shown in Table 1-5.

All in all, the final objective of this work is investigate the MCCI phenomena and resolve the uncertainties remains based on the current experimental studies by developing multi-physics models based on MPS method. Currently in this paper, validating the availability of the models is the main mission.

Table 1-4. Summarize of the work chart

Models	Original	Verification	Tin experiment	Gallium experiment	Wax experiment	CCI-2 experiment
Heat transfer	Imp	O	O	O	O	O
Phase change	Imp	O		O	O	O
Natural circulation	Imp		O	O	O	O
Surface tension	Imp				O	O
Mixing	Ori					O
Chemical reaction	Ori					O
Gas generation	Ori					O
Mass diffusion	Ori					O

Table 1-5. Improvement compare to the previous calculation

Issues	Previous CFD code	Developed code
Simulated experiment dimension	1-D ablation	2-D ablation (with lateral ablation)
Chemical reaction	Yes	Yes (consider Cr)
Mixing model	Directly change particle type or ignore the mixing process	Modify the particle mass when concrete mix into the corium
Gas generation model	No	Simplified model

2. Development of multi-physics model based on MPS method

2.1. Basic MPS method

2.1.1. Outline of MPS method

The MPS (Moving Particle Semi-implicit) method was first proposed by Koshizuka and Oka in 1990s [34-38]. In the MPS method, the governing equations are discretized according to particle interactions. Thus, the sharp deformation at the interface is easily simulated since the grids are not necessary. In the past ten years, the MPS method has been used in the field of nuclear engineering [39-41], ocean engineering[42], and medical technology[43]. In the field of nuclear safety analysis, MPS method also be applied in many researches on melt spread calculation [44], melt freezing behavior in an instrument tube[39, 41]. Besides, it was also been used for fuel–coolant interaction[45], vapor explosion[46], and ex-vessel molten corium spreading[44]. Therefore, MPS method is a possible proper tool for the MCCI investigation.

In the following text, the models implemented in a new MPS code, which is developed aiming to investigate the MCCI phenomena, are introduced. Movement and heat transfer of the particles are directly solved by the governing equation; Natural circulation are calculated based on Boussinesq assumption; Phase change are calculated by the enthalpy and the melting point; chemical reaction are calculated based on the chemical composition of both corium and concrete; mixing process are simulated by the diffusion process of the concrete; gas are simulated as a channel shift particles and enhance the string of the melt pool and the heat transfer between the corium and concrete.

2.1.2. Governing equation

The governing equations of the MPS method are the continuity, Navier-Stokes, and energy conservation equations:

$$\nabla \cdot \mathbf{u} = 0 \tag{2-1}$$

$$\frac{\partial \mathbf{u}}{\partial t} + (\mathbf{u} \cdot \nabla)\mathbf{u} = -\frac{1}{\rho}\nabla p + \upsilon \nabla^2 \mathbf{u} + \mathbf{F} \tag{2-2}$$

$$\frac{\partial h}{\partial t} = k\nabla^2 T + Q \tag{2-3}$$

where ρ, t, $\mathbf{u}$, p, υ, $\mathbf{F}$, h, k, T, and Q are density, time, velocity vector, pressure, kinematic viscosity, external force, enthalpy, thermal conductivity, temperature, and heat source, respectively.

2.1.3. Particle interaction models

In the MPS method, the fluid is represented by moving particles. The particle interaction is defined within a constant distance r_e using a kernel function w(r):

$$w(r) = \begin{cases} \dfrac{r_e}{r} - 1 & (r < r_e) \\ 0 & (r \geq r_e) \end{cases} \tag{2-4}$$

where *r* is the distance between two particles *i* and *j*.
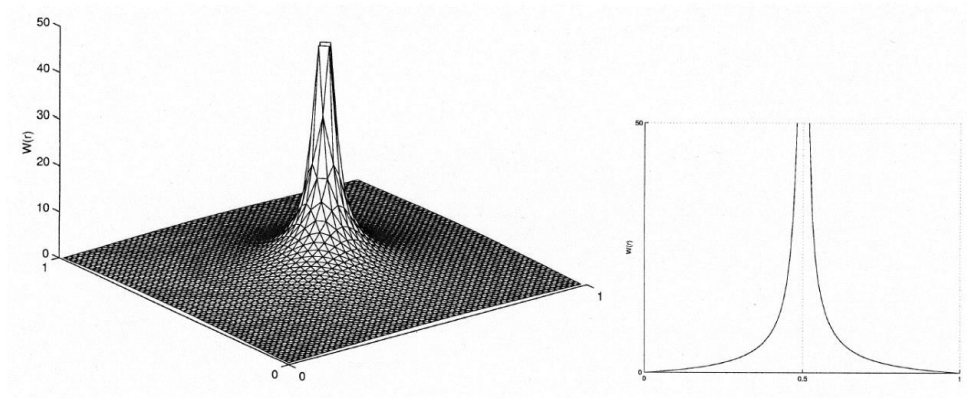
Figure 2-1. The kernel function[47].

Parameter n_i is a particle number density for particle i, which is defined as

$$n_i = \sum_{j \neq i} w\left(\left|\mathbf{r}_j - \mathbf{r}_i\right|\right)$$

(2-5)

where $\mathbf{r}_j$ and $\mathbf{r}_i$ are the coordinates of particle i and j. It represents the density of particles around particle i. In the case of an incompressible fluid, the particle number density of the fluid is kept constant. The continuity equation is satisfied automatically by holding the total number of particles and the mass of individual particles constant.

The gradient of the scalar field φ at particle i is computed by the weighted average of gradient vectors as

$$\langle \nabla \phi \rangle_i = \frac{d}{n^0} \sum_{j \neq i} \left[\frac{\phi_j - \phi_i}{\left|\mathbf{r}_j - \mathbf{r}_i\right|^2} \left(\mathbf{r}_j - \mathbf{r}_i\right) w\left(\left|\mathbf{r}_j - \mathbf{r}_i\right|\right) \right]$$

(2-6)

where d is the space dimension's number.
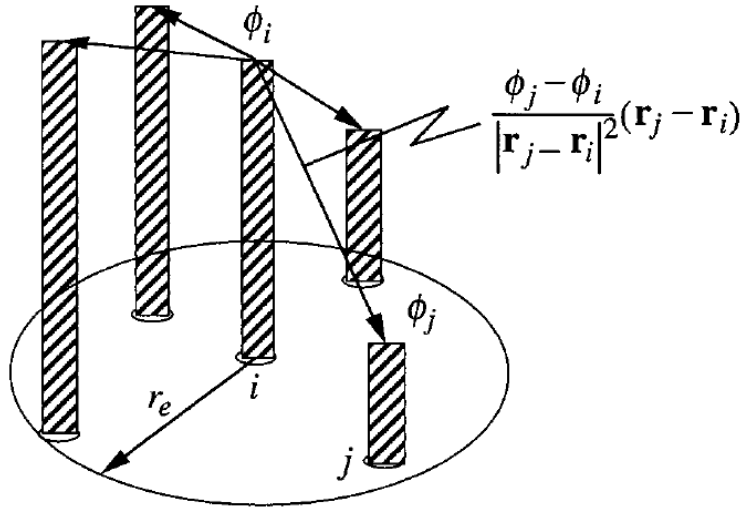
Figure 2-2. Concept of the gradient model[34].

In the MPS method, the Laplacian of ϕ is discretized by distributing a part of ϕ from particle i to its neighbor particles using the kernel function as

$$\left\langle \nabla^2 \phi \right\rangle_i = \frac{2d}{n^0 \lambda} \sum_{j \neq i} \left[\left(\phi_j - \phi_i \right) w \left(\left| \mathbf{r}_j - \mathbf{r}_i \right| \right) \right] \tag{2-7},$$

where λ is a parameter that is chosen such that the variance fits the analytical value:

$$\lambda = \frac{\int_V w(r) r^2 dv}{\int_V w(r) dv} \tag{2-8}$$
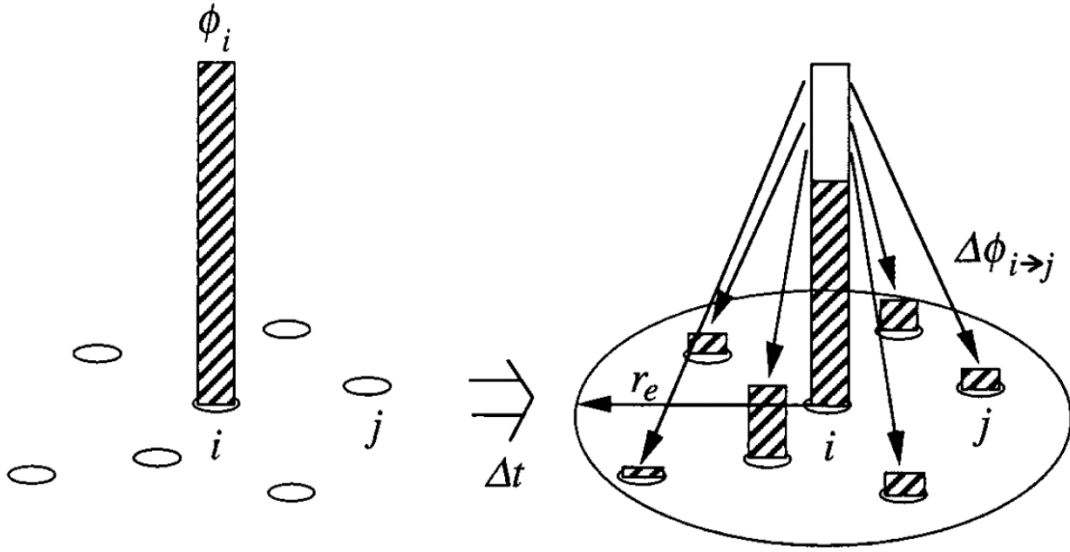
Figure 2-3. The concept of the Laplacian model[34].

2.1.4. Algorithm for incompressible fluid

A semi-implicit algorithm is employed in the MPS method. Viscosity term and external force terms in the Navier-Stokes equation are explicitly calculated in order to obtain the temporary velocities $\mathbf{v}_i^*$, and the temporary coordinates $\mathbf{r}_i^*$, $\mathbf{v}_i^{(k)}$, and $\mathbf{r}_i^{(k)}$ the velocity and coordinate from the last time step. The particles are moved based on the following equations:

$$\mathbf{v}_i^* = \mathbf{v}_i^{(k)} + \Delta t (\nu \nabla^2 \mathbf{v}_i^{(k)} + \mathbf{g}) \tag{2-9}$$

$$\mathbf{r}_i^* = \mathbf{r}_i^{(k)} + \mathbf{v}_i^* \Delta t \tag{2-10}$$

where Δt is the time-step width, and superscripts on the right shoulder, *k,* show the time step, and **g** is the vector of gravity. The pressure is then calculated by solving the following Poisson equation:

$$\left\langle \nabla^2 P \right\rangle_i = -\frac{\rho}{\Delta t^2} \frac{n_i^* - n^0}{n^0} \tag{2-11}$$

By solving this equation, the corrected velocity is obtained. The corrected convection is then calculated using the corrected velocity, and particle *i* moves to its final position in this time step.

$$\boldsymbol{v}_i^{k+1} = \boldsymbol{v}_i^* - \frac{\Delta t}{\rho} \cdot \nabla P \tag{2-12}$$

$$\mathbf{r}_i^{(k+1)} = \mathbf{r}_i^* - \frac{\Delta t^2}{\rho} \nabla P \tag{2-13}$$

More detailed explanation of the MPS method can be found in the references [34, 35, 42, 43].

2.2. Particle type and particle material

In order to explain the multi-physics models, it will be helpful to introduce relationship between the particle type and the particle material in advance.

In the original MPS method, fluid is represented by the moving particles, each particle has their own material parameters, which defined by the type of the particle. In other words, one type of particle has only one group of material parameter and phase. This system is good enough to solve most single material cases. However, this will be chaotic and complicated when we calculate a multi-material with multi-phase case, because plenty of particle type need to be defined, probably more than 10. Thus, a new particle system is developed in this research, which separate the particle type and particle material.
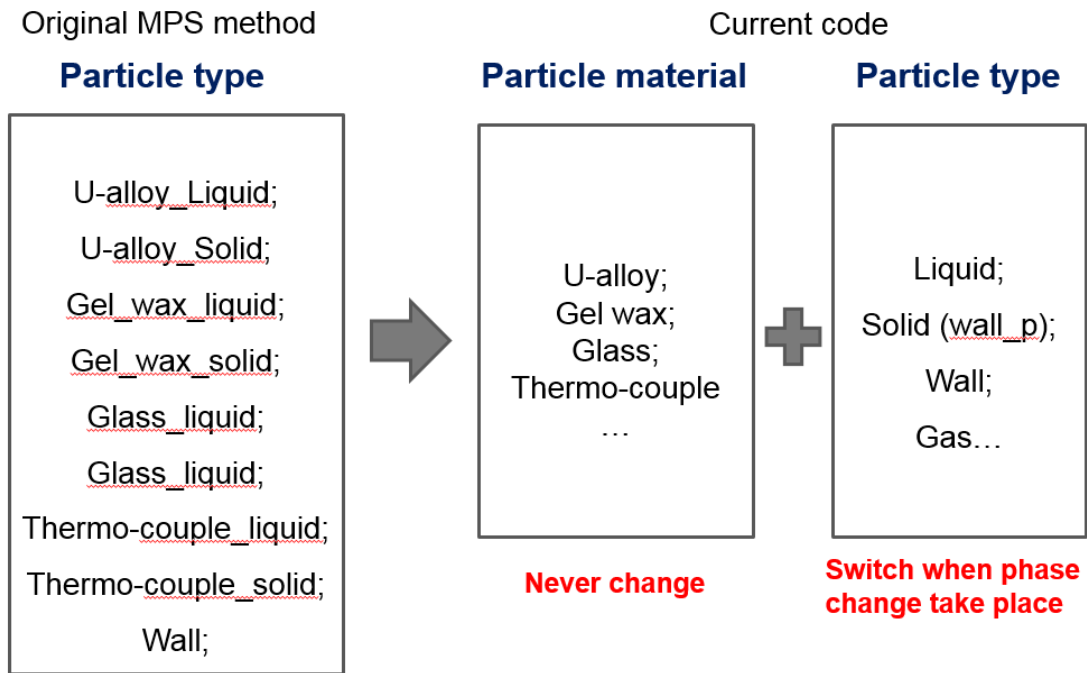
Figure 2-4. The particle system in the original MPS method and current code

As shown in Figure 2-4, there are four kinds of particle types in this system: liquid, solid, wall, gas. Liquid, solid and gas are used to define the phase of the normal particles. Wall particles are the virtual particle in the boundary to calculate the particle number density. Besides, particle type decide the movement boundary condition of the particles in the calculation. On the other hands, particle materials define the physical composition of this particle, such as u-alloy, gel-wax, concrete et.al. Every particle obtain their own physical parameters by both material and type.

This new system simplified the simulation code, especially in the case with multi-material and multi-phase. In the following text, this definition will be mentioned when multi-physics models are introduced.

2.3. Multi-physics models

2.3.1. Heat transfer and phase change models

Heat transfer between particles is discretized based on the energy equation (Eq. 2-3). The equation can be explicitly solved using the Laplacian model:

$$\frac{Dh_i}{Dt} = \frac{2d}{n^0 \lambda} \sum_{j \neq i} \left[k_{ij} \left(T_j - T_i \right) w \left(\left| \mathbf{r}_j - \mathbf{r}_i \right| \right) \right] + Q_i \qquad (2\text{-}14)$$

where h and Q are the enthalpy and heat source of particle i, respectively. The temperature is then calculated using Eq.2-15, where T_s and T_l are solidus temperature and liquidus temperature, respectively:

$$T = \begin{cases} T_s + \dfrac{h - h_s}{\rho C_{ps}} & (h < h_s) \\[2mm] T_s + \dfrac{h - h_s}{h_l - h_s}(T_l - T_s) & (h_s \leq h \leq h_l) \\[2mm] T_l + \dfrac{h - h_s}{\rho C_{pl}} & (h_l < h) \end{cases} \qquad (2\text{-}15).$$

For materials with a fixed melting point, the solidus and liquidus temperatures are given the same value as the melting temperature; i.e.,

$$T_s = T_l = T_{melt} \qquad (2\text{-}16)$$

To express the phase change, solid-fraction γ is introduced and calculated based on enthalpy h using

$$\gamma = \begin{cases} 1 & (h < h_s) \\[2mm] \dfrac{h_l - h}{h_l - h_s} & (h_s \leq h \leq h_l) \\[2mm] 0 & (h_l < h) \end{cases} \qquad (2\text{-}17),$$

which is used as a criterion to judge the phase of the material.

2.3.2. Surface tension model

The surface tension model is needed to simulate the immiscible materials in wax experiment and the possible stratification in MCCI pool. In this paper, the model developed by Kondo et al.[48] is adopted. In this model, surface tension is represented by the potential force between the particles:

$$\begin{cases} P(r) = \dfrac{C}{3}(r - \dfrac{3}{2}r_{\min} + \dfrac{1}{2}r_e)(r - r_e)^2 & (r \le r_e) \\ P(r) = 0 & (r \ge r_e) \end{cases} \tag{2-18},$$

where r, $r_{\min}$, r_e, and C are the particle distance, the initial minimum particle distance, the effective radius of the potential force and fitting coefficient, respectively. Coefficient C controls the strength of the surface tension. Surface tension is strong when C is large. In this paper, $r_{\min}=d$ and $r_e=3.1d$ are used. As shown in Figure 2-5, a unit area $S=r_{\min}^2$ between two fluids is established to simulate the surface energy inside it. To create this area, the particles existing from area A should be detached from the particles existing in area B. This is depicted in Eq. 2-19. Combining Eq. 2-19 with Eq. 2-18, C can be derived as Eq. 2-20:

$$2\sigma r_{\min}^2 = \sum_{i \in A, j \in B} P(r_{ij}) \tag{2-19}$$

$$C = \frac{3 \times 2\sigma r_{\min}^2}{\displaystyle\sum_{i \in A, j \in B, |r_{ij}| < r_e} (r_{ij} - \dfrac{3}{2}r_{\min} + \dfrac{1}{2}r_e)(r_{ij} - r_e)^2} \tag{2-20}$$

where σ is the surface tension coefficient of the material. This is the relationship between the potential force and surface tension. Particle convection can be subsequently calculated using Eq. 2-21.

$$m\frac{d\vec{v}}{dt} = C(r_{ij} - r_{\min})(r_{ij} - r_e)\vec{n}_{ij} \tag{2-21}$$
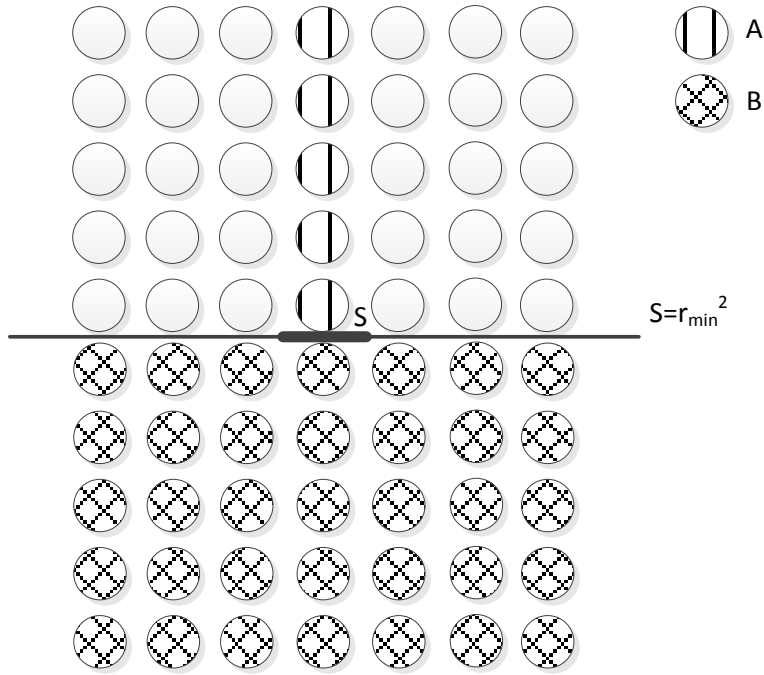
Figure 2-5. Surface energy estimation.

2.3.3. Natural circulation model

Boussineq approximation is used to simulate the natural circulation inside the melt pool.

$$\mathbf{F} = \beta \mathbf{g}(T - T_s) \tag{2-22}$$

Where F, β, g, T, Ts are body force, thermal expansion coefficient, gravity, temperature, average temperature of the melt pool respectively.

2.4. Developed physical model for MCCI simulation

2.4.1. Mixing model

During the MCCI process, the concrete is going to be melted and mixed into the mixture. Thus, mixing model is developed to investigate this phenomena. In the previous simulation, the mixing process was ignored, which results the non-conservation of the total mass and unphysical stratified layer between the

concrete and corium. In this paper, two new types of mixing model is developed and applied in the MCCI simulation.

➢ **Mixing model 1:**

To remedy the insufficient exists in the previous researches, a conservative equation is used for the mixing process. Once the concrete particle melt, the particle type will change from solid to liquid. Once the liquid concrete touch the corium particles, this concrete particle will be seems to be mixed into the melt pool. Meanwhile, the particle material will be switched from concrete to corium. Because of the difference of the material properties between the concrete and the corium, the physical parameters of the melt pool need to be reset to conserve the total mass and energy.

Eq. 2-23 is used in this research. The physical meaning of this formula is to average the properties through the whole corium area when there is concrete particle mixed into the pool.

$$\varphi_{melt} = \frac{\varphi_{corium} \times (total\_corium - total\_crust) + \varphi_{concrete} \times total\_melt}{total\_corium - total\_crust + total\_melt} \tag{2-23}$$

Where $total\_corium$ is the initial corium particle amount; $total\_crust$ is the total amount of crust particles; $total\_crust$ is total amount of melted particles; φ_{melt} is the real properties at the melt pool; φ_{corium} is the properties of the pure corium; $\varphi_{concrete}$ is the properties of the pure concrete.

The total mass and energy will be conserved automatically by using this model. And it is very simple to apply in the simulation. However, the diffusion process is supposed to be infinity in this model. Thus, the mixing model 2 is developed to solve this insufficient.
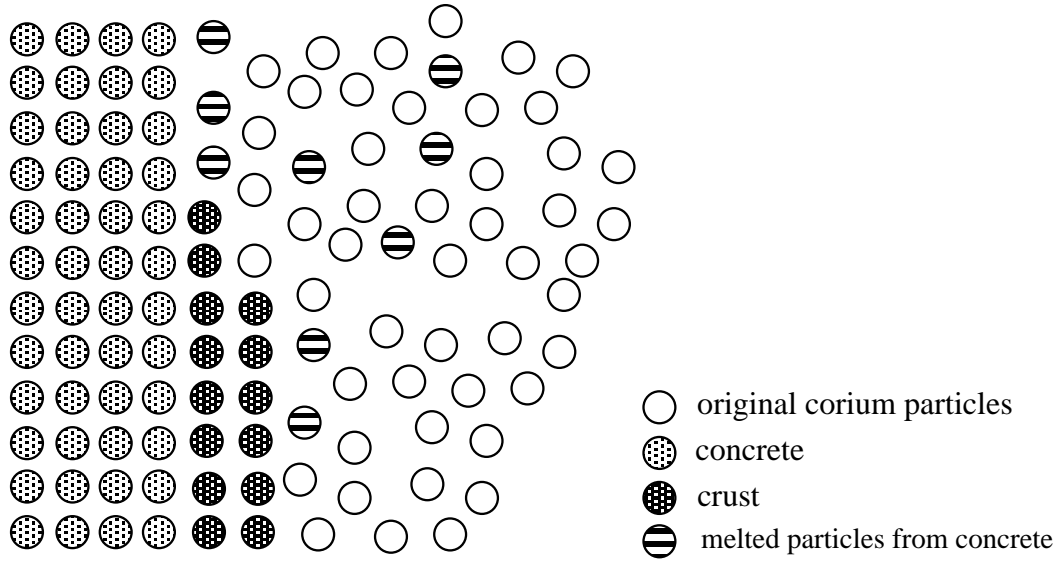
Figure 2-6. The concept of the mixing model

➢ **Mixing model 2:**

As a matter of fact, the mixing phenomena is not infinity during the MCCI process. Mixing model 2 is developed to solve the diffusion of both concrete and corium in MCCI. In this model, each particles has the composition of both corium and concrete, just like two barrels. For the concrete particles, the concrete barrel is 100% full while the corium one is empty. The mass diffusion equation will be solve between particles and the mass in the barrels will be transferred with each other.

$$\frac{\partial m}{\partial t} = D\nabla^2 m \tag{2-24}$$

where m is the mass and D is the diffusion coefficient of the material. The right side of the equation is discretized by the Laplacian model (Eq.2-7) in MPS method. Therefore, the Eq.2-24 can be written as

$$m_i^{t+1} = m_i^t + D\Delta t \cdot \frac{2d}{n_0\lambda} \sum_j (m_j^t - m_i^t) w_{ij} \tag{2-25}$$

where m_i^{t+1} is the mass of particle i at the time step $t+1$, m_i^t is the mass of particle i at the time step t, m_j^t is the mass of particle j at the time step t.

Similar model was applied by Mustari and Oka in eutectic simulation [49, 50]. From the verification work done from these papers [49, 50], this model is proved available to be applied in such simulation.
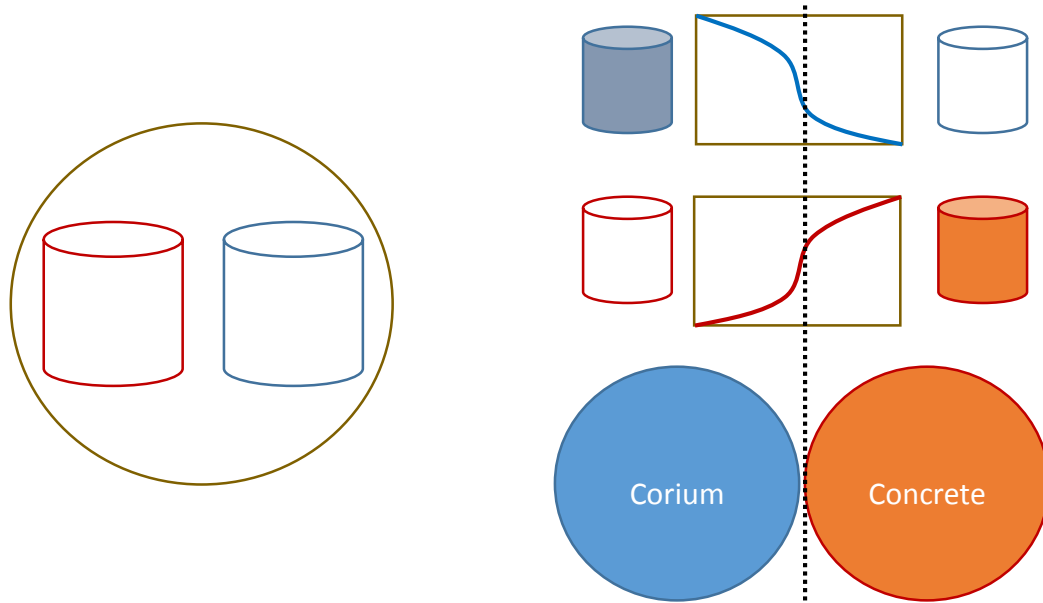
Figure 2-7. Left: two barrels in one particle; Right: the description for the mass diffusion

Each particle has its mass fraction of corium w_{corium} and mass fraction of concrete $w_{concrete}$. The material properties will be calculated by this mass fraction. The density will be calculated by the new mass and volume of the particle. And the other thermal properties will be calculated by

$$C_i = C_{corium} \times w_{corium} + C_{concrete} \times w_{concrete} \qquad (2\text{-}26)$$

where C_i is the material properties, including specific heat, thermal conductivity et. al. C_{corium} is the material properties of pure corium; $C_{concrete}$ is the material properties of concrete.

It can simulate continuous erosion process from the beginning after insert this model. The diffusion coefficient is much lower in solid particles than that in liquid particles. However, it effect the erosion process and change the composition of the crust, which will change its broken behavior.

2.4.2.Chemical reaction model

Chemical reactions during the MCCI process are considered in the code. It departed by two parts, one is the concrete decomposition during the ablation process, while another one is the redox reactions between the metal in the melt pool and the gas from the melt concrete.

As to the part of concrete decomposition, the decay heat for each dehydration reaction is considered in the code (the detail chemical reaction equations can be found in Chapter 1). The temperature will calculated using Eq.2-15, the solidus temperature and liquidus temperature is replaced by the start/end point in the dehydration process. Besides, the mass of steam and carbon dioxide is calculated by the composition of the concrete

The redox reaction will take place once the steam or carbon dioxide touch the corium particles. Hydrogen and carbon monoxide will be generated and finally going up to the top.

$$Zr + 2H_2O \rightarrow ZrO_2 + 2H_2 + 6.3MJ / kg_{Zr}$$
$$Zr + 2CO_2 \rightarrow ZrO_2 + 2CO + 5.7MJ / kg_{Zr}$$
$$2Cr + 3H_2O \rightarrow Cr_2O_3 + 2H_2 + 3.6MJ / kg_{Cr}$$
$$2Cr + 3CO_2 \rightarrow Cr_2O_3 + 2CO + 2.8MJ / kg_{Cr}$$
$$Fe + H_2O + 3.0kJ / kg_{Fe} \rightarrow FeO + H_2$$
$$Fe + CO_2 + 480kJ / kg_{Fe} \rightarrow FeO + CO$$
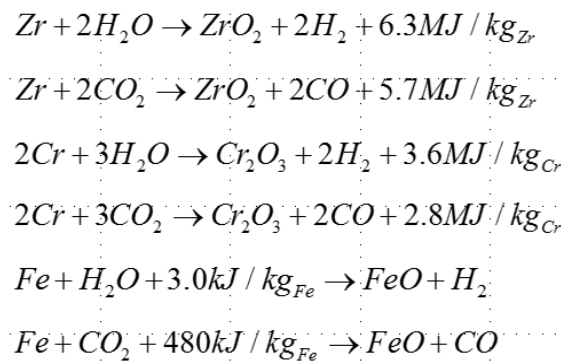
Once the concrete particle melted, the gas would penetrate into the melt pool and interact with the corium. At this time, the thermal release from the chemical reaction will included into the energy equation.

$$\frac{\partial h}{\partial t} = k\nabla^2 T + Q_{source} + Q_{chemical} \tag{2-27}$$

where Q_{source} is the source heat released from decay power, and $Q_{chemical}$ is the thermal released from chemical reaction.

2.4.3. Gas generation model

The gas release from the concrete decomposition would penetrate into the melt pool and interact with the metal in the corium. The mixture would be well stirred by the rising bubbles. Besides, the moving particles will carry out the thermal from the melt pool, which means it would enhance the heat transfer during the MCCI process. Thus, it is important to include the gas generation model to make the simulation more reliable.

The gas generation model were avoided in the previous MPS simulation because the big density difference between the liquid and bubble will lead to some error when the momentum equation is solved. Therefore in this research, the model will not exactly calculate the bubble movement by solving the momentum equation, but focusing on emulate the physical phenomena in the MCCI process.

In this model, as shown in Figure 2-8, once the concrete melt, another two new gas particle (CO_2 and H_2O) would be generated. The mass of the gas particle can be calculated by the particle mass and concrete composition (detail equations can be seen in Chapter 4). These particles are assumed to penetrate into the melt pool and interact with the metallic. Thus, the particles would be transformed to reducing gas (CO and H_2) and rising in the corium pool. The mass of these particles can be calculated by the mass of decomposition gas (CO_2 and H_2O) and corium composition.

As shown in Figure 2-9, all the bubble particles are putted into three channels and rise only through the channels. Three channels model are selected in order to not only considered the gas effective near central line, but also near the side wall boundary. All H_2 particles are putted in the central channel, while the CO particles are putted in the channels near the side wall. The momentum equation will not be solved for gas particles to avoid the calculation error. The buoyancy of the bubbles would be solved by Eq.2-22.
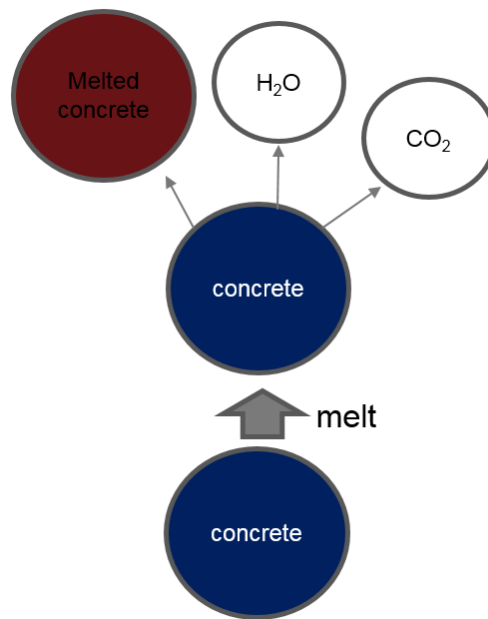
Figure 2-8. Gas bubble particle generation.
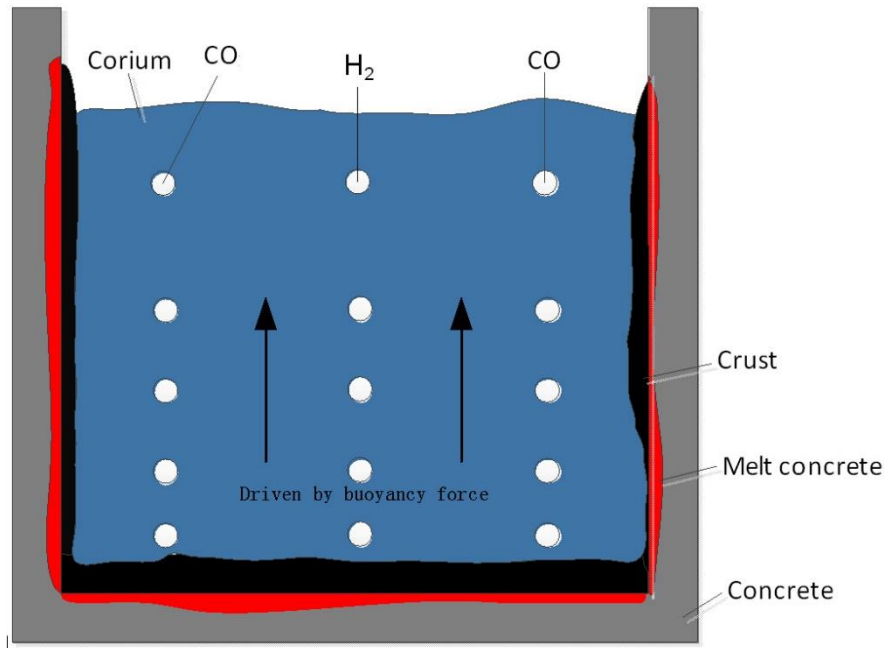
Figure 2-9. Concept of the gas channels
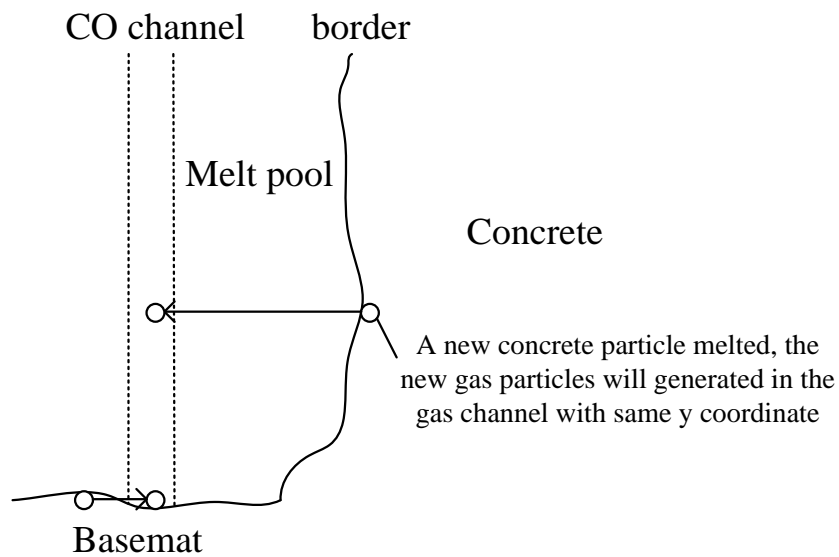
Figure 2-10. Initial position of the gas bubbles in the melt pool.

Figure 2-10 shows the approach to setup the initial coordinate of the gas particles in this model. Once a basement concrete melt, the gas particle will move from the bottom of the corium. While if the concrete is from sidewall, the gas particle will putted as the same height as the concrete particle since the gas will never going downward.
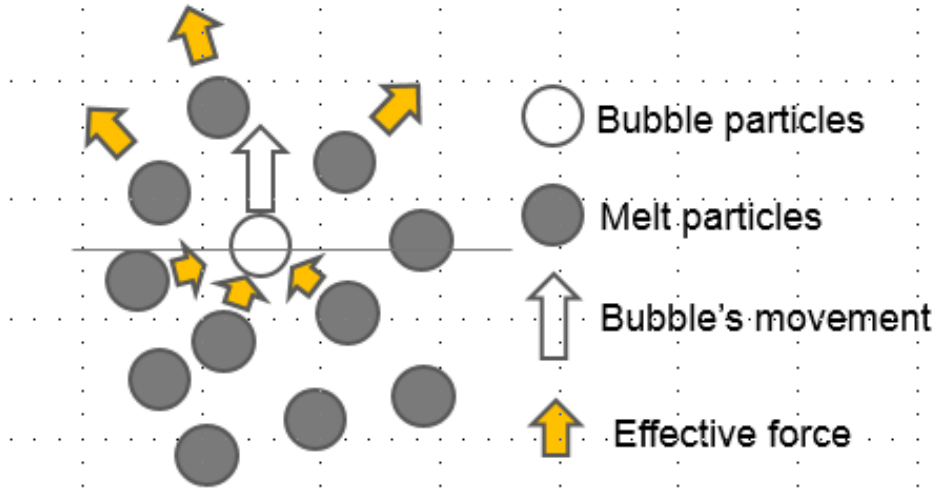
Figure 2-11. Effective force from the bubbles to liquid.

The melt pool is stirred by the force imposed from the gas bubbles. This effective force is calculated similar as the surface tension model introduced before.

$$\rho\frac{d\boldsymbol{u}}{dt} = C(r_{ij} - r_{\min})(r_{ij} - r_e)\frac{(\boldsymbol{r}_j - \boldsymbol{r}_i)}{r_{ij}} \qquad (2\text{-}28)$$

where

$$C = \begin{cases} 0.01 \times p(r) & y_i > y_{gas} \\ -0.001 \times p(r) & y_i \le y_{gas} \end{cases} \qquad (2\text{-}29)$$

where $p(r)$ is the weight function, which equal to

$$p(r) = \frac{1}{3}(r - \frac{3}{2}r_{\min} + \frac{1}{2}r_e)(r - r_e)^2 \qquad (2\text{-}30)$$

The energy equation (Eq. 2-3) is solved between gas bubbles and liquid melt to calculate the heat transfer between them. The detail will be discussed in Chapter 4.

2.5. Flow chart

Figure 2-12 summarize the flow chart of the simulation. The right side is the original MPS method algorithms and left side is the new insert multi-physics models. All the new models are inserted to the beginning of the main loop.
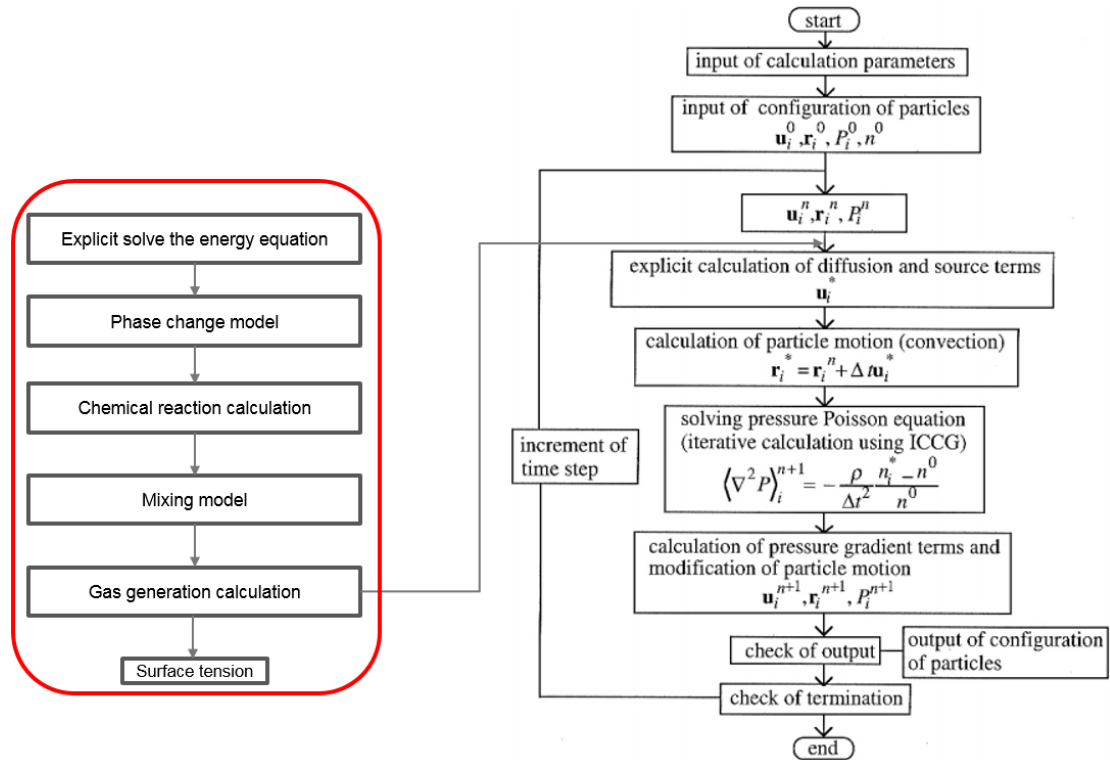
Figure 2-12. Flow chart of the simulation.

3. Verification and Validation

3.1. Outline

Heat transfer and phase change plays a very important role on MCCI process. These two models have already applied in some previous simulations [34, 38-41], which validate these two models are available in some field of engineering analysis. However, validation for such pool molten metal ablation process is required in this research. Besides, a number of experiments and numerical simulations have been conducted to investigate natural convection in the melt pool [51-53]. The results obtained show that it is foundationally important to analyze the heat transfer inside the corium[54]. Besides, Koshizuka's research indicate that it shows totally different crust shape after the natural circulation was considered in the simulation[30]. Therefore, it is Essential to discuss the feasibility of natural circulation model in MPS method.

In this chapter, verification of heat transfer model and phase change model is performed by comparing with the analytical results of semi-infinity board problem. The verification of Natural circulation conducted by S.Zhang [54, 55] is introduced. To validate these models are available on MCCI process, three experiments are simulated by using these models.

3.2. Verification

3.2.1. Heat transfer model

➢ One dimensional semi-infinity board

One dimensional semi-infinity board is a classics problem on thermal conductive calculation. The geometry of the calculation is shown as Figure 3-1. There is a semi-infinity board with a cold plate at the bottom. The size of the board is set to be 60 x 20 mm. This board has a uniform temperature distribution at the beginning.
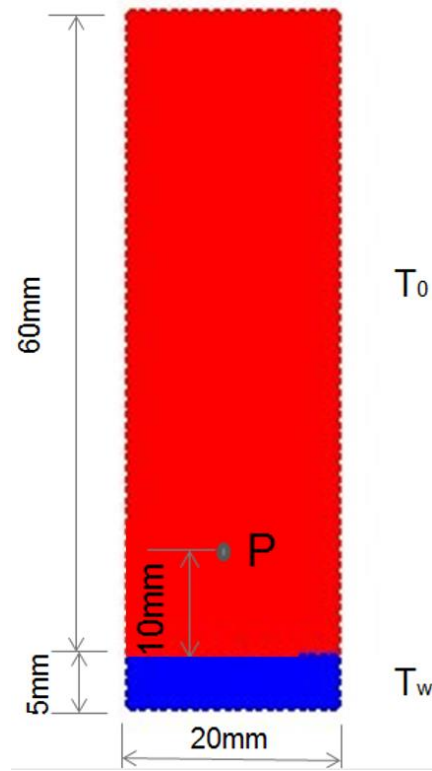
Figure 3-1. Geometry of the semi-infinity case.

Once the simulation start, the cold plate at the bottom would start to cool down the board. The board and the cold plate have the same material composition and properties. As a measure point, point P is installed at the position 10mm higher than the bottom. The initial temperature of the semi-infinity board T_0 and the cold plate T_w are 363K and 263K, respectively. To keep the same boundary condition as the analytical solution, the temperature of the cold plate would keep constant through the whole calculation. The total particles' number of the board and cold plate are 1200 and 100, respectively. The diameter of the particles is 1mm. The material properties used in this simulation are stated in Table 3-1.

Table 3-1. Material properties used in the simulation

Density(kg / m^3)	Specific heat($J \cdot kg^{-1} \cdot K^{-1}$)	Thermal conductivity($W \cdot m^{-1} \cdot K^{-1}$)
998.0	4.2 x 10^3	0.65

The analytical solution of this problem is

$$\frac{T(x,\tau)-T_w}{T_0-T_w} = erf(\frac{x}{2\sqrt{a\tau}}) \qquad \text{(3-1) [56]}$$

where x is the distance from the interface between the board and cold plate; $T(x,\tau)$ is the temperature at the x position in τ second; T_w is the cold plate's temperature; T_0 is the initial temperature of the semi-infinity board; a is the thermal diffusivity.
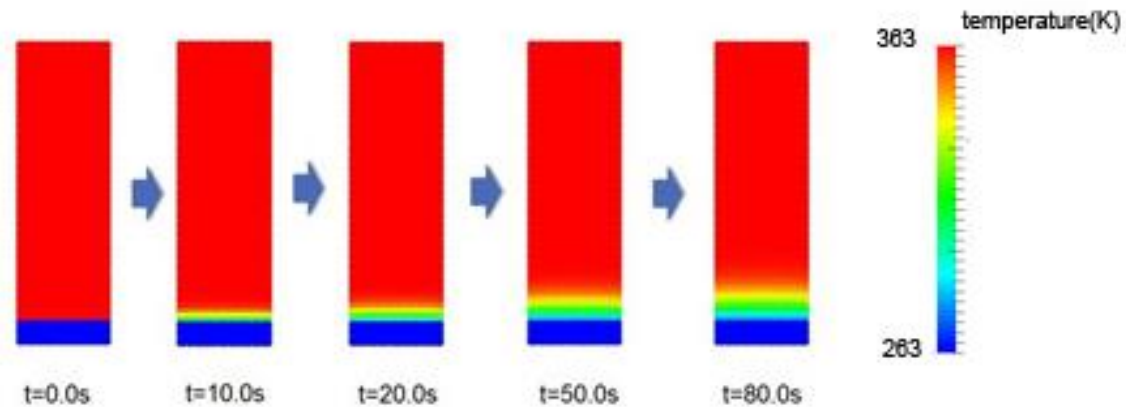
Figure 3-2. Temperature distribution along the elapse time.

Figure 3-2 shows the temperature distribution along the elapse time. The board is cool down by the cold plate at the bottom. The temperature diffusion didn't reach the top part, which means it satisfies the semi-infinity problem's requirement.
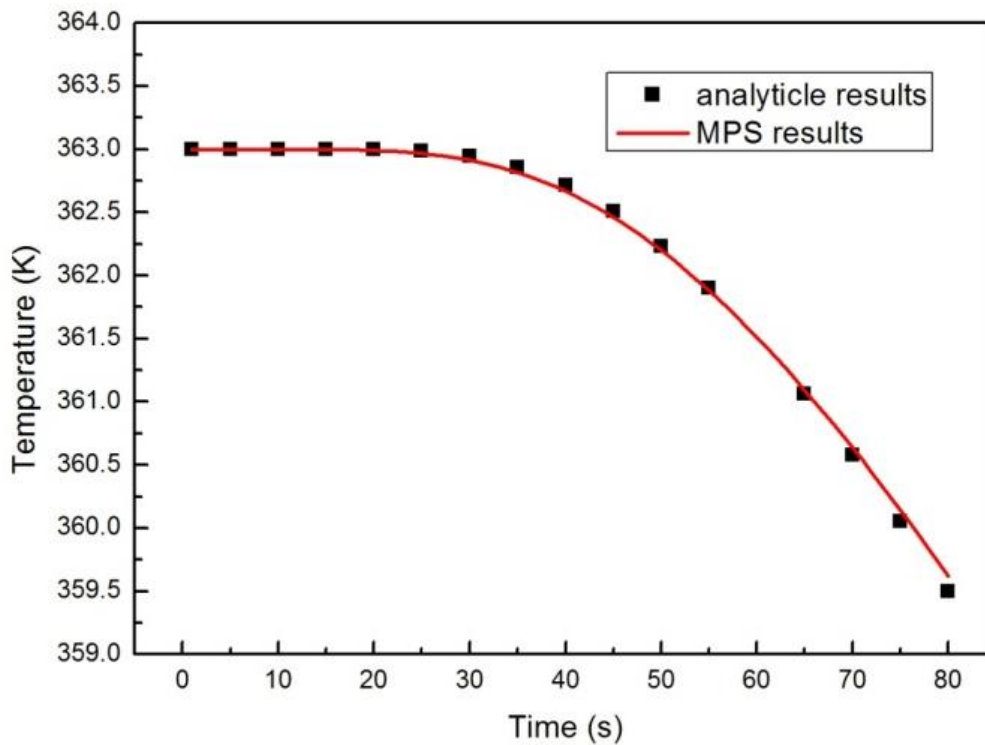
Figure 3-3. Comparison between the analytical results and MPS method.

To verify the model, the temperature of point P was calculated using Eq. 3-1 and compare with the simulation results. As shown in Figure 3-3, perfect match can be seen from this comparison.

➤ Double semi-infinity board

Since the heat transfer in the real case is not just one direction, but both way heat transfer. Thus, another verification with two semi-infinity board was conducted. As shown in Figure 3-4, two steel plate with different temperature are contacted with each other. The initial temperature of hot plate and cold plate are 80 ℃ and 10 ℃, respectively. The total particles' number of both board are 1000. The diameter of the particles is 1mm. The material properties used in this simulation are stated in Table 3-2.
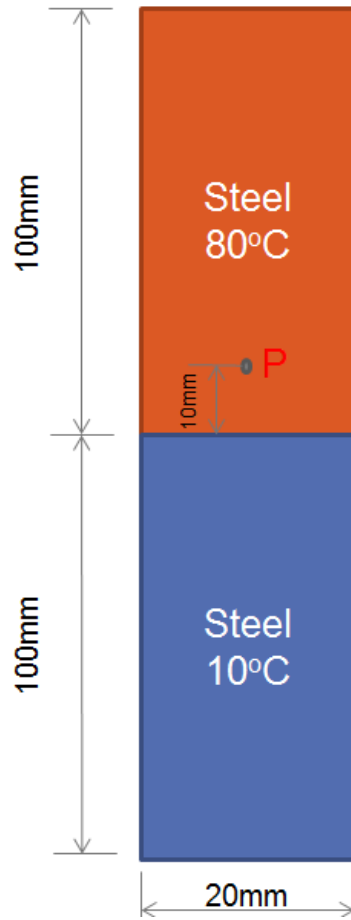
Figure 3-4. Two semi-infinity board.

Table 3-2. Material properties used in the simulation

Density(kg/m^3)	Specific heat($J \cdot kg^{-1} \cdot K^{-1}$)	Thermal conductivity($W \cdot m^{-1} \cdot K^{-1}$)
7850.0	444.0	80.0

This issue can be solved by the following equations

$$
\begin{cases}
T(x) = T_1 + (T_s - T_1)[1 - erf(\dfrac{x}{2\sqrt{\alpha_1 \tau}}) \\[4mm]
T(x) = T_2 + (T_s - T_2)[1 - erf(\dfrac{x}{2\sqrt{\alpha_2 \tau}}) \\[4mm]
T_s = \dfrac{\sqrt{\rho_1 c_1 k_1} T_1 + \sqrt{\rho_2 c_2 k_2} T_2}{\sqrt{\rho_1 c_1 k_1} + \sqrt{\rho_2 c_2 k_2}}
\end{cases}
\qquad (3\text{-}2)[56]
$$

where x is the distance between the point and the interface; $T(x)$ is the temperature of this point; T_s is the relative temperature for calculation; subscript 1 and 2 represent the properties of the first and second board, respectively.

Figure 3-5 shows the temperature distribution of both semi-infinity board. Perfect match against analytical results can be observed. As the previous simulation, the temperature diffusion does not reach the end of the board, thus this board can be seems as a semi-infinity board.
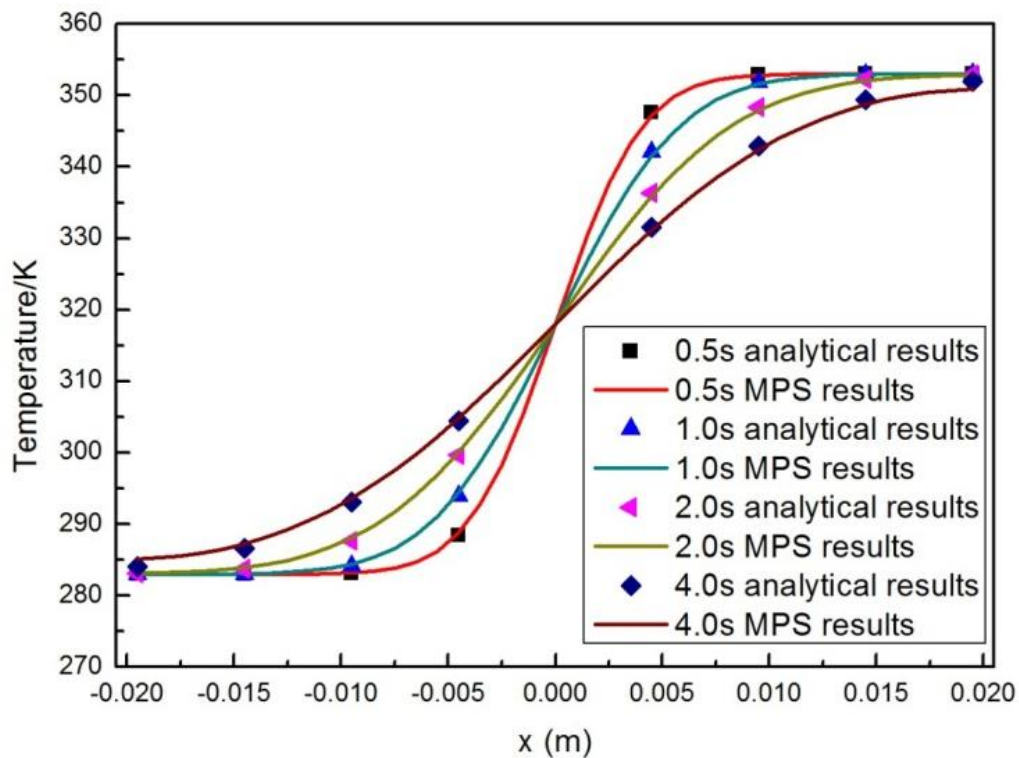
Figure 3-5. Temperature distribution in double semi-infinity board.

Figure 3-6 compare the temperature of the point P calculated from the MPS method and analytical solution. Good agreement can be seen.
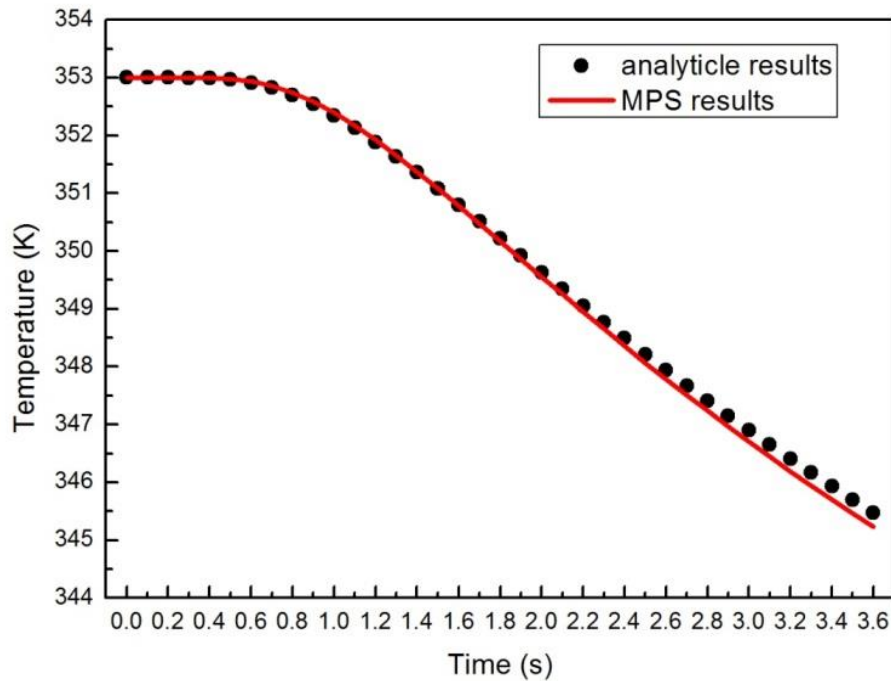
Figure 3-6. Comparison of the temperature of point P.

From the discussion above, it can be concluded that this heat transfer model is available for such immobile semi-infinity case.

3.2.2. Phase change model

● Neumann problem

The first analytical phase change problem is solved by Stefan[57], where the single phase are "active", the other phases are just kept on the melting temperature. Neumann extend the Stefan's solution to two-phase problem. The initial phase of the material is assumed to be solid, which is heated up and melt by a hot plate from one side. The thermos-physical properties are assumed as a constant.

In this paper, only final Neumann's solution is stated in the following text. More detail about the Neumann method can be found in[58].

Interface position can be calculated by

$$X(t) = 2\lambda\sqrt{a_l t} \qquad (3\text{-}3)$$

where $X(t)$ is the position of interface at t second; λ is the dimensionless number for Neumann method; a_l is the thermal diffusivity of the liquid phase.

where λ can be calculated by

$$\frac{St_l}{\exp(\lambda^2)erf(\lambda)} - \frac{St_s\sqrt{a_s}}{\sqrt{a_l}\exp(a_l\lambda^2/a_s)erfc(\lambda\sqrt{a_l/a_s})} = \lambda\sqrt{\pi} \quad (3\text{-}4)$$

where

$$St_l = \frac{C_l(T_l - T_m)}{H_f} \qquad (3\text{-}5)$$

$$St_s = \frac{C_s(T_m - T_s)}{H_f} \qquad (3\text{-}6)$$

The temperature in the liquid phase can be calculated by

$$T(x,t) = T_l - (T_l - T_m)\frac{erf(x/2\sqrt{a_l t})}{erf\lambda} \qquad (3\text{-}7)$$

The temperature in the solid phase can be calculated by

$$T(x,t) = T_s - (T_m - T_s)\frac{erfc(x/2\sqrt{a_s t})}{erfc(\lambda\sqrt{a_l/a_s})} \qquad (3\text{-}8)$$

Based on the Neumann problem, a rectangular semi-infinity region is configured as Figure 3-7. The semi-infinity domain and the hot plate are represented by the green and black particles, respectively. The length of the domain is 40 x 20mm, while the hot plate is 3 x 20mm. The initial temperature of the board and hot plate are 270K and

300K, respectively. The melting point of the board is 273K. The board will be heated up by hot plate and gradually melt. To satisfy the Neumann problem, the temperature of the hot plate will keep constant. There are 800 particles for semi-infinity board and 60 particles for hot plate. The particle's diameter is 1mm. The material properties are stated in Table 3-3.
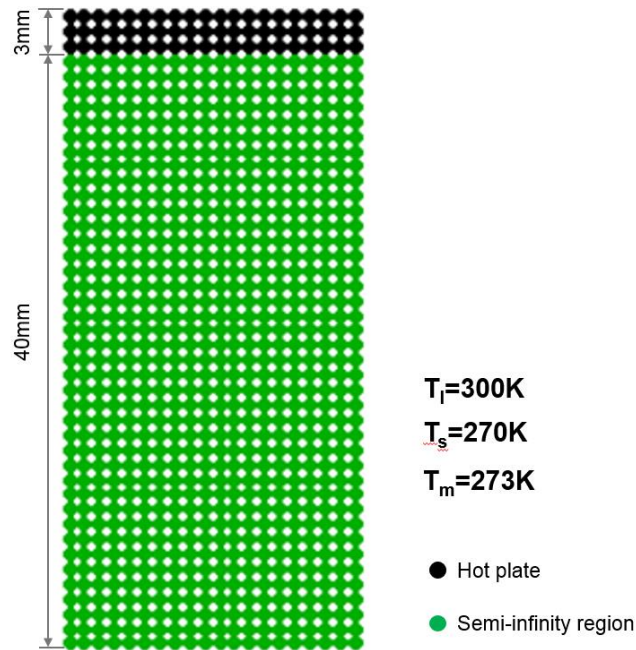
Figure 3-7. Configuration of the simulation.

Table 3-3. Material properties used in the simulation

Properties	Value
Density(kg / m^3)	998.0
Specific heat($J \cdot kg^{-1} \cdot K^{-1}$)	4200.0
Thermal conductivity($W \cdot m^{-1} \cdot K^{-1}$)	0.65
Melting point (K)	273.0
Latent heat (kJ / kg)	334.0

Figure 3-8 shows the erosion process calculated by MPS method. The solid particles from rectangle board were heated up by the hot particles at the top and gradually melted downward. The melted particles are represented by the pink particles. Figure 3-9 shows the temperature distribution along the elapse time.

To verify the phase change model, the temperature calculated by MPS method is compared with the analytical results. From the Figure 3-10, both ablation depth and temperature distribution shows perfect match with the analytical results. Therefore, MPS method is verified as a proper tool to calculate the phase change problem.
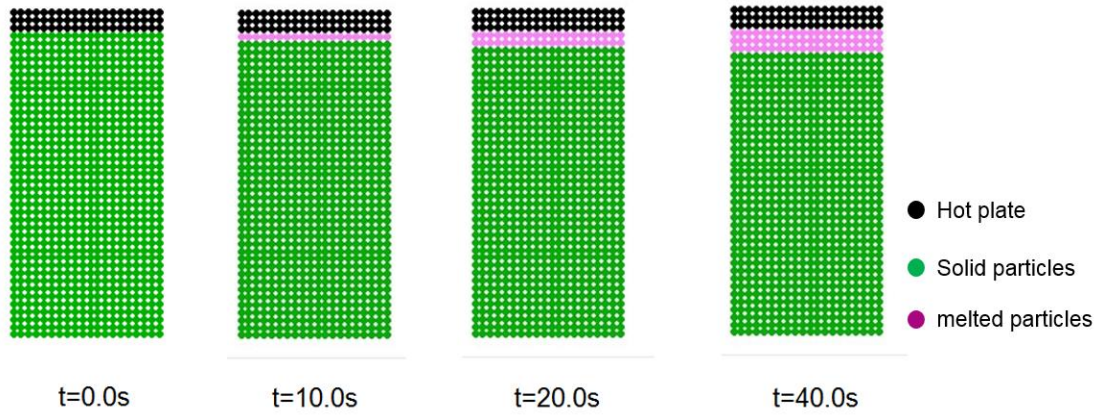
Figure 3-8. The melt process calculate by MPS method.
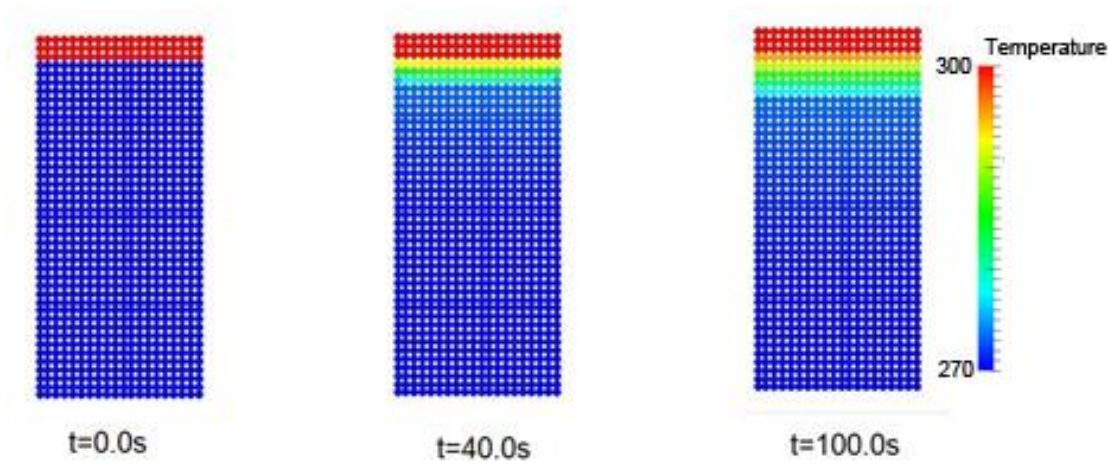
Figure 3-9. Temperature distribution along the elapse time.
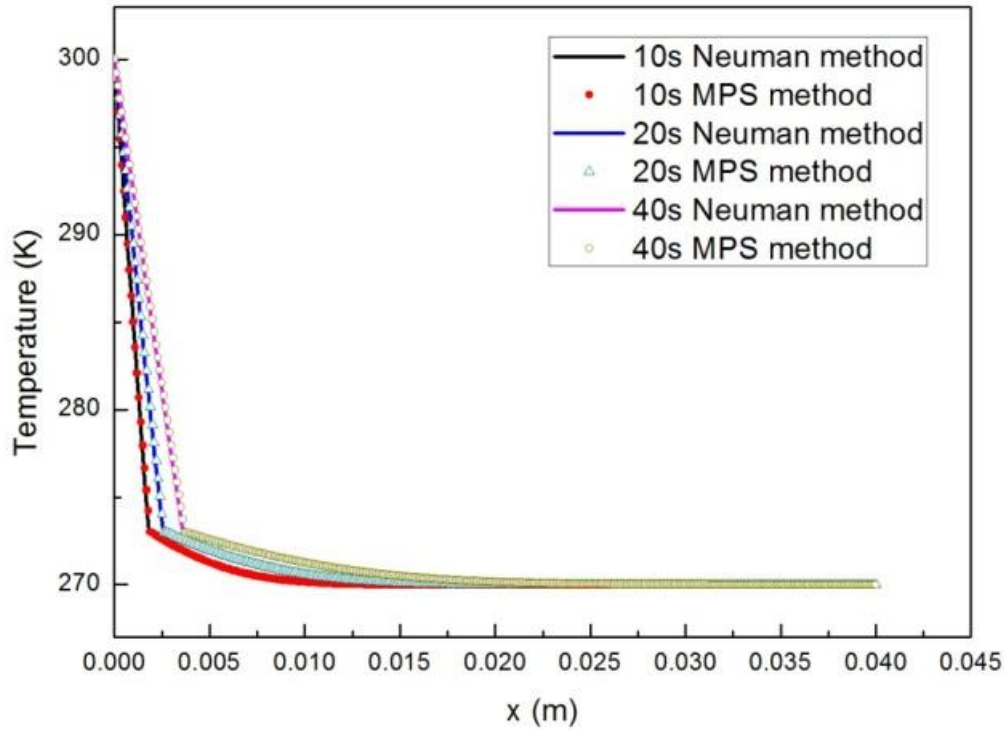
Figure 3-11. Temperature distribution and melt depth.

3.2.3.Natural circulation model

Verification of natural circulation model has been performed by S. Zhang[55]. The geometry is shown in Figure 3-12, the square calculation region is heated up from left side and cooled down from right side, adiabatic boundary conditions set up on the top and bottom.

The trend of the natural circulation is controlled by a non-dimensional number, Ra number

$$Ra = \frac{g\beta\Delta T W^3}{\upsilon\alpha} \qquad (4\text{-}1)$$

where g is gravitational acceleration; β is the thermal expansion coefficient; ΔT is the temperature difference; W is the character length; υ is viscosity; α is thermal diffusivity.

Adiabatic

Hot wall   Fluid   Cold wall

Adiabatic
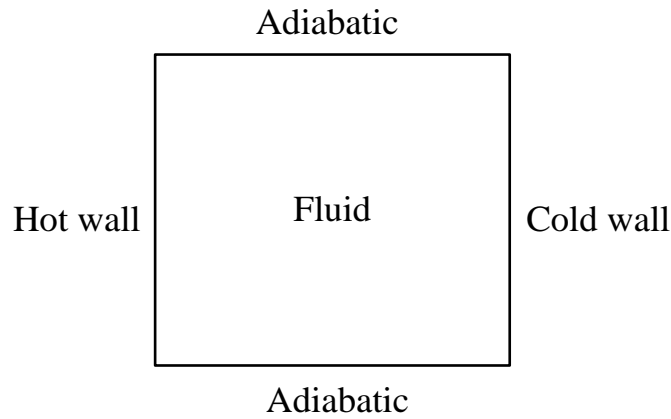
Figure 3-12. Geometry of the calculation.

The isothermal contour under different Ra numbers are shown in Figure 3-13. We can see from the figure that different Ra number contribute different convection behavior.
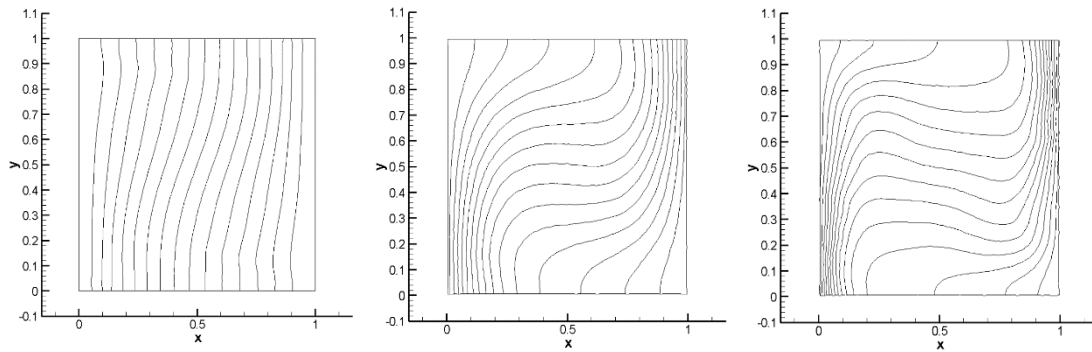
Figure 3-13. isothermal contour with $Ra = 1 \times 10^3$, $Ra = 1 \times 10^4$, $Ra = 1 \times 10^5$.[55]

The average Nusselt number at the boundary is calculated to compare with the benchmark[59]. As shown in Table 3-4, it showed that the MPS method can give excellent results for low and moderate Rayleigh numbers. However, some deterioration exists in the high Rayleigh number condition, which suggests a smaller

temperature gradient than the analytical results. Quantitatively, the results deteriorate and the error is about 11% under $Ra = 1 \times 10^5$. Besides MPS method, it also shows the similar results in SPH method simulation[60].

Table 3-4. Comparison of benchmark and MPS method[55]

	$Ra = 1 \times 10^3$	$Ra = 1 \times 10^4$	$Ra = 1 \times 10^5$
Benchmark[59]	1.117	2.238	4.509
MPS	1.138	2.191	3.965

3.3. Validation

Except the verification, MPS method is required to validate against the MCCI experiment to prove its availability for its investigation. However, visualizing it in large-scale experiments is virtually impossible because of the extreme experimental conditions. Furthermore, the setting of the experiment to test the ablation of concrete in MCCI phenomena is costly and requires high-level safety procedures. Thus, a simple alternative experiment at low temperatures using u-alloy and transparent materials was performed aiming to validate the feasibility of heat transfer and phase change models. Besides, another two experiment conducted in 1980s is simulated to validate the natural circulation model.

3.3.1. Wax experiment

The final objective of this research is to investigate MCCI process. Thus, u-alloy and gel wax were selected to emulate the molten corium and concrete. The reason of this selection is:

➢ U-alloy is suitable to emulate the molten metallic because of its low melting temperature.

➢ It allows us to visualize the ablation process since the gel wax is transparent.

> The density ratio between u-alloy and gel wax is 2.70, which is sufficiently close to the ratio between corium and concrete, which is 3.42.

A schematic view of the experimental apparatus is shown in Fig. 3-14. The gel wax was contained in a transparent glass container with dimensions 7 cm $\times$ 7 cm $\times$ 6 cm. Unlike the large-scale MCCI experiment, the experiment proceeded under pure dry cavity conditions for the code validation purpose. Initially, u-alloy was heated in the hotpot until 190°C, while the temperature of the gel wax was 20°C. Then, the melted u-alloy was poured into the cylindrical cavity at the center of the pool made of gel wax. Ablation immediately began right after the pouring. The ablation movement was captured by a high-speed camera at a rate of 2 fps. The temperature was measured with three K-type thermal-couples at locations (-1.0 cm, 0.5 cm), (-1.0 cm, 1.8 cm), and (0 cm, 3.5 cm). The data acquisition was carried out using a data logging system at a frame rate of 1 fps.
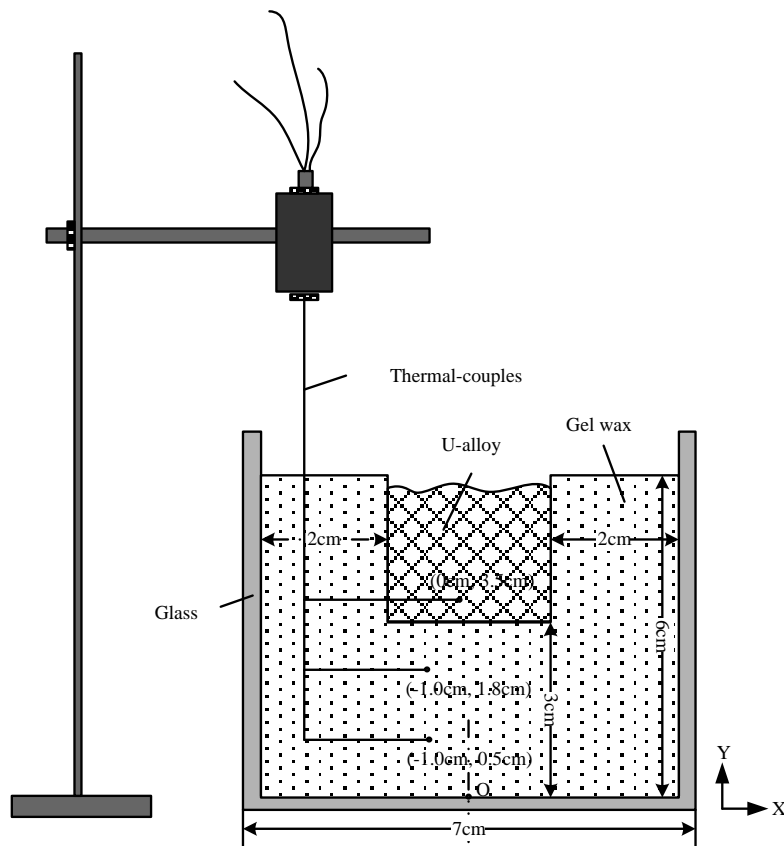
Figure 3-14. Principle-view of the experimental apparatus.

A two-dimensional domain was established to simulate the experiment by the MPS method, as shown in Figure 3-15. There are three types of particles, represented by blue, green, and red, they are u-alloy particles, gel-wax particles, and wall particles, respectively. The representative material did not change throughout the calculation and it ensured the conservation of mass and heat. The wall particles were only used to calculate the particle number densities. Because they did not exchange heat with the inner particles, the wall was modeled adiabatically in this simulation. To express the phase change of the gel wax, each gel-wax particle was judged to be either fluid or solid in every time step. The fluid particles' movement was calculated by solving the momentum equation, while the solid particles were fixed in the previous position. The initial simulation condition is shown in Table 3-5, and the material properties [61-63] used in the code are shown in Table 3-6.
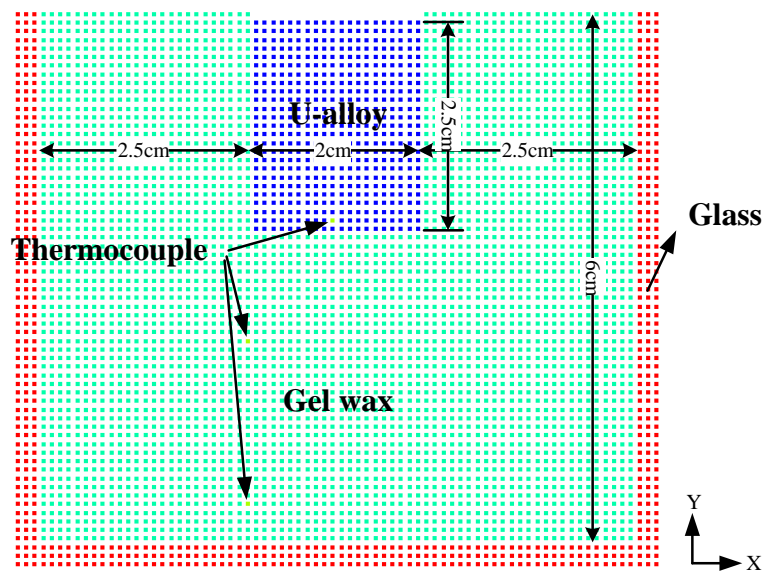
Figure 3-15. Initial particle configuration.

Table 3-5. Initial condition of the simulation

Parameter	Value
Initial temperature of gel wax (K)	293.0
Initial temperature of u-alloy (K)	464.0
Average distance between particles (m)	0.001
Total number of particles	9126

Table 3-6. Physical properties of materials utilized

Property	U-alloy	Gel wax	Glass
Density (g/m^3)	9580.0	3550.0	2300.0
Thermal conductivity ($W/m \cdot K$)	36.0	0.4	1.09
Specific heat ($J/(kg \cdot {}^oC)$)	790.0	780.0	600.0
Latent heat (J/kg)	45800.0	43700.0	-
Melting point (${}^oC$)	70.0	50.0	2000.0

The profile of the metal deformation process can be seen in the pictures in Figure 3-16. The process can be divided into two main stages. From the very beginning to around 80s, the ablation process is nearly homogenous because of the uniform temperature distribution of the melt pool. In addition, crust is generated after around 60s in the bottom of the melt, which reduces the heat transfer between the molten metal and gel wax. The second stage is from 80s; molten metal gains its final shape after some time and continues its downward motion while preserving its shape. This is because of the heat sink effect from the gel; the surface temperature is reduced until

the solidification point of the u-alloy. Therefore, a shell is gradually generated and surrounds the melting material. However, the ablation process does not stop because the surface temperature is still higher than the melting point of gel wax. The final melting depth in the central line was 2.2 cm.

Figure 3-17 is a series of pictures that compares the ablation profile between the simulation and the experiment at three time points. In order to clearly compare the molten metal deformation process with the experiment, the particles are represented by their material type. From the pictures it is clear that the ablation profile simulated by the MPS method is congruent with the experiment.

Figure 3-18 compares the erosion front head, with both axial and radial direction, of the experiment and the MPS method. A good agreement on both the downward and sideward ablation can be seen in the picture. The liquid metal melted the wax almost homogenously. The ratio of axial and lateral ablation at the end is 1.27, which is very similar to the experimental results. The ablation speed is seen gradually decreasing as the time elapses.
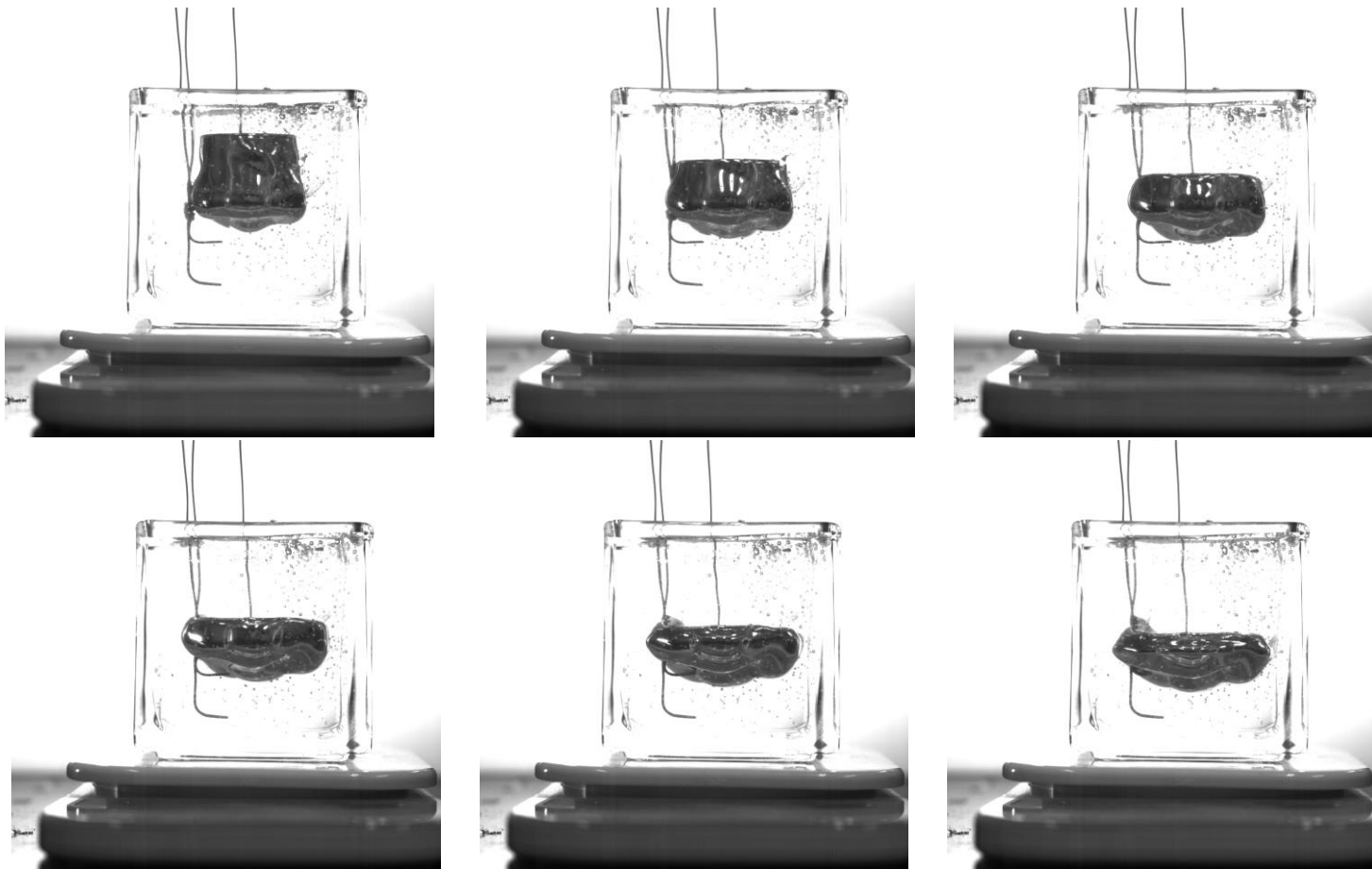
Figure 3-16. Ablation process and metal deformation (First line, from left to right: 5 s, 20 s, 40 s; Second line, from left to right: 60 s, 80 s, 100 s.)
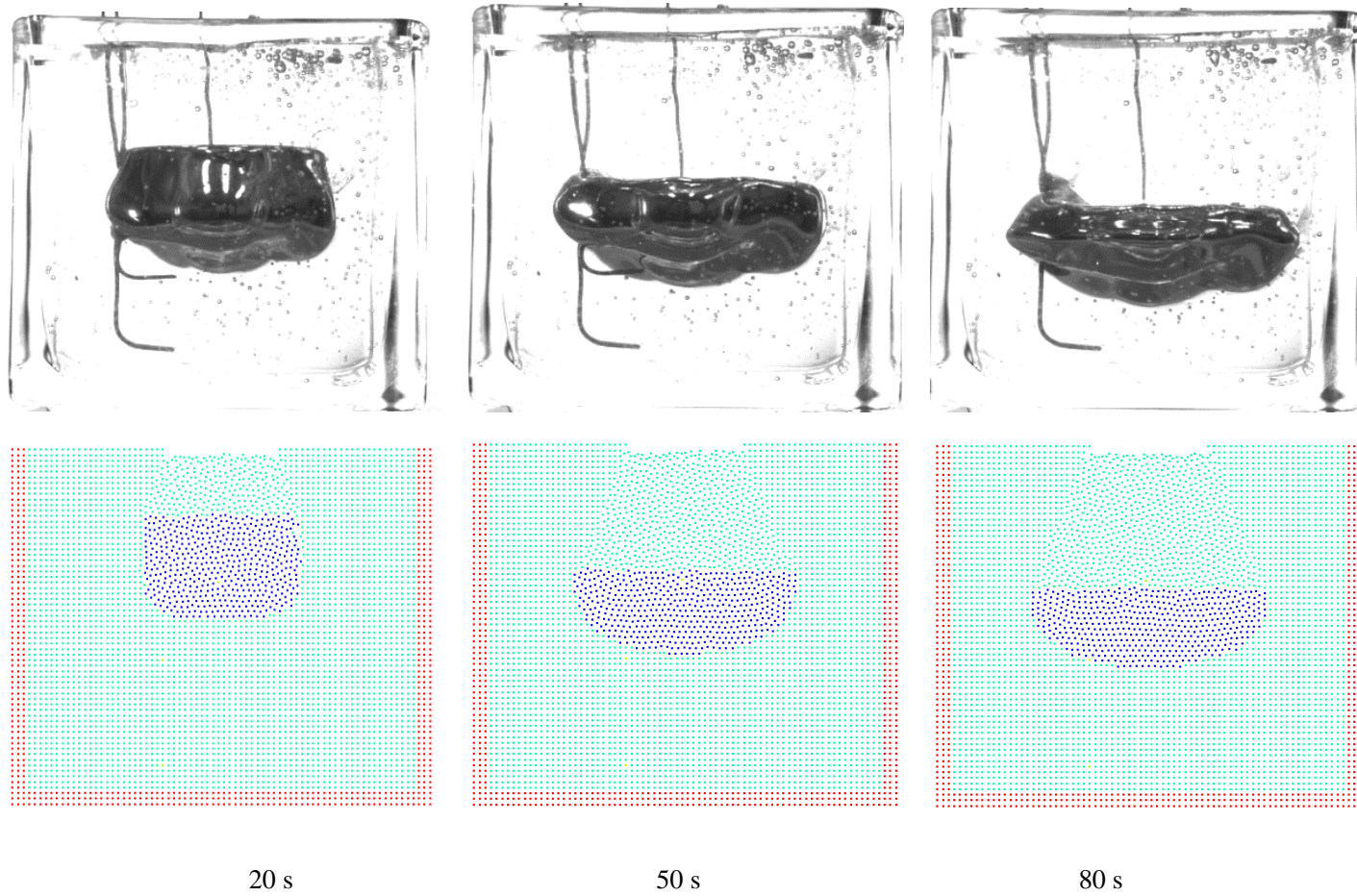
20 s   50 s   80 s

Figure 3-17. Ablation profile comparison between simulation and the experiment at 20 s, 50 s, 80 s.
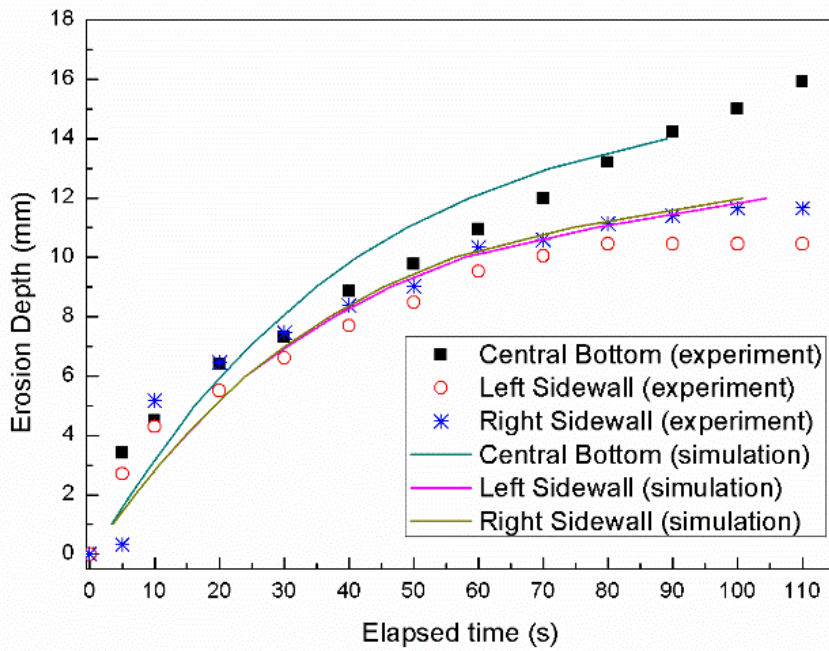
Figure 3-18. Erosion front head during the ablation process.
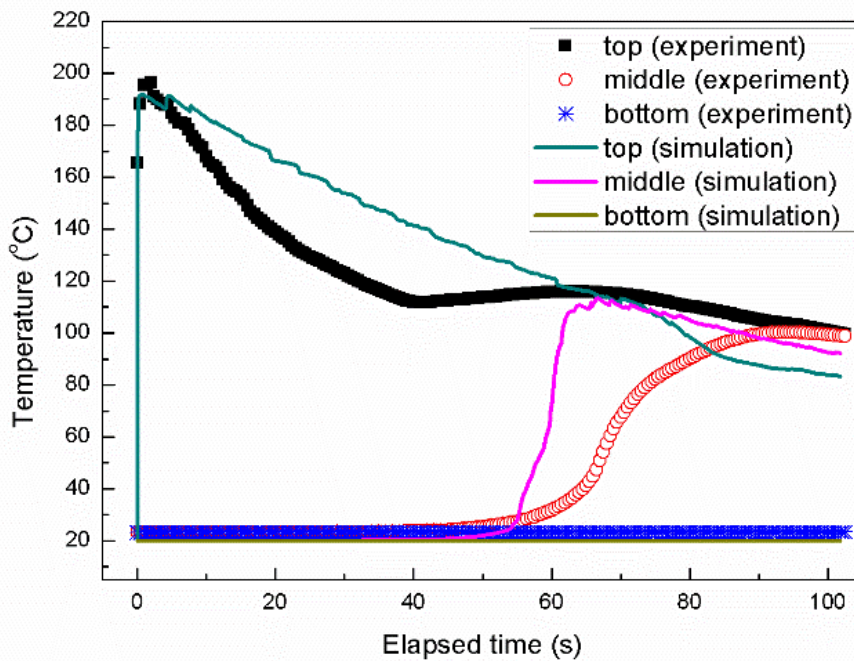
Figure 3-20. Temperature of the thermocouples.
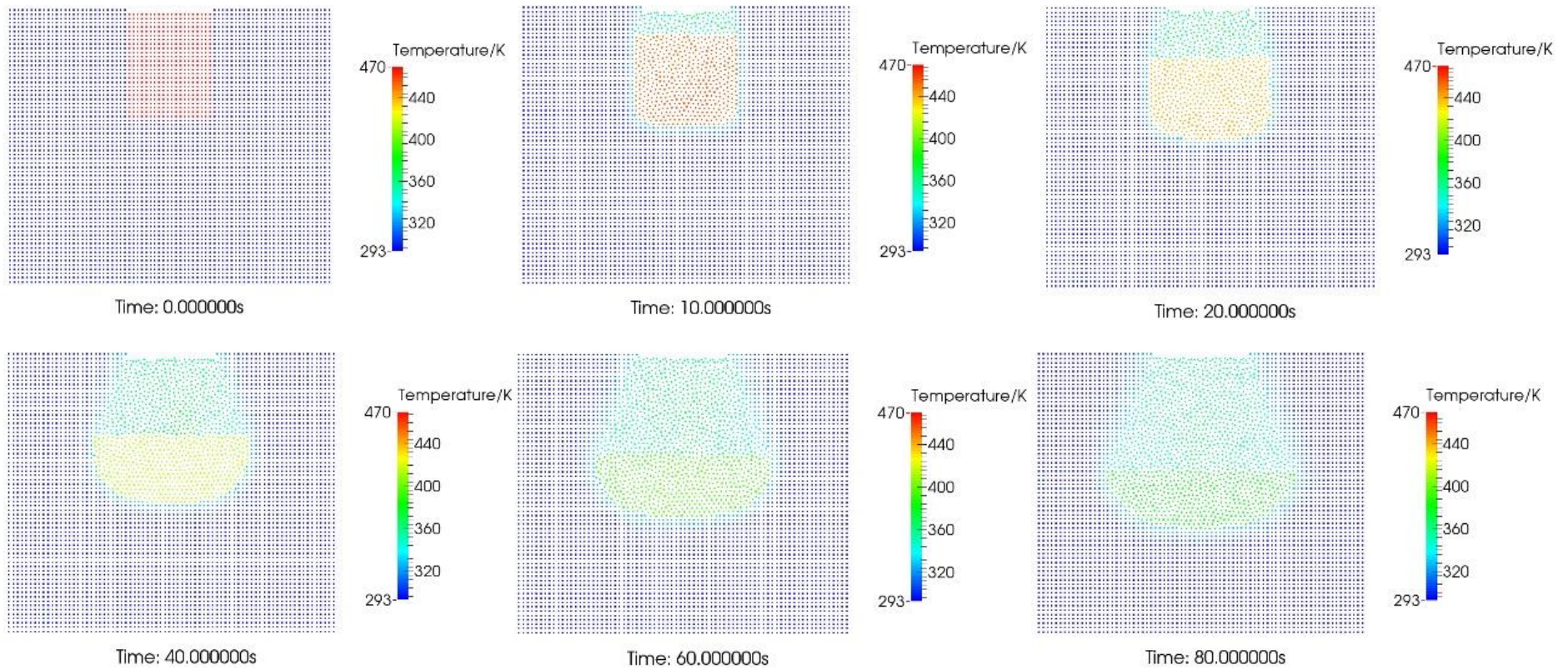
Figure 3-19. Temperature changes with elapsed time.

Figure 3-19 is a series of pictures showing the temperature distribution of the whole domain with elapsed time in the simulation. It can be seen from the pictures that the temperature of u-alloy decreased because of the heat sink effect from the gel wax. In addition, a very small temperature diffusion appears as a result of the low thermal conductivity of gel wax. Figure 3-20 gives a comparison of the temperature measured by the thermocouples and the temperature calculated by the MPS method at the same place. It can be seen that in the experiment, the temperature of the top thermocouple decreased rapidly for the first 30 s, which is because the u-alloy is condensed by the air and the gel wax during the process of being poured into the cavity, which cannot be simulated in the calculation. The molten pool reached the second thermocouple at 58 s in the simulation, which was slightly earlier than in the experiment. Further, the temperature of the second thermocouple rises rapidly because of the low temperature diffusion of gel wax, while the curve of the experiment changes gently, probably because there was some gel wax surrounding the thermocouple when it was heated by the molten pool, and results in deceleration of the melting process in the location of the second thermocouple.

3.3.2. Tin experiment simulation

Tin experiment was performed by Wolf. et.al. in 1988[64], which is aiming to obtain the experimental data of natural convection under the low Plant number condition. The experimental apparatus is shown in Figure 3-21, the test section is constructed based on a normal five-sided Pyrex glass containment with 7mm thick. Some sand was putted onto the bottom of the containment since the height of the tank is higher than the experimental design. Another Pyrex glass was putted onto the sand to separate the sand and molten material. Two lava plate was placed on the tin to keep the isothermal boundary condition. Two heat exchangers were placed on both vertical walls as a heat source. Temperature of the liquid will be measured by the probe insert from the top. In the probe, type K thermocouple wire is inserted into a 3mm O.D. glass tube.

As shown in Figure 3-21 (right), the tin was placed in a rectangular cavity with two vertical side walls at constant but different temperatures. The remaining walls of the cavity were well insulated. The configuration of the simulation, which has the same initial condition as the experiment, is depicted in Figure 3-22. The physical properties of tin and the initial condition of the simulation are listed in Tables 3-7 and 3-8, respectively.

Figure 3-23 compares the isothermal contour of both experiments and the MPS method simulation using non-dimensional values $\xi = x/L$, $\eta = y/H$. A similar trend was obtained on the temperature field.
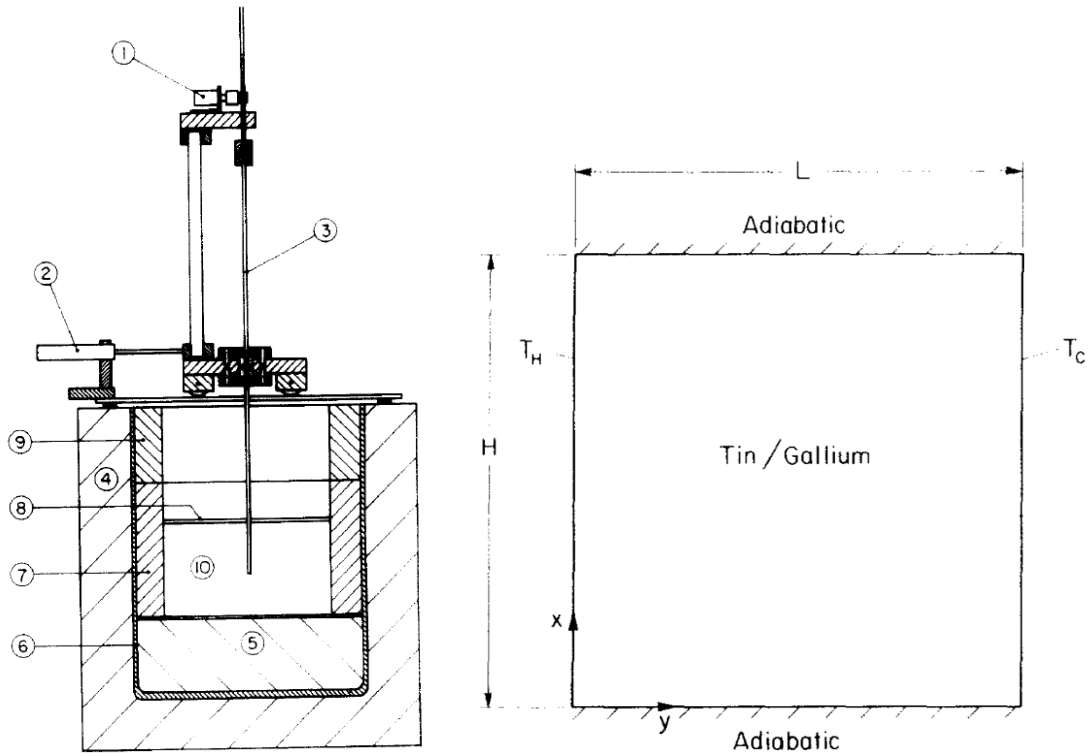
Figure 3-21. Left: The experimental apparatus; Right: the test cavity of the experiment[64].
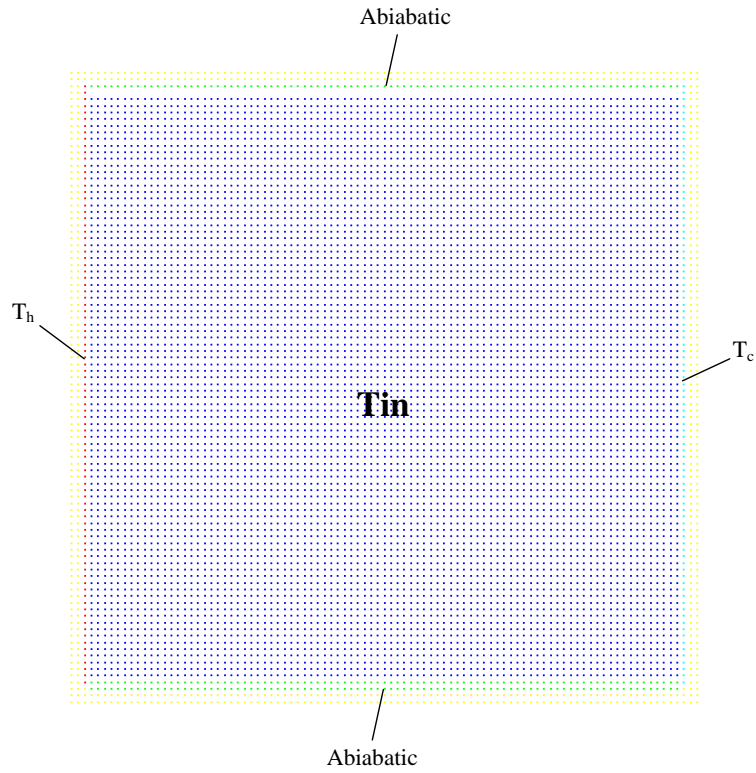
Figure 3-22. Initial geometry of the simulation.

Table 3-7. Material properties used in the simulation

Properties	Value
Density(kg / m^3)	5769.1
Specific heat($J \cdot kg^{-1} \cdot K^{-1}$)	210.0
Thermal conductivity($W \cdot m^{-1} \cdot K^{-1}$)	66.0
Melting point ($^o C$)	231.93
Thermal expansion coefficient ($10^{-6} / K$)	22.0

Table 3-8. Initial condition of the simulation

Parameter	Value
Initial tin temperature (K)	506.2
Hot wall temperature T_h (K)	507.4
Cold wall temperature T_c (K)	505.0
Average distance between particles (m)	0.001
Total number of particles	9126

Figure 3-24 compares the temperature history in three specific places among the experiments, the MPS method and FLUENT, a CFD code assembled in ANSYS software. In the figure, the results are shown using the non-dimensional value $\Theta = \dfrac{T\text{-}T_c}{T_h\text{-}T_c}$. It is clear from the figure that both FLUENT and the MPS method obtain reasonable results. Figure 3-25 shows the velocity field, the hot particles going up on the left, and the cold particles going down near the cold wall on the right.
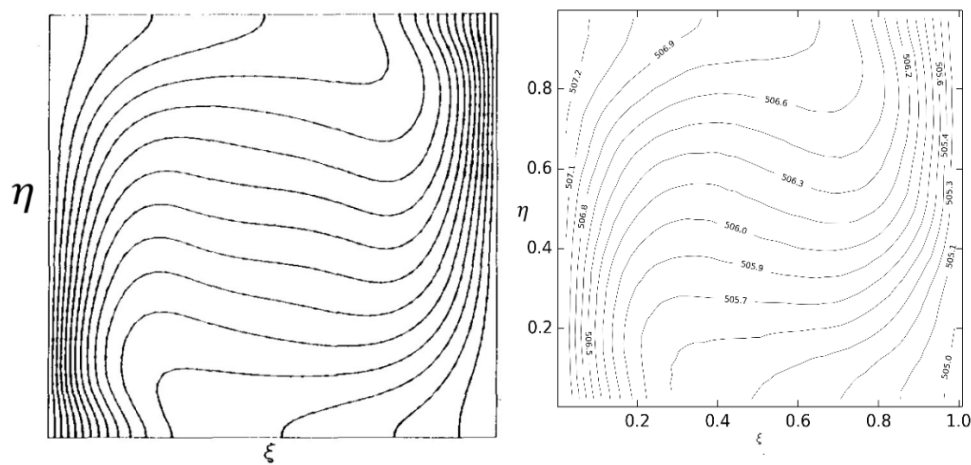
Figure 3-23. Isothermal contour comparison of the experiment: Left: the experiment[64] Right: the MPS simulation.
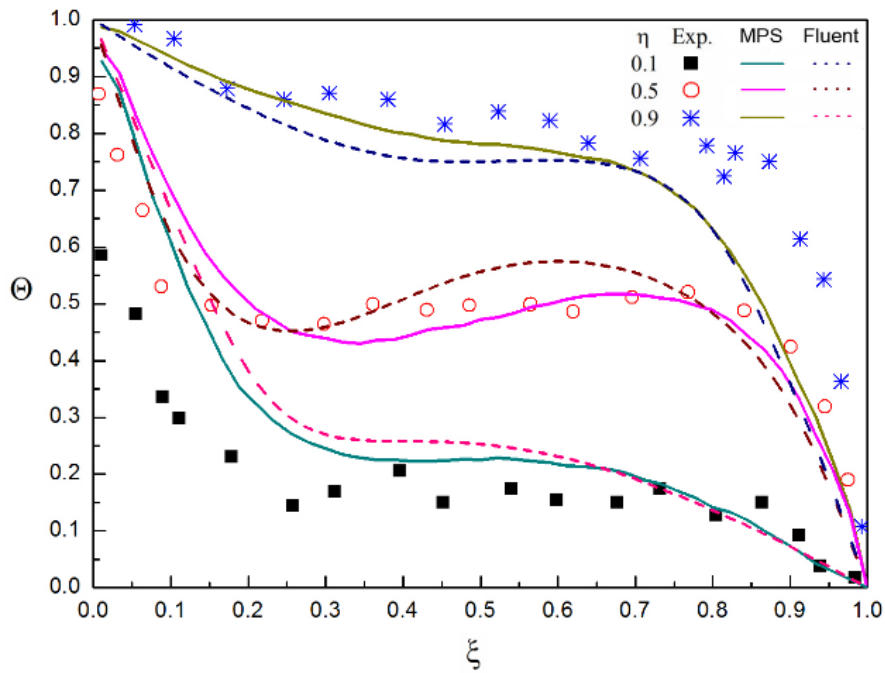
Figure 3-24. Comparison of temperature in three places: the experiment, MPS method, and FLUENT.
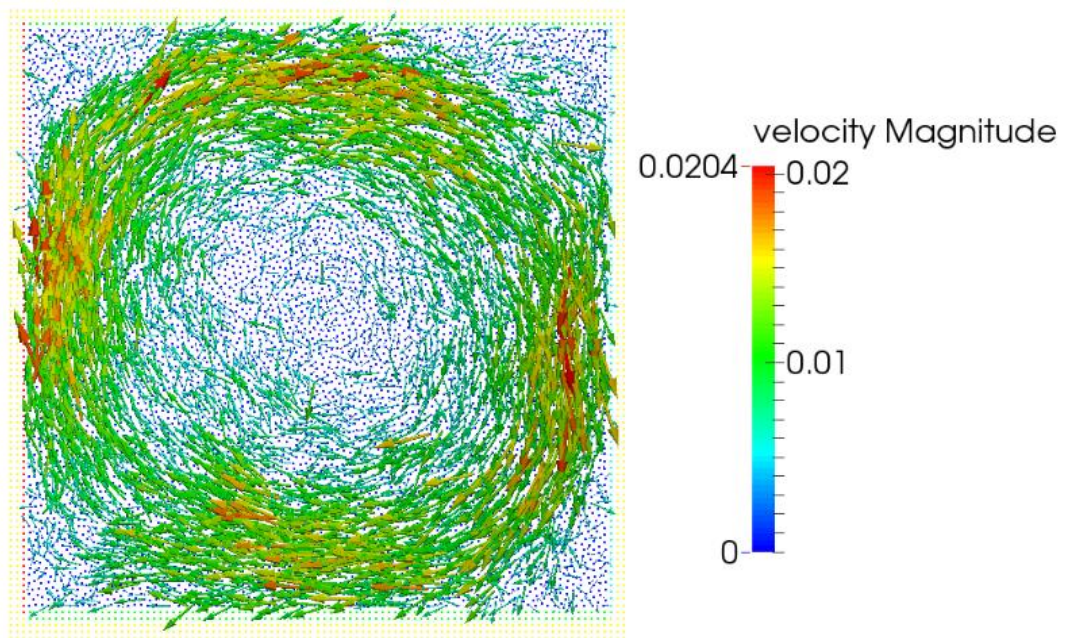
Figure 3-25. Velocity field calculated using the MPS method.

However, differences between the experiment and simulation can be observed from Figure 3-23 and 3-24, especially at the top-right corner and bottom-left corner,

where the large temperature gradient exists. This tendency is similar to the verification calculation done by Zhang[55], that is the temperature gradient is smaller than that in the experiment. Zhang calculated the Nusselt number to estimate the magnitude of the error compared to the analytical results, which is approximately 11% when $Ra = 1 \times 10^5$ [55]. The Rayleigh number in this validation calculation is approximately 3.625×10^5, which is larger than the case in the verification study. Therefore, the error in this study was also larger compared to the tin experiment. This supports the conclusion in the verification work. Specifically, the natural circulation can be appropriately simulated by the MPS method at low Rayleigh numbers, but underestimation occurs when the Rayleigh number is high.

3.3.3.Gallium experiment simulation.

To avoid the accidental error, another experiment with melt process was simulated and be discussed. Gallium experiment was performed by Gau and Viskantain 1986[65]. Similar as tin experiment, a rectangular cavity is heated up from the left wall and cooled down from the right. The top and bottom boundaries are adiabatic. As shown in Figure 3-26, the cavity is 88.9mm wide and 63.6mm high. The simulation is configured as Figure 3-27. The enclosure is represented by green particles while the wall by red. The initial temperature of the enclosure is 28.3°C, and the hot wall keeps a constant temperature of 38.9°C. The physical properties of gallium are shown in Table 3-9. To compare with MPS method, another CFD code based on FVM method is applied on the simulation by KIT[66].
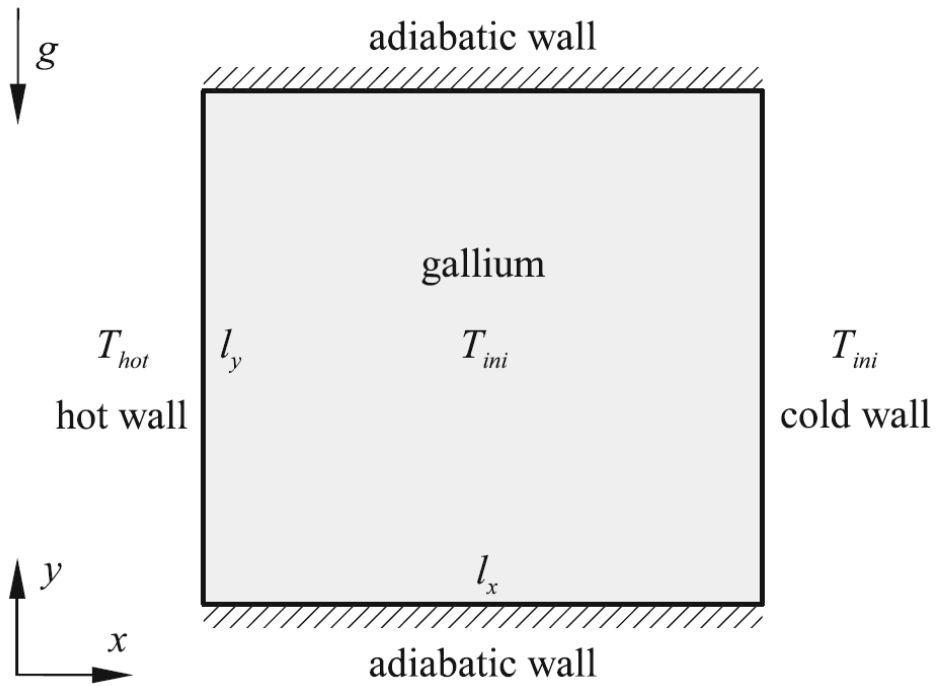
Figure 3-26. Physical model of the gallium experiment[65].

Table 3-9. Thermal properties of Gallium[65].

Properties	Value
Density(kg/m^3)	6093
Specific heat($J \cdot kg^{-1} \cdot K^{-1}$)	381.5
Thermal conductivity($W \cdot m^{-1} \cdot K^{-1}$)	32.0
Melting point (^oC)	29.78
Thermal expansion coefficient ($10^{-6}/K$)	120.0
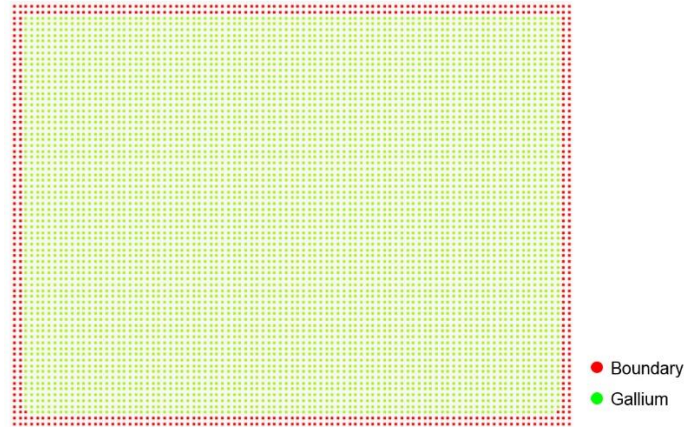
Figure 3-27. Simulation configuration for gallium experiment.

Figure 3-28 shows the melting progress based on the simulation results. Solid gallium is heated up from the left side and melt gradually to the right. Because of natural convection, the hot liquid gallium is staying at the top, which results in a quicker ablation. Figure 3-29 compare the melt speed between the results of the experiment, FVM method[66] and MPS method. Reasonable results from both FVM[66] and MPS method can be observed from the figure. However, the natural circulation is not fully developed in MPS results, which is similar conclusion as the tin experiment simulation. Figure 3-30 depict the temperature distribution at the 16min. The hot liquid is staying at the top of the cavity. Despite, The bulge of hot liquid gallium part can be observed in the FVM simulation[66], which is not exist in MPS method. It also due to the natural circulation in MPS simulation is not fully developed.

The simulation may be related to the particle size. Since the heat convection is calculated automatically by the moving particles, which assembly a huge number of molecule inside. Thus, the motive of these particles is weaker than the molecular thermodynamic movement, which results the weaker heat transfer. However, until now it is impossible to reduce the size of particles to even smaller because of the limitation of CFL condition, because the maximum velocity will increase when the diameter decrease.
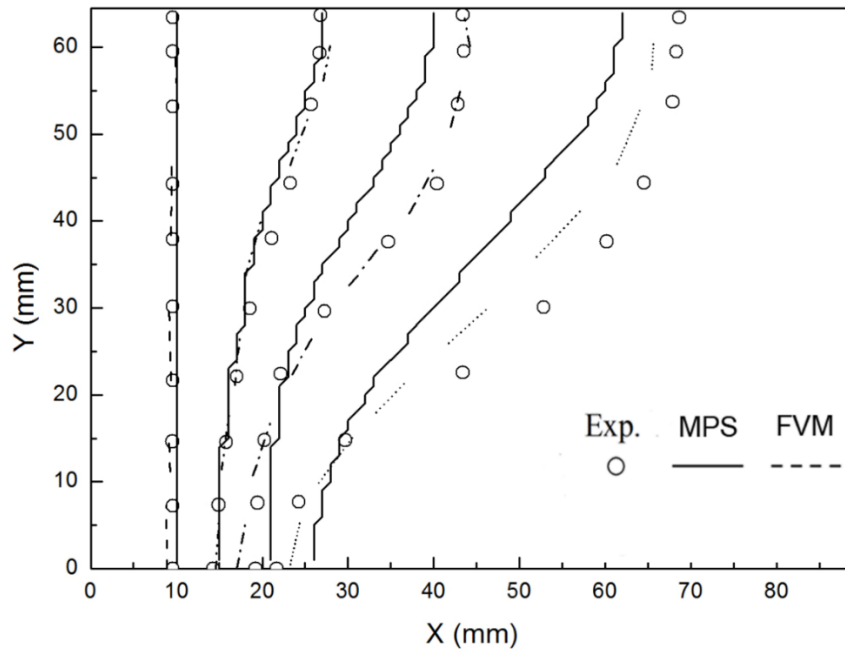
Figure 3-29. Melt behavior comparison between experiment, FVM[66] and MPS method.
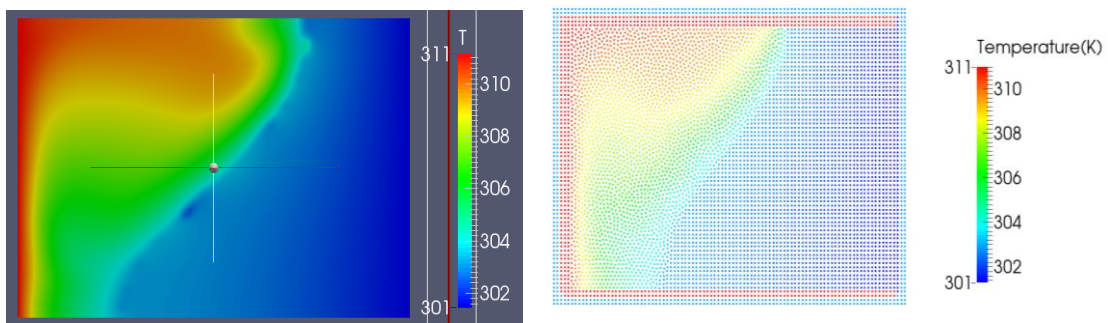
Figure 3-30. temperature distribution. Left: FVM method[66], Right: MPS method.

All in all, it can be concluded that MPS method can perfectly applied on low Rayleigh number or pure heat conduction conditions, but there is some Deviation on high Rayleigh number flow condition' simulation because of the limitation of particle size.
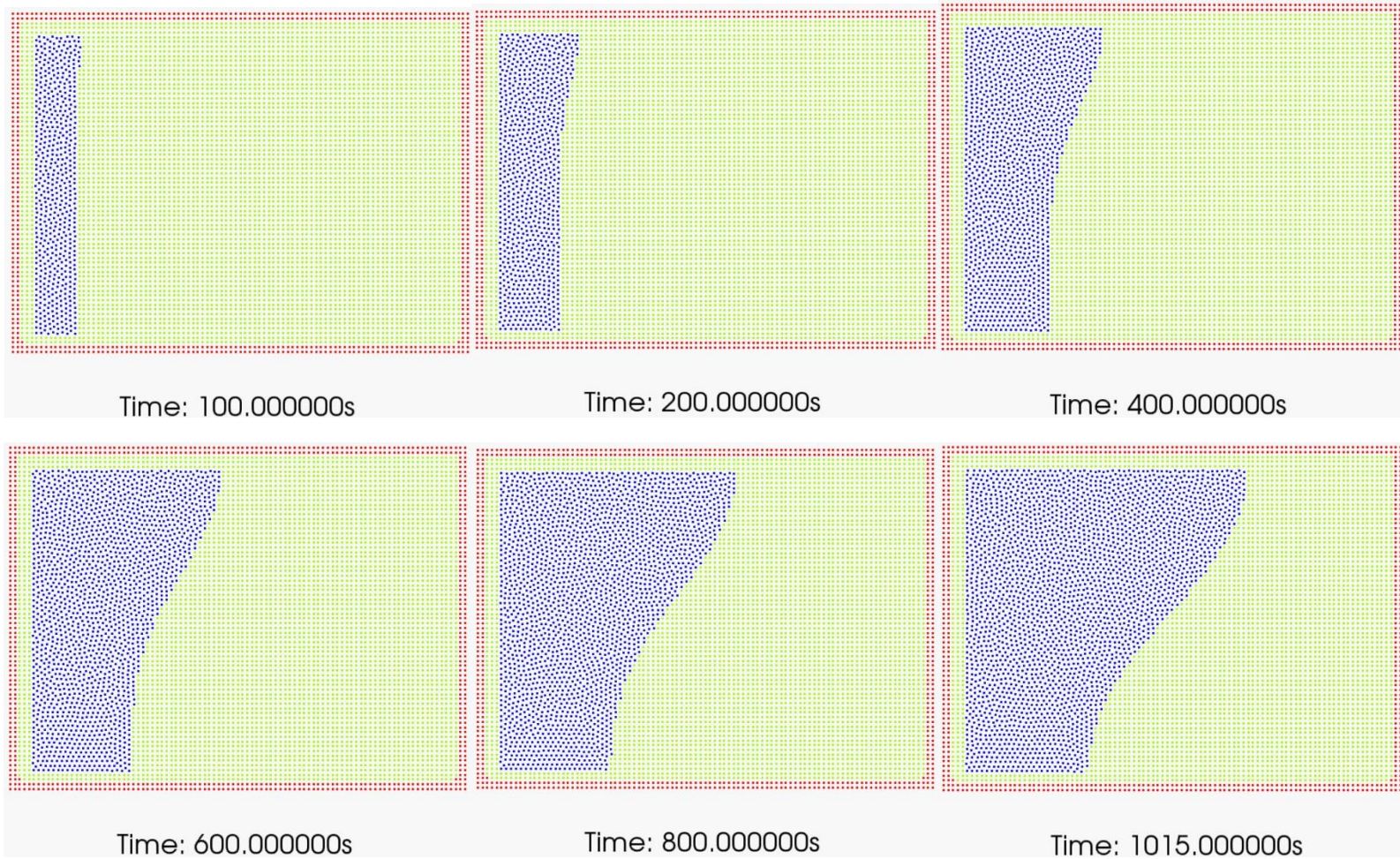
Figure 3-28. Melting progress from the results conducted by MPS method.

3.4. Conclusion of the chapter

1)   Single semi-infinity problem, double semi-infinity problem and Neumann problem was calculated by MPS method, and comparing the results with the analytical solution. The comparison shows the perfect match between two calculation results, which verified the availability of MPS method on such simulation.

2)   A small-scale experiment was conducted using u-alloy and gel wax to emulate the ablation behavior in MCCI. The motion of the u-alloy melt was visualized and temperature history measured as experimental data for code validation.

3)   The wax experiment was simulated using the developed MPS code, and compared with the experimental results. The ablation behavior, deformation profile of the molten metal, and temperature history matched the experimental results, which suggests that the MPS code is applicable to calculate the heat transfer and phase change of the molten metal pool.

4)   Tin and gallium experiments are simulated by the developed MPS code. Although the perfect data can be obtained from pure heat conductive and low Rayleigh number natural circulation simulation, there is some Deviation on high Rayleigh number flow condition' simulation because of the possible reason of the limitation of particle size.

4. Simulation of CCI-2 by multi-physics models

4.1. Outline of the work

Except heat transfer model, phase change model and natural circulation model, chemical reaction model, mixing model and gas generation model are developed in order to simulate the multi-physics phenomena in the MCCI process. In this chapter, CCI-2 experiment is simulated by these developed models. The effectivity of different models to the ablation behavior is discussed. Besides, the detail of ablation behavior can be obtained by the simulation results.

4.2. CCI-2 experiment

CCI series[67] tests were performed by Argonne National Laboratory aiming to achieve two technical objectives:

➤ Resolve the ex-vessel debris cool ability issue by providing both confirmatory evidence and test data for coolability mechanisms identified in previous integral effect tests.

➤ Address remaining uncertainties related to long-term 2-D core concrete interaction under both wet and dry cavity conditions.

Different concrete type are used among different tests, And totally different ablation behaviors were observed. Limestone concrete was applied in the CCI-2 experiment, which contribute a homogeneous deformation shape of the corium. The apparatus of the experiment are shown in Figure 4-1. The test section is 3.4m tall with a square internal cavity inside, which initially measured by 50cm x 50cm. This cavity is the place to fill with the corium and surround it is the limestone concrete which was intended to ablation. The concrete basemat was initially 55cm deep to keep a safe

range from assumed about 35cm axial ablation. The electrode sidewalls were fabricated from a castable MgO refractory, while another two non-electrode sidewalls were fabricated from the concrete. Type C thermocouple assemblies were cast with the MgO sidewalls. To generate the melt pool, two iron/alumina sparklers, wrapped with nichrome starter wire, were positioned a few centimeters below the top of the corium powder. The sparkler was used to initiate the thermite chemical reaction to produce the melt pool over a timescale of ~30 seconds. After the thermite reaction, DEH was supplied to emulate decay heat through two banks of tungsten electrodes which positioned at interior surface of the opposing MgO sidewalls. The water would injected at 300min to obtain the data with flooding. However, the flooding is not considered in this simulation due to the limitation of the simulation time.
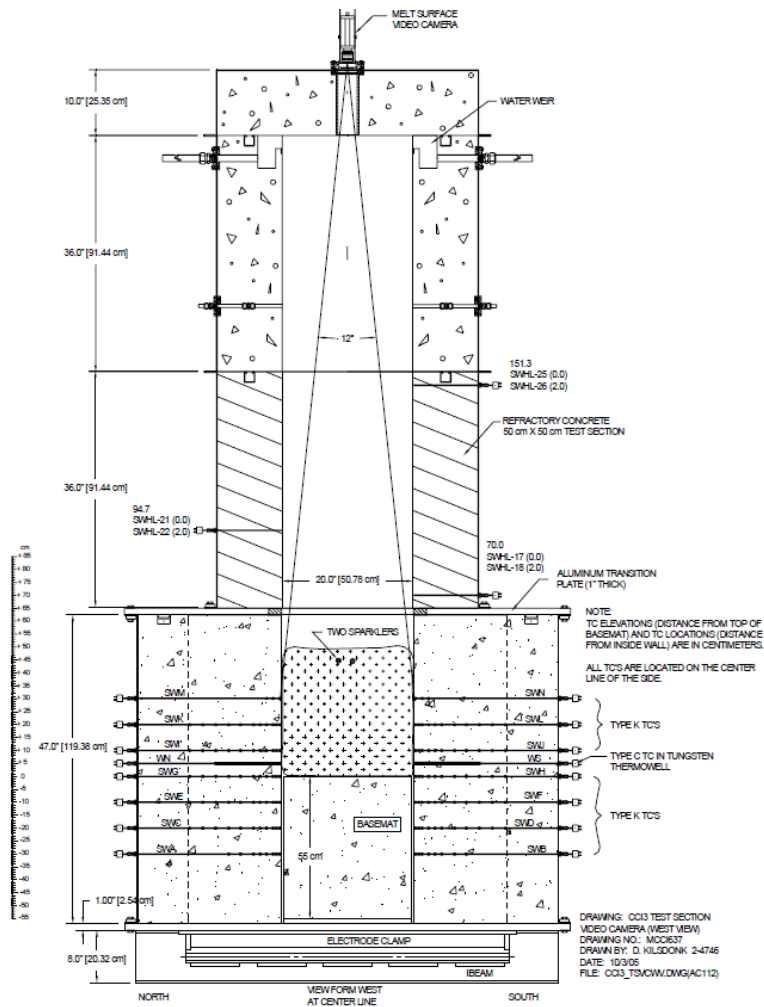
Figure 4-1. The apparatus of the CCI tests[67].

The concrete type is the key parameter among the CCI tests. As shown in Table 4-1, both CCI-1 and CCI-3 tests were performed with siliceous concrete, but with the different geographic origin. On the other hand, CCI-2 test was conducted with Limestone-Common Sand (LCS) concrete. Table 2-1 shows the chemical compositions of the three concrete types. This composition is determined by the chemical analysis of the samples taken from the concrete archives. The exothermal release from the chemical reaction and the mass of the generation gas would be calculated by this chemical composition. Thus, this data is extreme important for the simulation in this chapter.

The density of the concrete used in the tests are shown in Table 4-2, which are calculated by the measured mass and volumes of the archive samples for each test. The initial corium composition for CCI tests were fully oxidized PWR core melt with various proportions of concrete. The composition of the concrete additives were consistent with the concrete used in the sidewalls and basemat.

The initial corium composition after the thermite reaction is shown in Table 4-3. We can see from the table that Cr is the only metallic which is going to interact with the concrete decomposition gases (CO_2 and H_2O). The thermal properties of the corium is calculated by the each constitute and their mass fractions.

The event sequence of CCI-2 experiment is shown in Table 4-4. The tests began from the corium melt made initial contact with the basemat surface at Time t=0 (at completion of the thermite reaction). After that, DEH was ramped up to 120 kW as design, which is essentially maintained for the balance of the test involving dry cavity operations.

Table 4-1. Chemical composition of concretes

Oxide	CCI-1 (Wt%)	CCI-2 (Wt%)	CCI-3 (Wt%)
Al_2O_3	0.77	2.49	3.53
CaO	8.54	25.88	16.79
Fe_2O_3	0.79	1.39	1.49
MgO	0.60	11.47	0.85
MnO	0.00	0.03	0.04
K_2O	0.12	0.55	0.81
SiO_2	82.48	21.61	59.91
Na_2O	0.00	0.31	0.66
SrO	0.00	0.00	0.04
TiO_2	0.051	0.135	0.155
SO_3	0.514	0.505	0.434
CO_2	0.901	29.71	9.8
$H_2O, Free$	1.808	3.255	2.293
$H_2O, Bound$	1.92	1.11	1.40
Total	98.48	98.47	98.19

Table 4-2. Density of concretes

Tests	CCI-1	CCI-2	CCI-3
Concrete density (kg/m^3)	2300	2330	2270

Table 4-3. Initial Melt Compositions for CCI Test Series.

Constitute	CCI-1 ($Wt\%$)	CCI-2 ($Wt\%$)	CCI-3 ($Wt\%$)
UO_2	60.97	60.62	56.32
ZrO_2	25.04	24.90	23.13
Calcined concrete	8.08	8.07	14.14
Cr	5.19	6.41	6.41

The ablation started at both axial and radial direction from the first minute of the interaction. The evidence of the Aerosol release can be obtained from the first few minutes. The corium temperature behavior at the beginning is decrease to 1800 ^oC first and then gradually raise up to 1910 ℃. Eruption was observed because of the breach of the crust. The time scale is about 35 min and 50 min for north sidewall and basemat, respectively. The cavity was flooded on 300 min and gradually cooled down after that. More detail information could be found from the experiment report[67].

Due to the objective of code's validation, the simulation is focusing on the dry cavity condition at the first two hours to discuss the ablation behavior and the phenomena in the MCCI process. A lot of the parameters is going to compare between the experiment and simulation, which include the ablation rate of both axial and radial direction, the temperature of the corium, the role played by the chemical reaction and the gas generation to the ablation behavior. The simulation configuration will be explained in the next part.

Table 4-4. Major event sequence of CCI-2 test[67]

Time (Minutes)	Event
-0.6	Thermite burn initiated.
0.0	Melt generation completed; initial temperature ~1880°C.
0.4	Onset of basemat ablation detected at all thermocouple locations, and at some part on both the North and South sidewalls.
1.2	Aerosol clears in test section plenum revealing crusted melt upper surface.
1.6	Target input power of 120kW reached.
34.9-38.4	Average melt temperature peaks at the start of the period, and then steadily declines to ~1800°C at the end of the period.
42.7-43.6	Melt eruption near North sidewall; aerosols gradually block view. Ablation burst detected at + 10cm elevation on North sidewall. Local ablation depth proceeds from 2.5 to 7.6 cm; average ablation rate =1.6 cm/min.
42.2-52.8	Axial ablation picks up dramatically, proceeding from 2.5 to 7.6 cm; average ablation rate =0.5cm/min.
62.7-85.7	Intermittent eruptions through holes in crust near Northeast corner.
146.8-155.0	Eruptions through holes in crust in Southwest corner.
300.8	Water addition initiated on the basis of reaching the 29.2 cm depth in North sidewall; melt temperature ~1540 °C. Cooling rate reaches 2.8 MW/m^2.
325.8-332.2	Intermittent eruptions observed below the bridge crust, as evidenced by luminescence through crust opening in the Southeast corner.
346.0	Crust lance used in an attempt to breach the bridge crust. Peak load of 3.35 kN applied. Crust was not breached.
423.1	Test terminated on the basis that concrete temperatures had stabilized. Power supply operations and data acquisition terminated.

4.3. Simulation configuration

4.3.1. Geometry and initial setup

As shown in Figure 4-2, a two-dimensional domain was established to simulate the CCI-2 experiment. Since the simulation would not calculated till the end of the experiment, the size of the concrete wall is cut to save the calculation time. However, the size of the melt pool keeps consistent with the experiment cavity. The height of the corium is equal to the height after thermite reaction in the experiment, not that of the powder before burning. There are three types of particles, represented by blue, green, and red, which are corium particles, concrete particles, and virtual particles, respectively. The initial setting of the simulation is shown in Table 4-5.
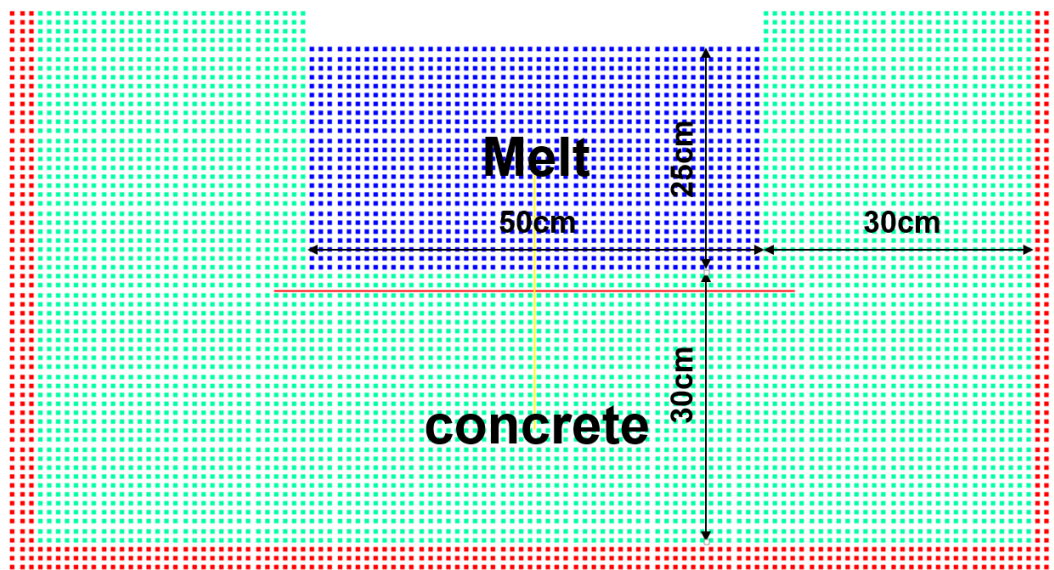
Figure 4-2. Geometry of the simulation.

Table 4-5. Initial condition of the simulation

Parameter	Value
Initial temperature of concrete (*K*)	293.0
Initial temperature of corium (*K*)	2153.0
Average distance between particles (*m*)	0.01
Total number of particles	6692

4.3.2.Material thermal properties

The material thermal properties utilized in the simulation will be introduced in the following text. As to the concrete, the density is shown in Table 4-2 and it supposed to be a constant during through the whole process. The thermal conductivity of different types of concrete are shown in Figure 4-3[68]. Since limestone is utilized in the CCI-2 experiment, the concrete thermal conductivity is decrease linearly from 2.0 $W \cdot m^{-1} \cdot K^{-1}$ at $20^{o}C$ to 1.2 $W \cdot m^{-1} \cdot K^{-1}$ at $800^{o}C$, and then keep 1.2 $W \cdot m^{-1} \cdot K^{-1}$ as a constant in the simulation. The specific heat of concrete is depict in Figure 4-4[68], which increase from 800 $J \cdot kg^{-1} \cdot K^{-1}$ at 20ºC to 1200 $J \cdot kg^{-1} \cdot K^{-1}$ at 700ºC in the simulation. After 700ºC, the value will keep steady on 1200 $J \cdot kg^{-1} \cdot K^{-1}$. The melting point of the concrete is 1295 ^{o}C. Once the temperature exceed this value, the concrete particle would switch its particle type from solid to liquid. If this liquid concrete particle touch any corium particle, the particle material will change from concrete to corium.
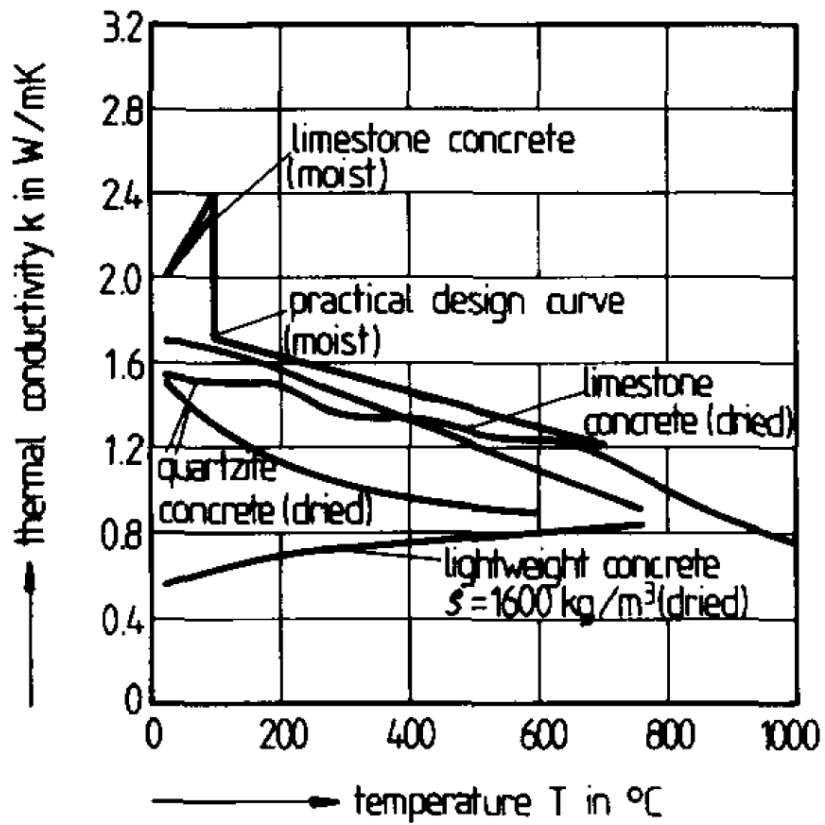
Figure 4-3. Thermal conductivity of different types of concretes[68].
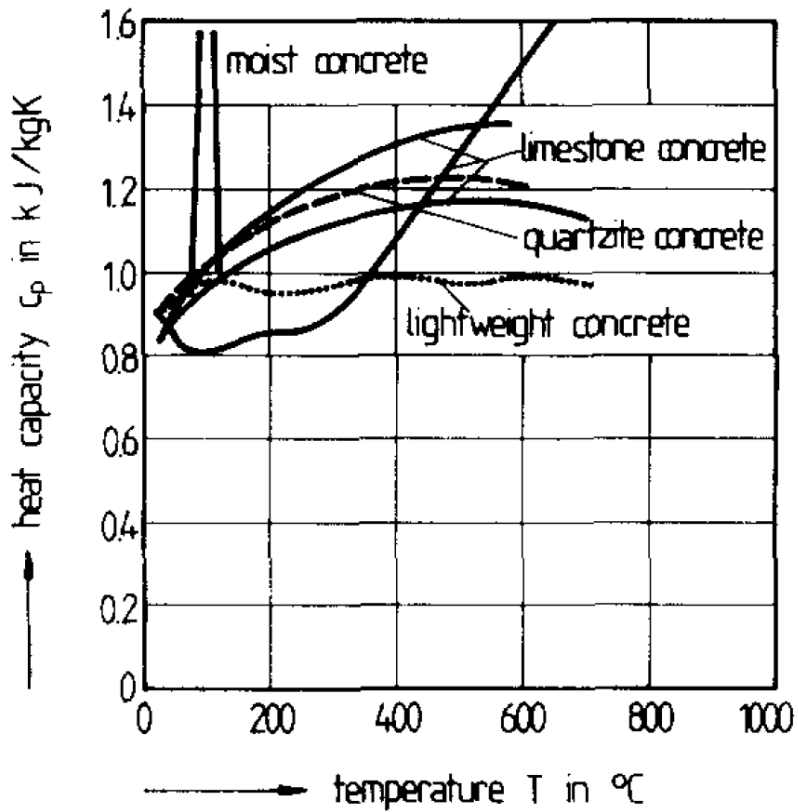
Figure 4-4. Specific heat of different types of concrete[68].

As to the mixture, the thermal properties will be calculated as weight averages of the individual components.

$$C = 1 / (W_i / C_i + W_j / C_j + W_k / C_k + ...) \tag{5-1}$$

where C is the thermal properties, such as specific heat, density and thermal conductivity. W is the mass fraction. Subscript i, j, k represent each component in the mixture, such as UO_2, ZrO_2, Cr and concrete. The properties of concrete inside the mixture is kept consistent as that of the pure concrete discussed before.

According to Asmolov et al. [69], The density of UO_2 and ZrO_2 near its melting point is 8860 kg/m^3 and 5150 kg/m^3, respectively. The density of liquid Chromium is 6300 kg/m^3.

According to International Nuclear Safety Center[70, 71], the specific heat of UO_2 can be calculated by the equation

$$C_p = 1 9 3 . 2 1\!\!+\!\!7 \quad 3 2 5 . 7 1 \quad 3 1 1 . 9 6 9 7 t^2 \quad 1 6 . 8 1^4 1 - 9 . 7 t \tag{5-2}$$

where $\tau = T / 1000$, T is the temperature of the UO_2. The heat capacity of ZrO_2 is obtained from the MELCOR's manual[72], where a constant specific heat of 544.3 $J \cdot kg^{-1} \cdot K^{-1}$ is suggested. The specific heat of liquid Chromium is 972.62 $J \cdot kg^{-1} \cdot K^{-1}$.

Thermal conductivity of UO_2 is in the range of 2.5 to 3.6 $W \cdot m^{-1} \cdot K^{-1}$ based on the report of International Nuclear Safety Center[70]. According to MELCOR's manual[72], the thermal conductivity of ZrO_2 is 2.49 $W \cdot m^{-1} \cdot K^{-1}$ when the temperature is higher than 1727 ºC. The thermal conductivity of Chromium is 93.9 $W \cdot m^{-1} \cdot K^{-1}$.

The viscosity of the corium is hard to decide since it is in the "mushy" domain between solidus and liquidus temperature. The value used in the simulation is from the research of Epstein[73], where recommends a constant viscosity of $0.3 \pm 0.2 \, kg/m \cdot s$ for limestone/common-sand concrete. It will keep constant even melt concrete mix into the corium.

4.4. Results discussion

The CCI-2 simulation results calculated by the developed code will be discussed in this section. Multi-physics models were applied in order to simulate the phenomena during the process. Four simulations with same geometry and initial input data but different model combinations were performed to observe the role played to the simulation by each models. The models combinations are shown in Table 4-5.

Case1 didn't considered the composition dependence corium melting temperature, as well as other multi-physics models, thus it is meaningless to compare only Case1 results with experimental results since it was too simplified and far away from the reality. Therefore in this section, Case2, Case3, Case4 will be compared with experimental results one by one. Results discussion by comparing the different cases will be stated in the last section

Table 4-5. Summarize of the CCI-2 simulation.

Models	Case1	Case2	Case3	Case4
Heat transfer	O	O	O	O
Phase change	O	O	O	O
Natural circulation	O	O	O	O
Surface tension	O	O	O	O
Infinity diffusion	O	O	-	-
Chemical reaction	-	-	-	O
Gas generation	-	-	-	O
Mass diffusion	-	-	O	O
Active corium solidus temperature	-	O	O	O

4.4.1. Case2 (with composition dependence solidus temperature)

Compare to case1, the simulation in this case considered the variation of the mixture's solidus temperature with the increasing concrete mass fraction. As shown in Figure 1-2, the solidus temperature of the mixture decreases rapidly when the concrete mass fraction increases, and it is almost the same as the melting point of the pure concrete once the concrete mass fraction reach to about 20%. That is to say, with the process proceeding, the corium's solidification is harder and harder and the crust would be vanished at the end of the process.

The melting point of the mixture used in the simulation are calculated by

$$
\begin{cases}
T_{melt} = 2500.0 - 9.0 \times W_{concrete} \times 100 & W_{concrete} < 0.1 \\
T_{melt} = 2225.0 - 6.25 \times W_{concrete} \times 100 & 0.1 \leq W_{concrete} \leq 0.14 \\
T_{melt} = 1546.0 - 1.4 \times W_{concrete} \times 100 & 0.14 < W_{concrete} < 0.2 \\
T_{melt} = 1266.0 & W_{concrete} \geq 0.2
\end{cases}
\qquad (5\text{-}3)
$$

The ablation process of Case2 are shown in the series pictures in Figure 4-5. Corium, solid concrete, crust, liquid concrete are represented by blue, light green, yellow, red particles, respectively. We can see from the figure that the crust formed at the corium/concrete interface from the very beginning since the corium was cooled down by the cold concrete. These crust would heat up the concrete and gradually trigger the partial concrete decomposition. The crust at the bottom is thicker than that at the sidewall since the temperature in the top is higher due to the natural circulation of the melt pool (the maximum thickness is 4cm at the bottom and 3cm at the sidewall). First liquid concrete appears at around 22min. The corium was keep heating up by the inner source heat, which gradually re-melt the crust. At around 30min, the crust break and liquid concrete mixed into the corium (particle material switch from

concrete to corium). The material properties of the whole corium pool were re-calculated based on Mixing model 1. Therefore, the liquid concrete particles directly become crust since their temperature is lower than the melting point of the corium. The ablation is proceeding with the cycle of crust generate--re-melt--regenerate--re-melt--…. The solidus temperature of the corium decreases with concrete mass fraction increases. Thus, the crust generation become harder and harder with progress proceeding, so that the convection heat transfer is enhanced due to the fewer crust.

Figure 4-6 shows the temperature distribution along the elapsed time. We can see from the pictures that the hot particles are staying at the top of the pool due to the natural convection, which cause the quicker ablation rate to the sidewalls. The temperature diffusion of the concrete is not so high due to its low thermal conductivity.

Figure 4-7 shows the ablation front head in the concrete along the elapsed time. It shows pronounced sidewall ablation in the simulation. The ablation is almost linearly increase, and the speed is about 4cm/h for sidewall and 2cm/h for basemat, respectively.

Figure 4-8 shows the average temperature of the melt pool. The melt is cooled down by the cold concrete to 1843°C at the first 6 minutes, then gradually heated up by the inner source heat to about 1850°C. There are several small decrease when the liquid concrete mix into the corium.
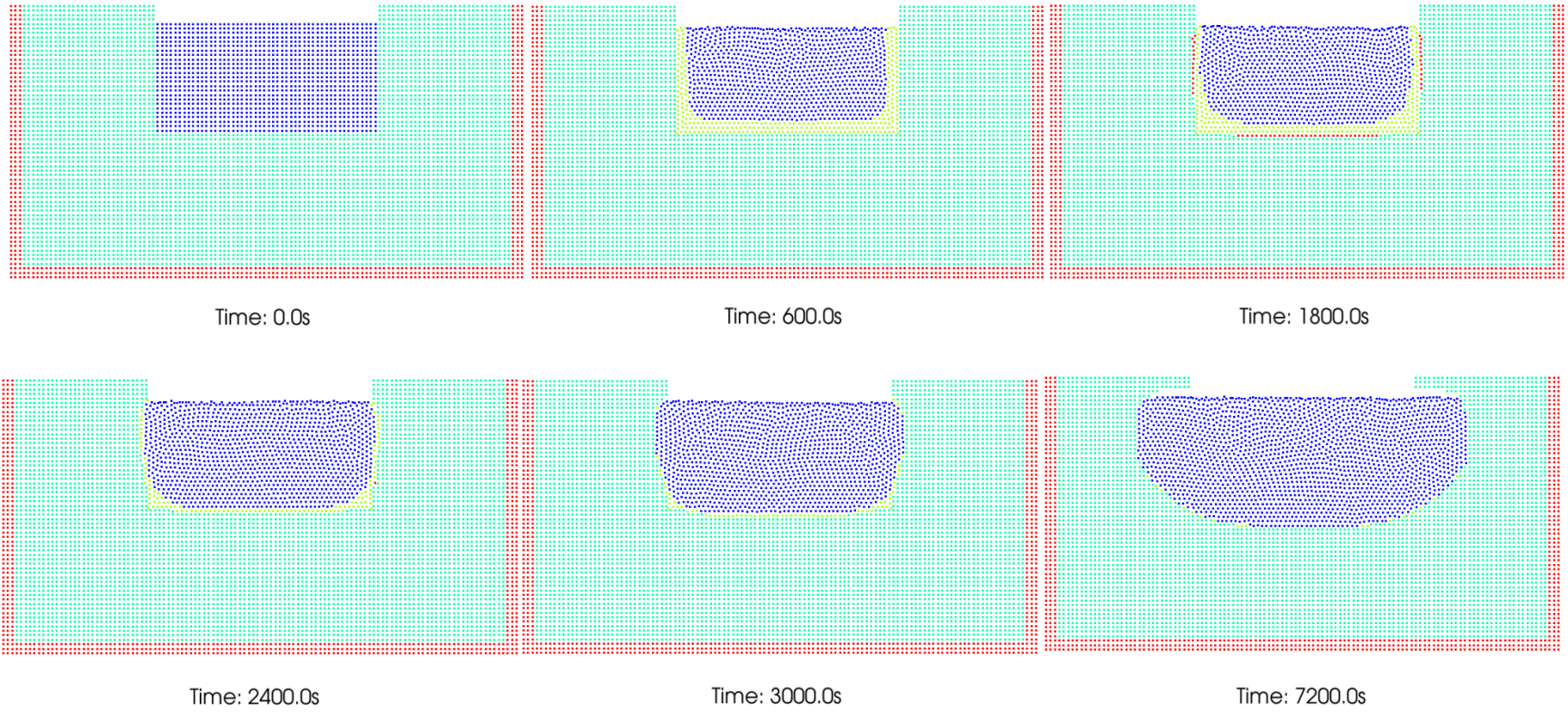
Figure 4-5. Ablation progress along the eplapse time (Top: 0, 20, 30min; Bottom: 40, 50 120min).

.
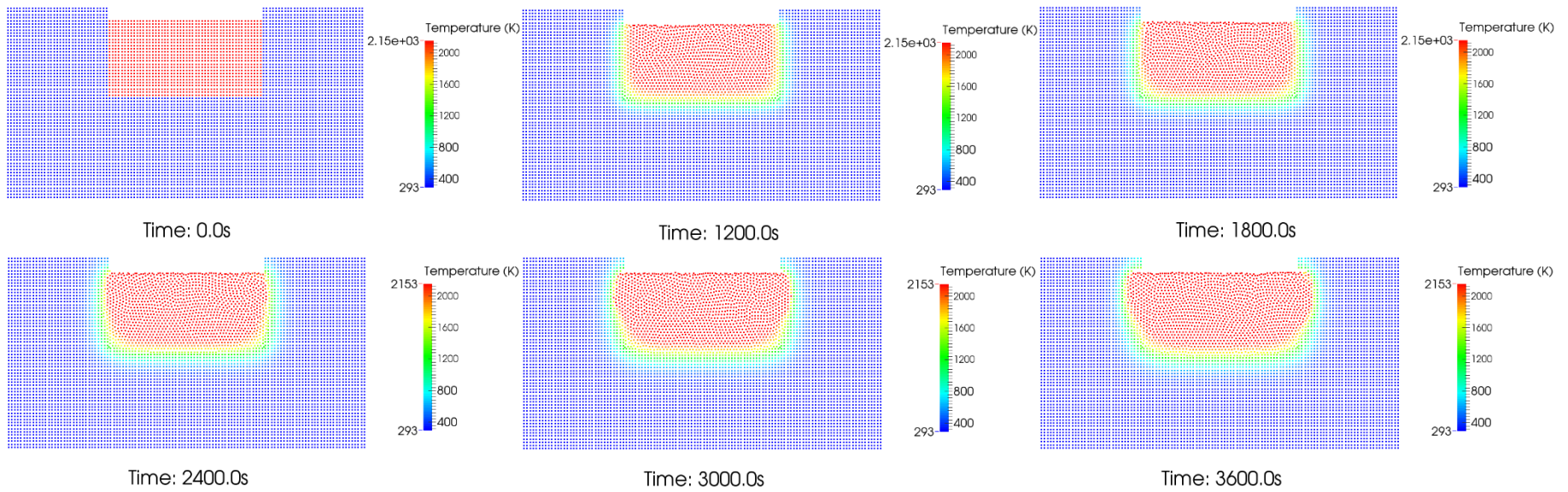
Figure 4-6. Temperature distribution along the elapse time (Top: 0, 20, 30min; Bottom: 40, 50, 60min)
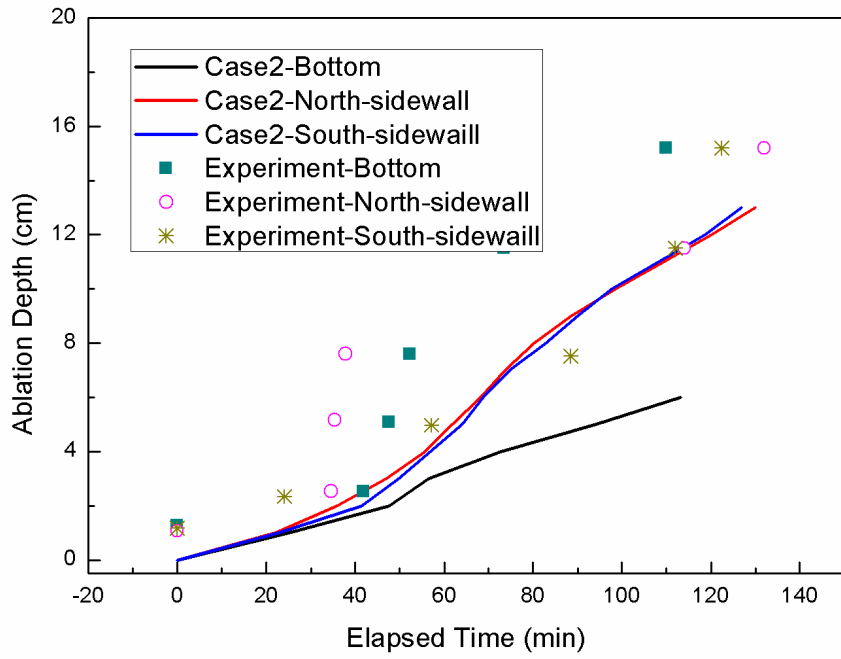
Figure 4-7. Ablation rate along the elapsed time.
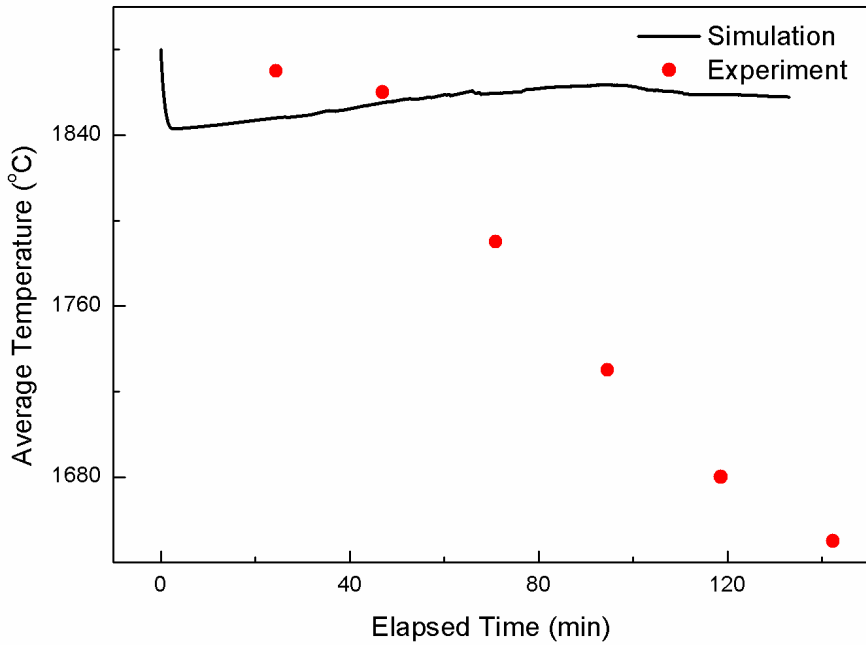
Figure 4-8. Average temperature along the elapse time.

4.4.2.Case3 (with mass diffusion model)

The mass diffusion process is considered in this simulation. Compare to the infinity mixing process, this simulation is more reliable and physical.

The situation before the crust breach keeps consistent as Case2. Once the concrete contact the corium after the crust break, the code would call the mixing model 2 to calculate the mixing process. As explained in Chapter 2, it supposed to have two barrels in each particles, with corium and concrete inside, respectively. Once the liquid concrete particle contact the corium particle, the mass of the materials in both barrels would transport with each other based on the diffusion equation.

Since both of the density and heat capacity of the particle would be changed after the diffusion calculation, the enthalpy of this particle will be reset by the new density and heat capacity. Otherwise, the temperature would be oscillate.

Figure 4-9 shows the ablation progress of the simulation. Like Case2, the crust is generated from the very beginning of the process due to the cold concrete. And the crust is re-melt by the inner source heat and breach at around 30 minutes. Unlike the previous simulation, the liquid concrete mixed into the corium by calculating the diffusion equation. Thus, the liquid concrete will not directly become crust since the sudden change of the material properties does not exist. The hot corium will invade the domain of liquid concrete when the crevasse is big enough, and results in a rapid erosion.

Figure 4-10 shows the temperature distribution along the progress. Similar as Case2, before the crust breach, the hot corium particles are staying at the top of the melt pool due to the natural convection. However, after the crust break, the cold light concrete particles, which have not fully mixed into the corium, are staying at the top. Besides, the hot corium particles in the breach hole are cool down by the cold concrete. The hottest corium is lay on the middle of the melt pool.

Time: 0.0s   Time: 600.0s   Time: 1800.0s

Time: 2400.0s   Time: 3000.0s   Time: 7200.0s
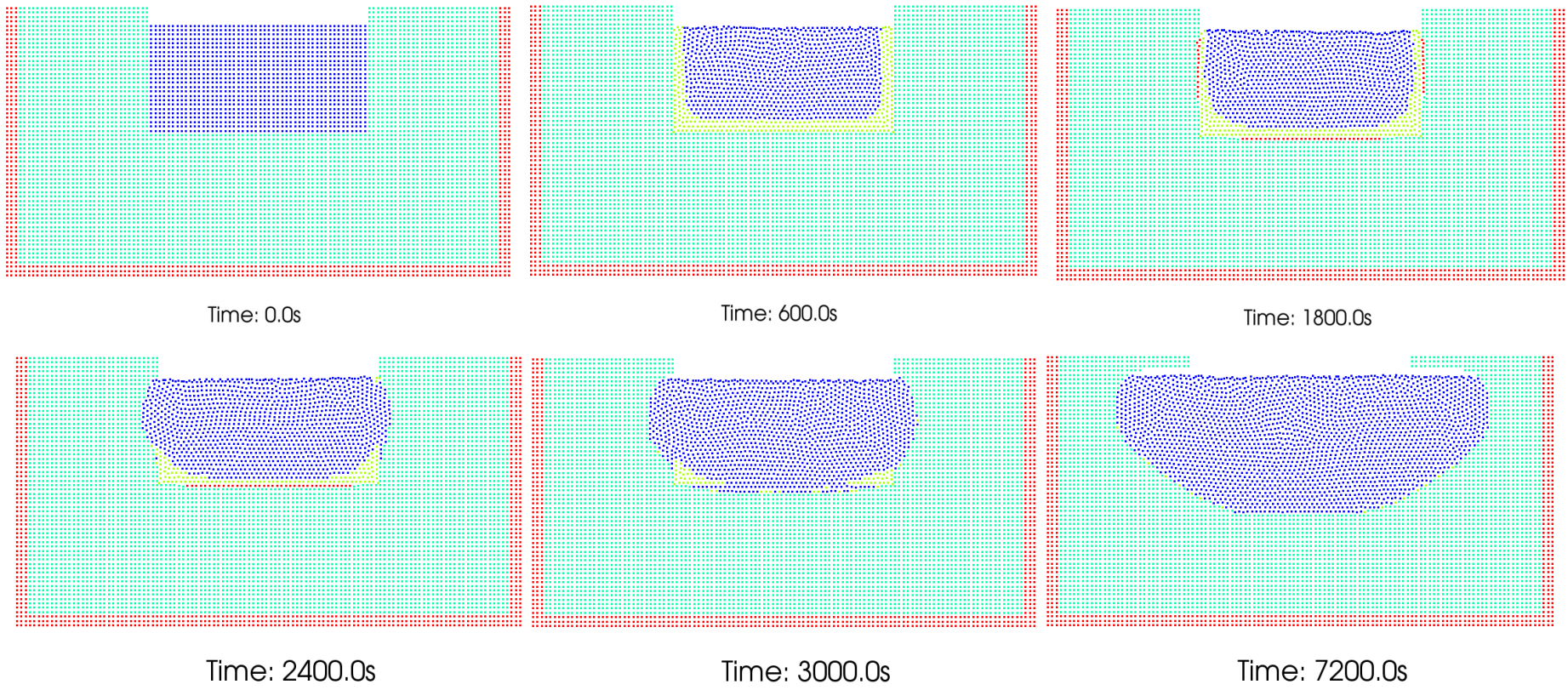
Figure 4-9. Ablation progress along the elapse time (Top: 0, 30, 40 minutes; Bottom: 50, 60, 120 minutes).
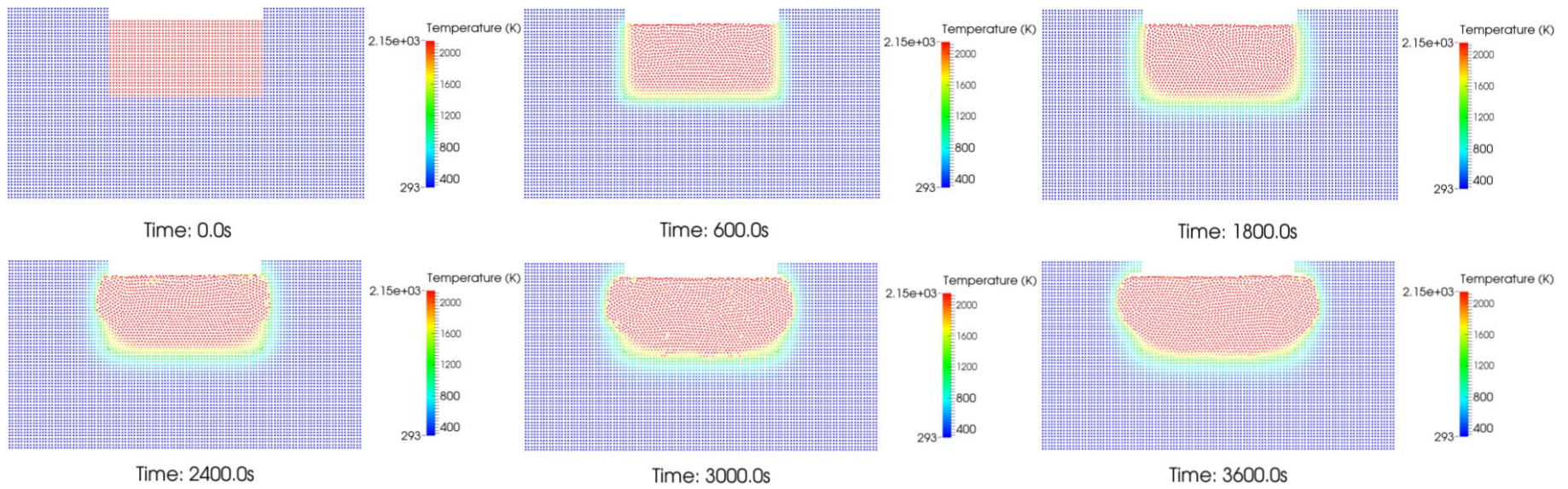
Figure 4-10. Temperature distribution along the elapse time (Top: 0, 20, 30min; Bottom: 40, 50 60min)
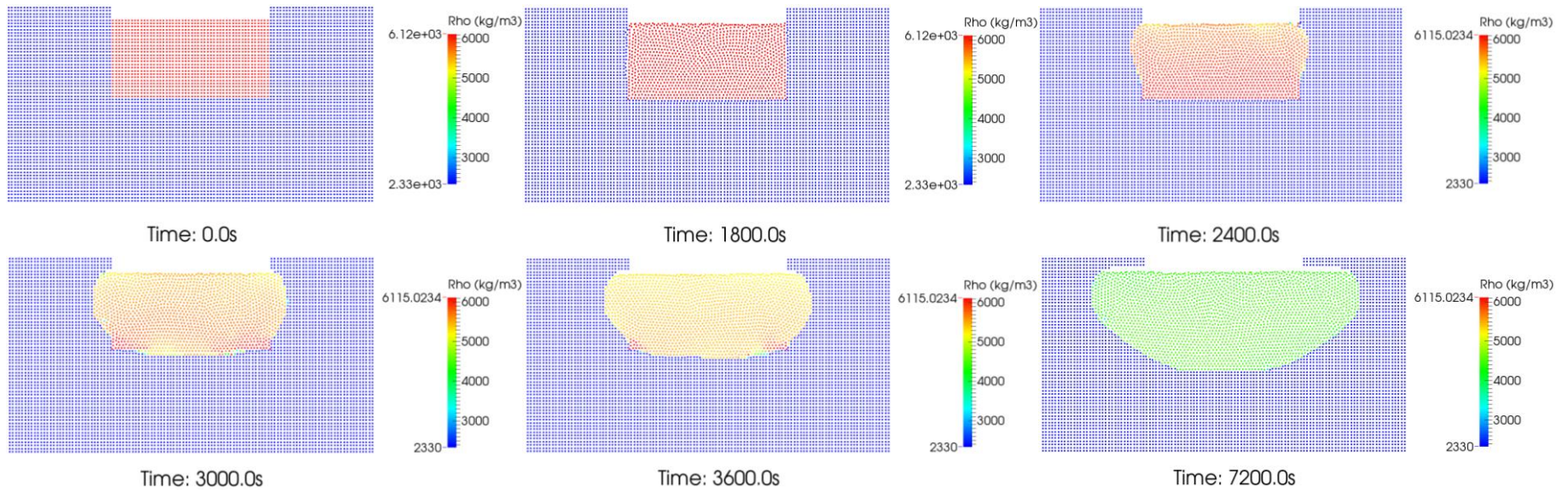
Figure 4-11. The corium mass fraction after the crust breach (Top: 0, 30, 40 minutes; Bottom: 50, 60, 120 minutes).
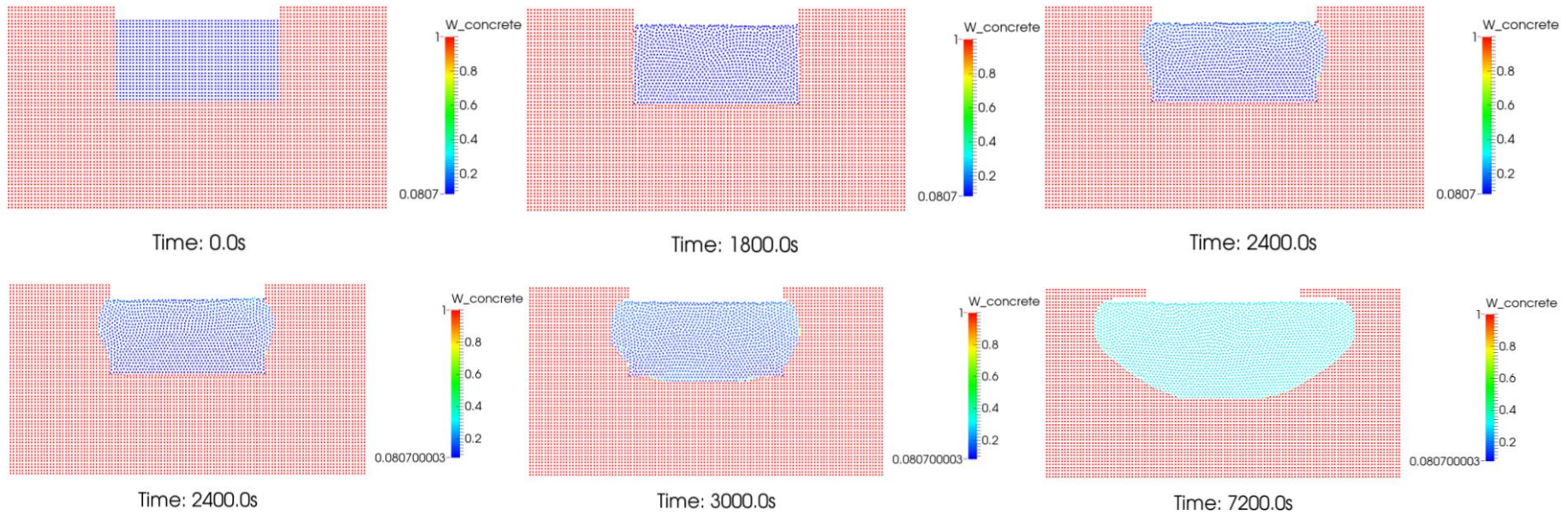
Figure 4-12. The concrete mass fraction along the elapsed time (Top: 0, 30, 40 minutes; Bottom: 50, 60, 120 minutes).

A series of pictures of Figure 4-11 shows the density changes along the ablation process. We can see from the pictures that the density of the melt pool gradually decrease from 6120kg/m^3 at the beginning to less than 4000kg/m^3 at 180min due to the mixing of the light concrete. Diffusion process can be clearly visualized from the pictures. Melt pool is very non-uniform right after the crust breach due to the big density difference between the corium pool and concrete. The concrete particles gradually diffused to the other corium domain and changed the material properties of the particles. This diffusion process become weaker after several hours, since the density difference between the concrete and the corium pool decreased. Lighter particles lay on the top of the melt pool due to the natural convection. Once the crust near the bottom collapse, a big solutal convection (light concrete particles rise up to the top) can be observed. Similar tendency can be observed in the pictures of Figure 4-12, where the concrete mass fraction is showing.

The ablation rate is shown in Figure 4-13. Similar as Case2, it shows very slow ablation speed before the crust break. However, a rapid increase of the erosion can be observed since the hot corium replaced the liquid concrete after the crust breach.

The average temperature of the melt pool is shown in Figure 4-14. Similar as previous cases, the temperature is at first decrease since the corium is cooled down by the cold concrete, then steady grow up to about 1850°C. Rapid decrease after 33 minutes can be observed which is due to the pronounced heat transfer between the corium and concrete after the crust breach.
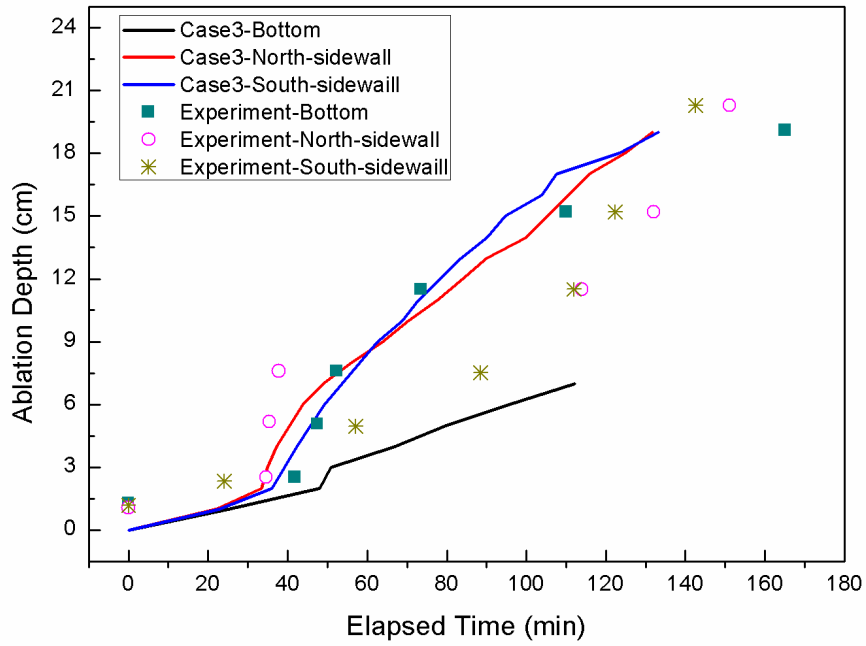
Figure 4-13. Ablation rate along the elapse time.
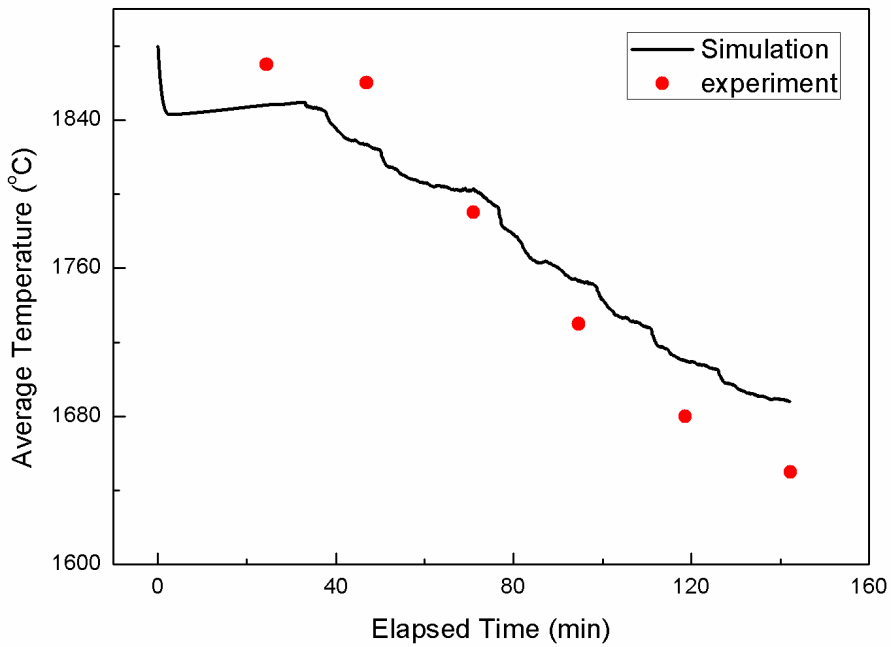
Figure 4-14. The average temperature of the melt pool.

4.4.3. Case4 (with chemical reaction and gas generation)

Compare to case3, chemical reaction and gas generation is considered in this case. Addictive thermal is provided by the redox chemical reaction. The generated gas bubbles would rise up in the melt pool and stirring the mixture. Quantitative calculation of these two models is depend to the different corium and concrete composition. In the following text, the approach to calculate the heat release from the chemical reaction and the mass of the decomposed gas for CCI-2 experiment will be introduced.

➢ **Chemical reaction and gas generation calculation**

Due to the corium composition, the redox reactions that take place in the melt pool are

$$2Cr + 3H_2O \rightarrow Cr_2O_3 + 3H_2 + 3.6MJ / kg_{Cr}$$
$$2Cr + 3CO_2 \rightarrow Cr_2O_3 + 3CO + 2.8MJ / kg_{Cr}$$

(5-4)
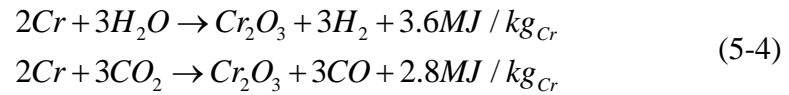
The amount of the Cr, H_2O and CO_2 is required to calculate the accurate mass of generated gas and the thermal released from the redox reaction. Based on the volume of the melt pool and the mass fraction of the chromium, the amount of chromium could be calculated by

$$N_{Cr} = \frac{m_{Cr}}{M_{Cr}} = \frac{V_{corium} \times \rho_{corium} \times W_{Cr}}{M_{Cr}} = 26.14$$

(5-5)

where $N_{Cr}, m_{Cr}, M_{Cr}, W_{Cr}$ are the chromium's amount, mass, molar mass and mass fraction in corium, respectively. And V_{corium} and ρ_{corium} is the volume and the density of the corium. W_{Cr} can be found in Table 4-3.

On the other hands, the total amount of H_2O and CO_2 in concrete can be calculated by the composition of concrete.

$$N_{H_2O} = \frac{m_{H_2O}}{M_{H_2O}} = \frac{V_{concrete} \times \rho_{concrete} \times W_{H_2O}}{M_{H_2O}} = 1.71 \qquad (5\text{-}6)$$

$$N_{CO_2} = \frac{m_{CO_2}}{M_{CO_2}} = \frac{V_{concrete} \times \rho_{concrete} \times W_{CO_2}}{M_{CO_2}} = 4.76 \qquad (5\text{-}7)$$

where N_{H_2O}, m_{H_2O}, M_{H_2O}, W_{H_2O} are water's amount, mass, molar mass and mass fraction in the concrete, respectively. N_{CO_2}, m_{CO_2}, M_{CO_2}, W_{CO_2} are the carbon dioxide's amount, mass, molar mass and mass fraction in the concrete, respectively. $V_{concrete}$ and $\rho_{concrete}$ is the volume and the density of the concrete (both sidewall and basemat). W_{H_2O} and W_{CO_2} can be found in Table 4-1.

Relate it with the chemical reaction (5-4), we can conclude that in the CCI-2 experiment, the chromium have more amount than the actual demand for the redox reaction in the melt pool, which means both chemical heat release and the amount of gas generation should be calculated by the amount of water and carbon dioxide.

In the simulation, once a concrete particle i touch the corium particle, the chemical reaction would be happen, and new gas particles would be generated. The mass of the new gas particle can be calculated by the equations

$$m_{H_2} = N_{H_2}M_{H_2} = N_{H_2O}M_{H_2} = \frac{m_{H_2O}}{M_{H_2O}}M_{H_2} = \frac{V_i \times \rho_{concrete} \times W_{H_2O}}{M_{H_2O}}M_{H_2} = 0.7125g \;(5\text{-}8)$$

$$m_{CO} = N_{CO}M_{CO} = N_{CO_2}M_{CO} = \frac{m_{CO_2}}{M_{CO_2}}M_{CO} = \frac{V_i \times \rho_{concrete} \times W_{CO_2}}{M_{CO_2}}M_{CO} = 27.77g \;(5\text{-}9)$$

where m_{H_2}, M_{H_2} are the mass and molar mass of the hydrogen; m_{CO}, M_{CO} are the mass and molar mass of the carbon monoxide; V_i is the volume of particle i. As explained in Chapter 2, two new gas particles will be generated once the chemical reaction take place. In this simulation, the mass of the new generated gases particle

are m_{H_2} and m_{CO}.

The process of chemical heat release in this simulation is assumed as 10 seconds long. According to the chemical reaction equation (5-4), the heat release could be calculated by the following equations

$$q_{H_2} = \frac{m_{Cr} \times 3.6 \times 10^6}{t_{chemical}} = \frac{N_{Cr} \times M_{Cr} \times 3.6 \times 10^6}{t_{chemical}}$$
$$= \frac{2}{3} \times \frac{N_{H_2O} \times M_{Cr} \times 3.6 \times 10^6}{t_{chemical}} = 2050W \tag{5-10}$$

$$q_{CO} = \frac{m_{Cr} \times 2.8 \times 10^6}{t_{chemical}} = \frac{N_{Cr} \times M_{Cr} \times 2.8 \times 10^6}{t_{chemical}}$$
$$= \frac{2}{3} \times \frac{N_{CO_2} \times M_{Cr} \times 3.6 \times 10^6}{t_{chemical}} = 5712.69W \tag{5-11}$$

where q_{H_2} and q_{CO} are the chemical heat release from two chemical reactions, respectively. $t_{chemical}$ is the duration of the chemical reaction, which assumed as 10 seconds in this simulation. The chemical heat release would spread through the whole melt pool domain.

Figure 4-15 shows the ablation process in Case4 simulation. Generally, it doesn't shows big differ from Case3 but a little bit quicker due to the heat released from the redox chemical reaction. The crust is generated and re-melt like Case2. After the crust breach, the hot corium replaced the cold liquid concrete and make a rapid erosion, which is similar as Case3. The liquid concrete mix into the corium by calculating the diffusion equation.

The temperature distribution is shown in the pictures of Figure 4-16. Similar as previous cases, the hot corium particles stay at the top of the melt pool due to the natural convection. After the crust breach, the cold liquid concrete penetrated into the melt pool and lay on the top.

The corium density variation can be seen from the pictures in Figure 4-17.

Similar corium distribution as Case3 can be observed from the pictures. However, it shows well stirred than that in Case3 due to the enhancement by the moving bubbles. Relatively, the concrete mass fraction can be seen from the pictures in Figure 4-18. Similar tendency is obtained as the corium density.

The ablation rate is shown in Figure 4-19. Similar as Case2, it shows hyper slow erosion before the crust break. However, there is a rapid increase of the erosion since the hot corium replaced the liquid concrete after the crust breach. Besides, the heat release from the chemical reaction also support the erosion.

The average temperature of the melt pool is shown in Figure 4-20. Like Case3, a rapid decrease after 30 minutes can be observed which is due to the pronounced heat transfer after the crust breach.
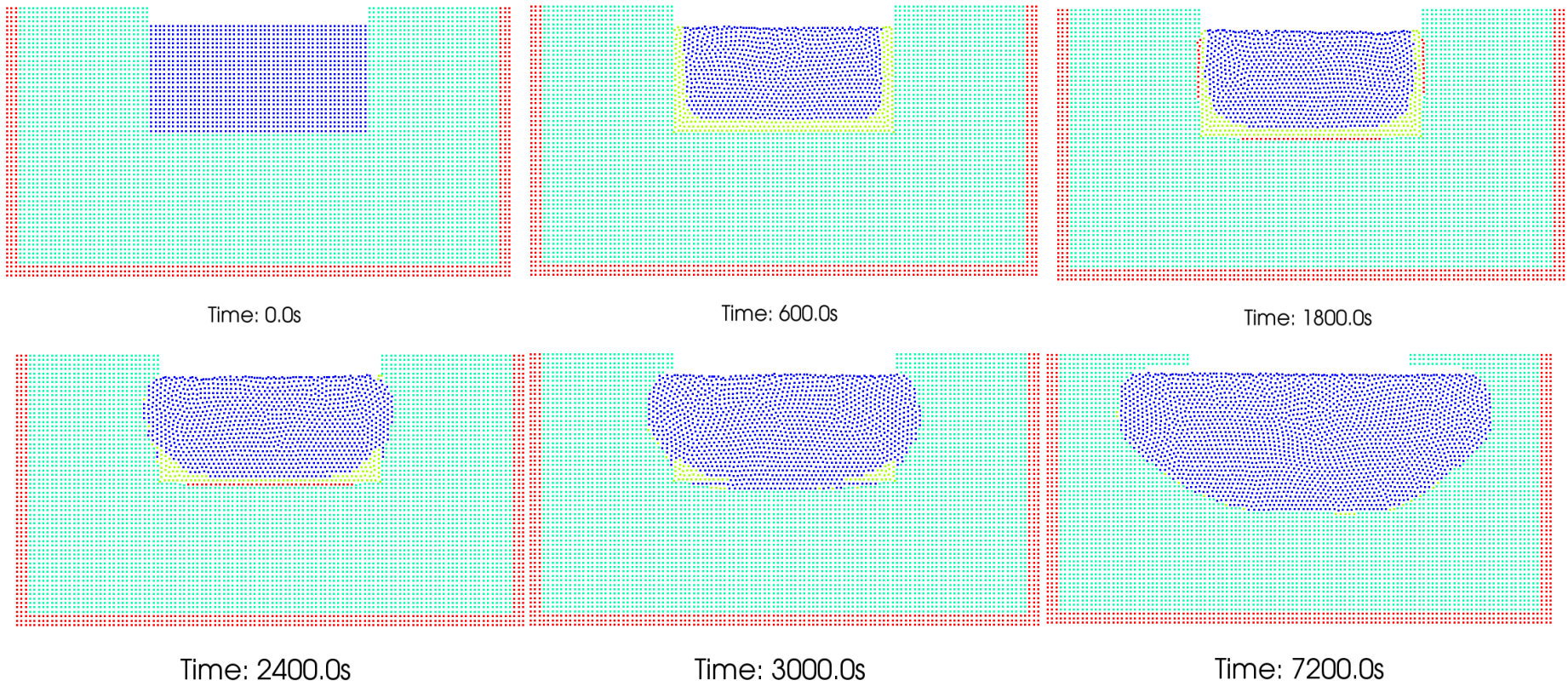
Figure 4-15. Ablation progress along the elapse time (Top: 0, 20, 30min; Bottom: 40, 50 120min).
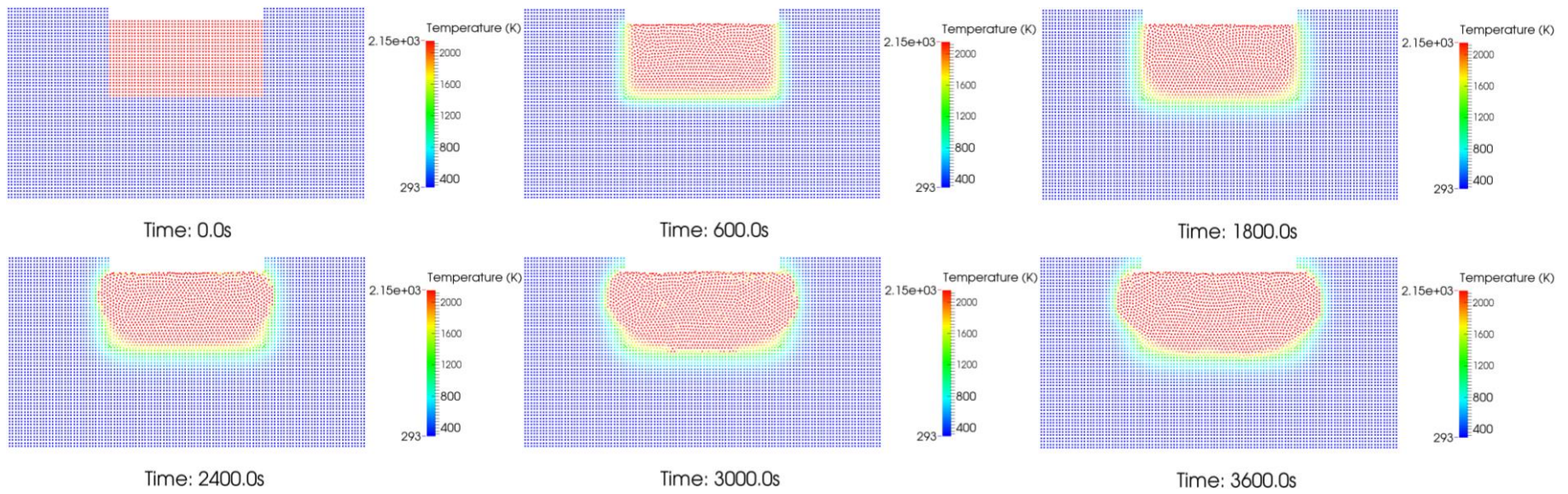
Figure 4-16. Temperature distribution along the elapse time (Top: 0, 20, 30min; Bottom: 40, 50 60min)
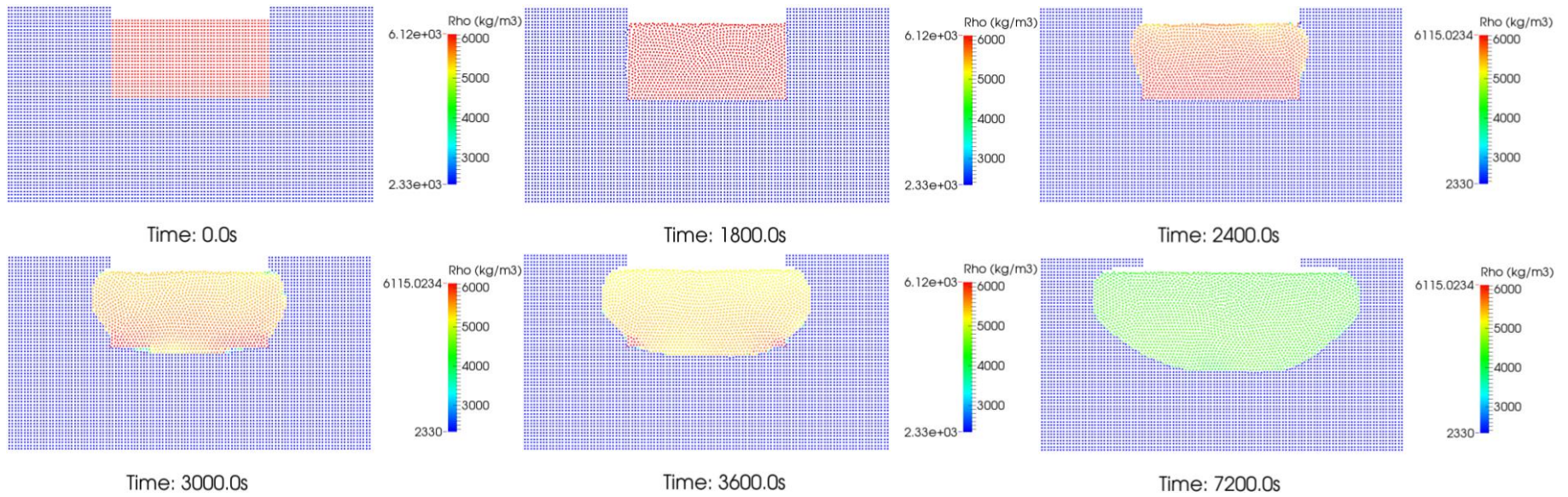
Figure 4-17. The density variation along the elapsed time (Top: 0, 30, 40 minutes; Bottom: 50, 60, 120 minutes)
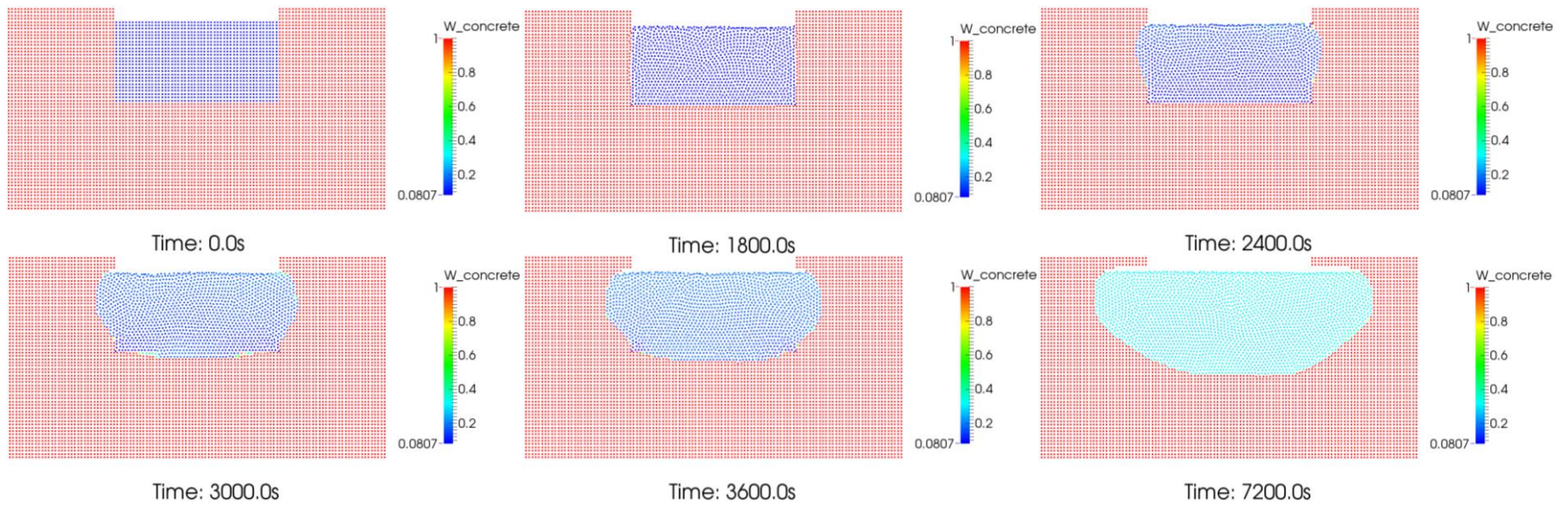
Figure 4-18. Concrete mass fraction variation along the elapsed time. (Top: 0, 30, 40 minutes; Bottom: 50, 60, 120 minutes)
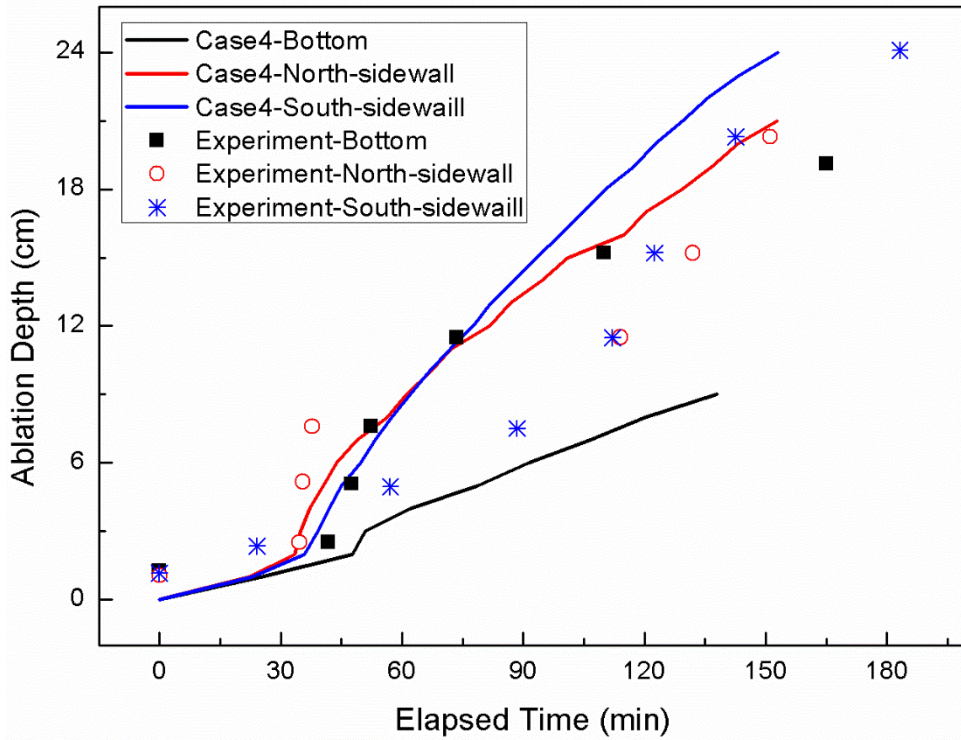
Figure 4-19. Ablation rate along the elapse time.
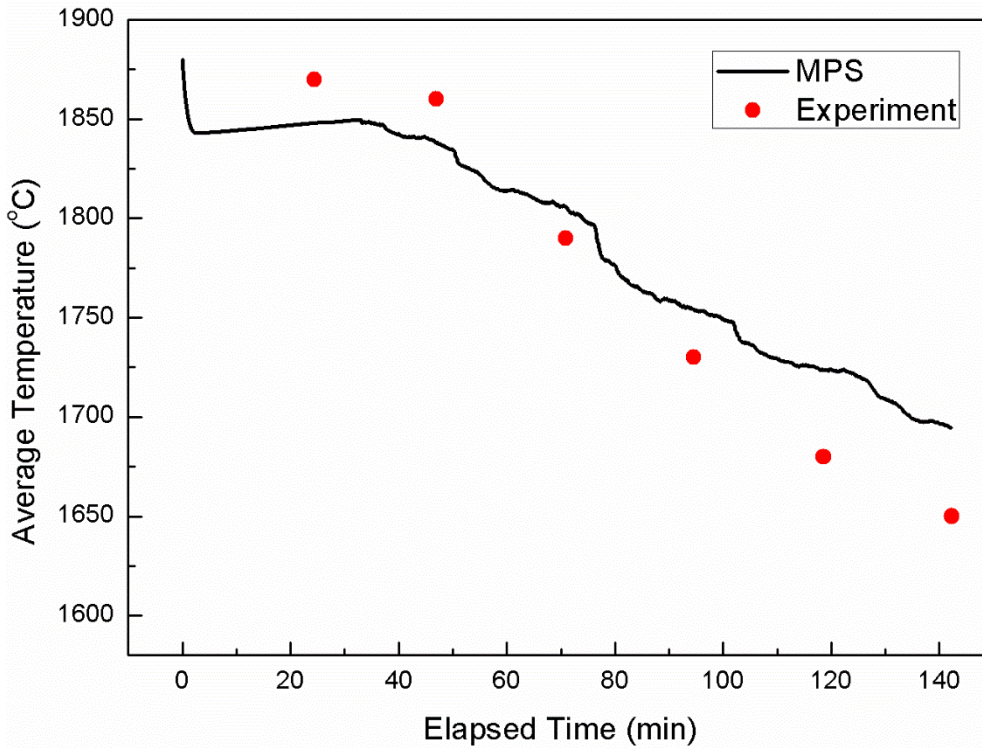
Figure 4-20. Average temperature of the melt pool (including the crust).

4.4.4.Discussion

➤ **Crust formation and break.**

Based on the simulation results, especially by comparing Case2 and Case3, the crust could be concluded as an important role during the ablation process. Due to the extreme experimental condition and the limitation of the measurement technique, the crust behavior cannot be studied very well. However in the simulation, it is very easy to visualize the crust profile through the whole experiment.

As shown in Figure 4-21(a), steady crust formed from the beginning of the experiment. With the concrete mixing into the corium, the crust will be formed harder and harder due to the decrease of the corium melting temperature. Thus, the maximum thickness of crust exists at the early stage of the process, which is 4cm at the bottom and 3cm at the sidewall. Because of the natural circulation, the crust at the bottom is thicker, more stable and harder to re-melt and break than that near the sidewall. As shown in Figure 4-21(b), the crust would be gradually re-melted by the inner source heat at 32min and 50min for sidewall and bottom, respectively.

(a)   (b)
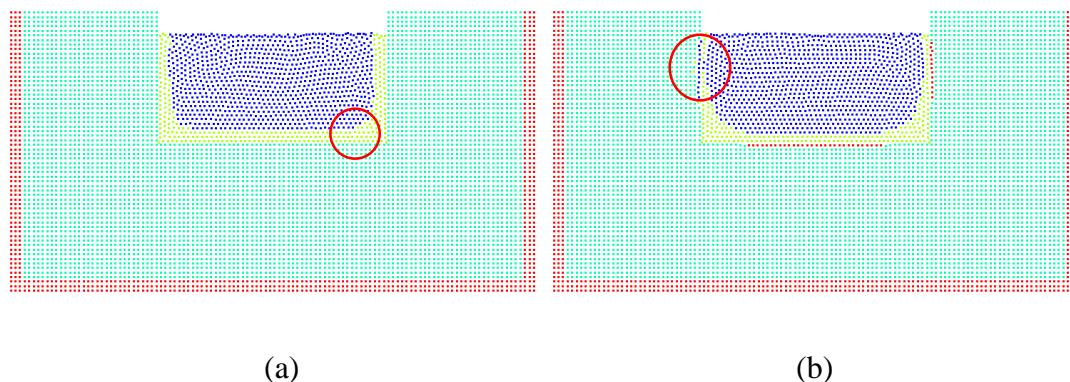
Figure 4-21. Crust thickness and breach.

➤ **Composition dependence corium solidus temperature**

As shown in Figure 1-2, the corium solidus temperature would be highly dependent on the concrete mass fraction of the mixture. The mixing process was not well predicted in the previous researches, so that this phenomena was not considered

because of the lack of concrete mass fraction calculation. Thus in this paper, composition dependence corium solidus temperature model was applied to simulate this phenomena. Figure 4-22 shows the concrete mass fraction of the corium in Case2. We can see from the picture that in Case2, the concrete mass fraction increases from 8.07% before the crust breach to about 30% at 135min. Meanwhile, the corium solidus temperature will changed depend on the concrete mass fraction. As shown in Figure 4-23, a rapid decrease appears after the crust breach, while the corium solidus temperature almost keep constant after the concrete mass fraction is larger than 30%.

Case1 was performed without the corium solidus temperature variation in order to validate the effect of the model. Figure 4-24 compare the ablation condition of both Case1 and Case2 at 45 minutes. Clearly, Case1 produced a thicker crust at the bottom compare to Case2 due to the higher melting temperature.
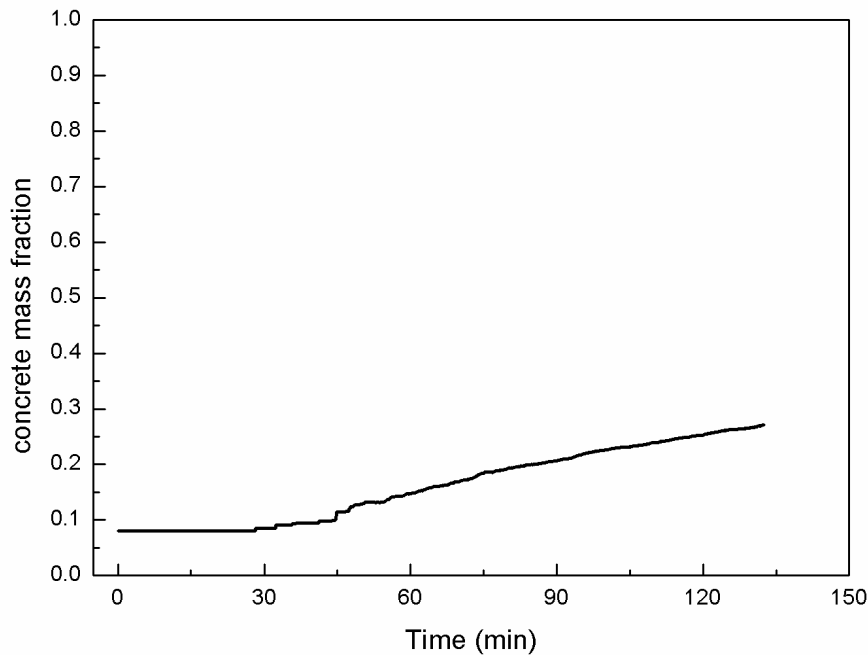
Figure 4-22. Concrete mass fraction in the melt pool.
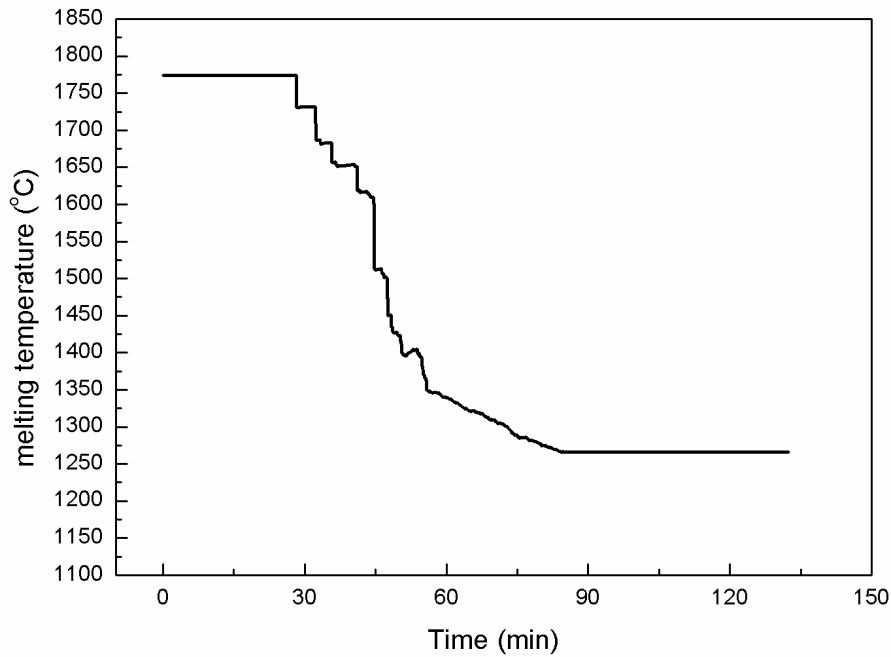
Figure 4-23. Corium melting temperature.

Case1   Case2
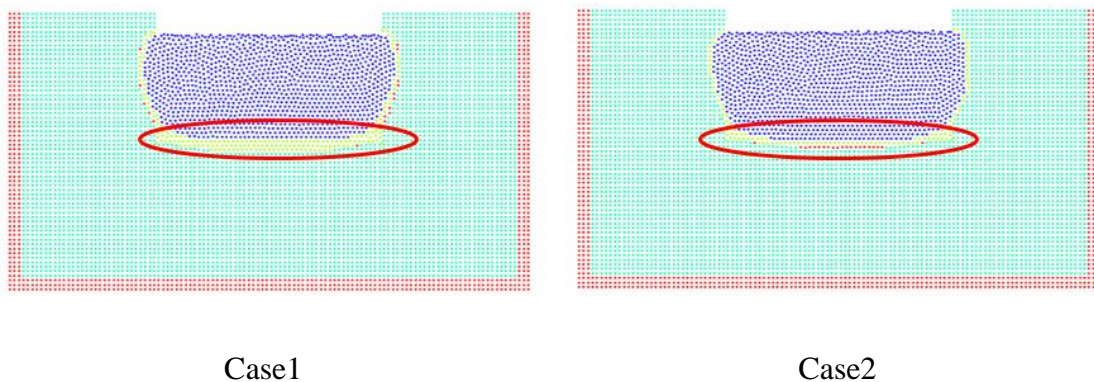
Figure 4-24. Ablation behavior at 45min.

Since crust plays an important role on the ablation behavior due to the thermal resistance, thus it is essential to consider the variation of the corium melting temperature against the changing of the concrete mass fraction.

➢ **A rapid erosion after the crust breach.**

Unlike the ablation circulation of crust generation and re-melt in Case2, a rapid erosion was observed after the crust breach in Case3. It can be seen from the Figure

4-25 that Case3 produced similar slow ablation profile at the first 30min. However, a quicker sidewall ablation compare to Case2 can be seen after that. Especially right after the crust breach, there is a rapid erosion took place. It is because the mass diffusion model was adopted in Case3, so that the liquid concrete particle would not become crust directly like Case2, but flow into the melt pool and gradually diffuse into the mixture. Therefore, as it shown in Figure 4-26, a solutal convection provided by these liquid concrete particles was formed near the sidewall interface. Hot corium particles would invade the liquid concrete domain and keep heating up the solid concrete. It is the reason why the rapid erosion occurs after the crust breach.
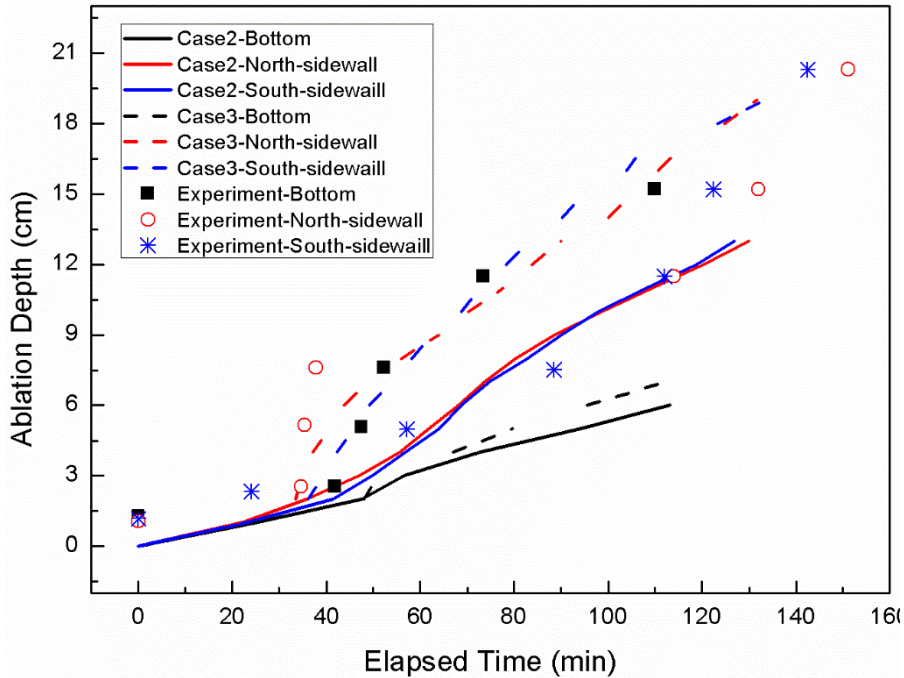
Figure 4-25. Ablation rate comparison between Case2, Case3 and experiment.
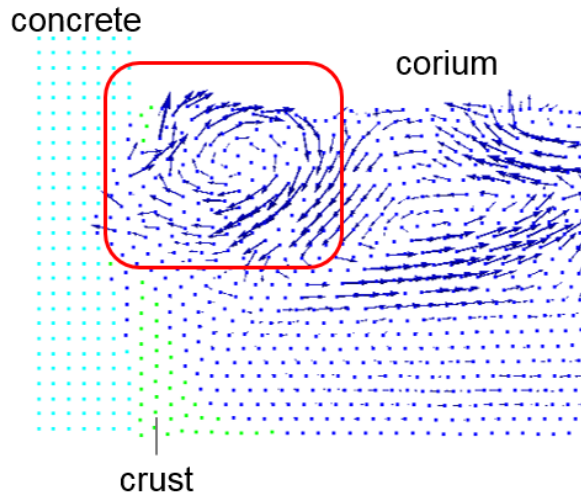
Figure 4-26. Solutal convection near the sidewall crust.

➤ Heat release from the chemical reaction

Figure 4-27 and Figure 4-28 comparing the results of Case3 and Case4 to discuss the effect of the heat release from the chemical reaction. Almost same ablation rate can be seen from Figure 4-27. A slight higher corium temperature was observed in Case4 compare to Case3 due to the thermal from the chemical reaction. It suggests that the heat released from chemical reaction plays a limited role compare to the inner source heat.
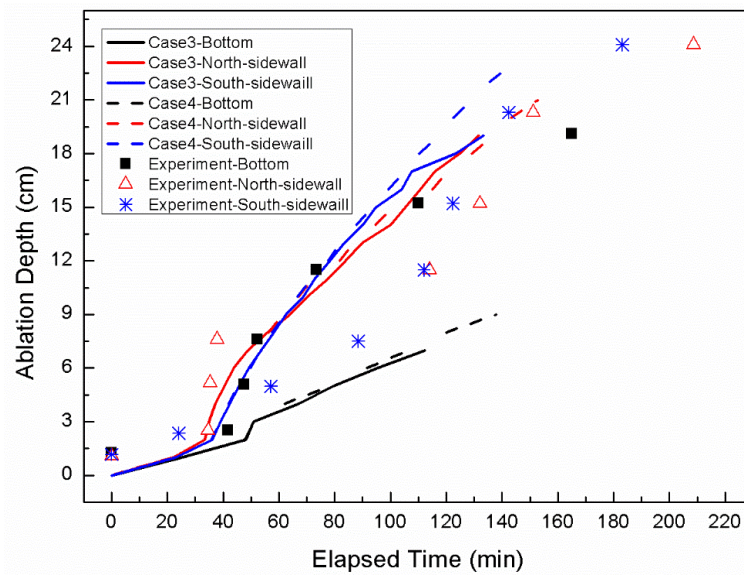
Figure 4-27. Ablation rate of Case3, Case4 and experiment.
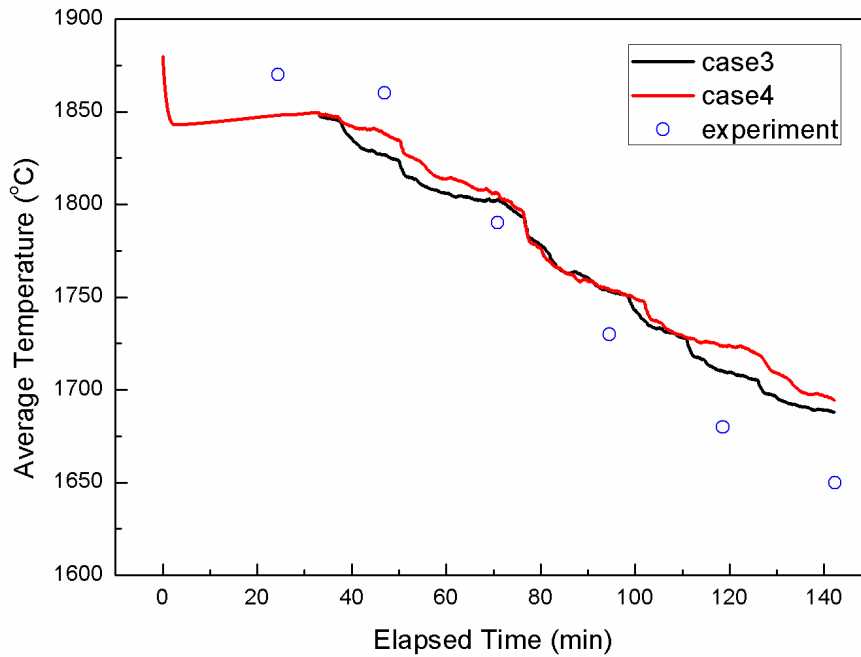
Figure 4-28. Average temperature of Case3, Case4 and experiment.

➢ **Gas generation and mixture stirring.**

As discussed above, steam and CO_2 would be generated from the liquid concrete and interact with the metallic materials in the melt pool and produce H_2 and CO. Figure 4-29 and Figure 4-30 shows the amount of the H_2 and CO released from the melt pool. As shown in Figure 31, these amount of gas bubbles would penetrate into the pool and enhance the stirring of the mixture. By comparing Case3 and Case4 (Figure 4-32), a slight more uniform mixture can be seen after implemented moving gas bubble model, which confirmed the stirring enhancement provided by the gas generation model. However, it also shows a under-estimated of the effect from the moving bubbles, which suggests the further improvement of the gas generation model.
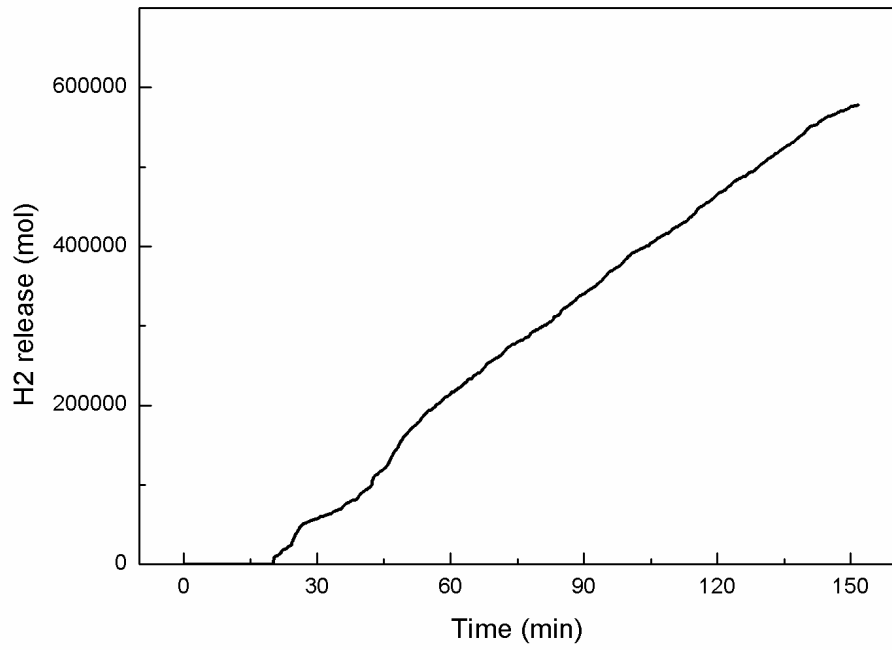
Figure 4-29. The amount of H2 released from the melt pool.
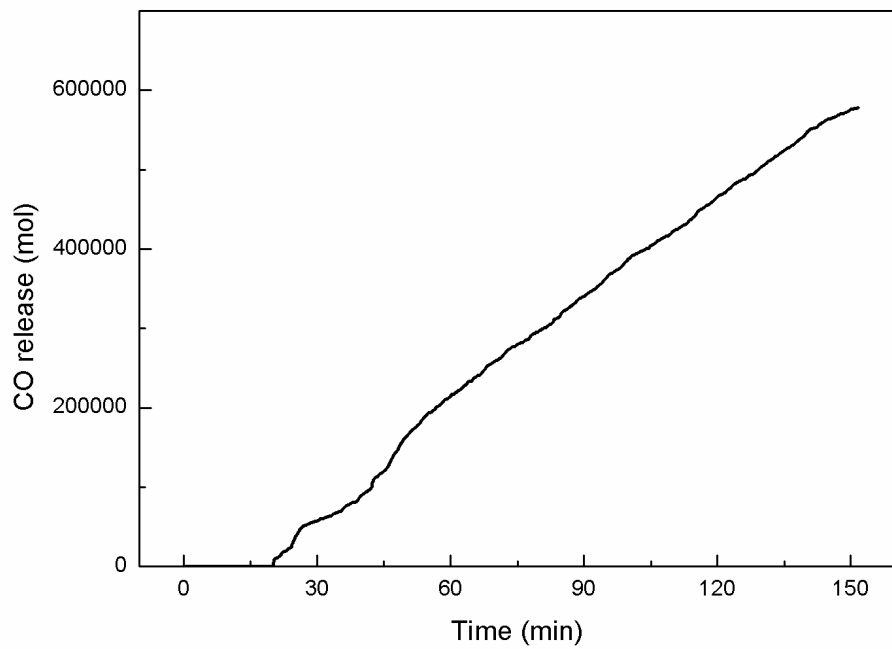
Figure 4-30. The amount of CO released from the melt pool.
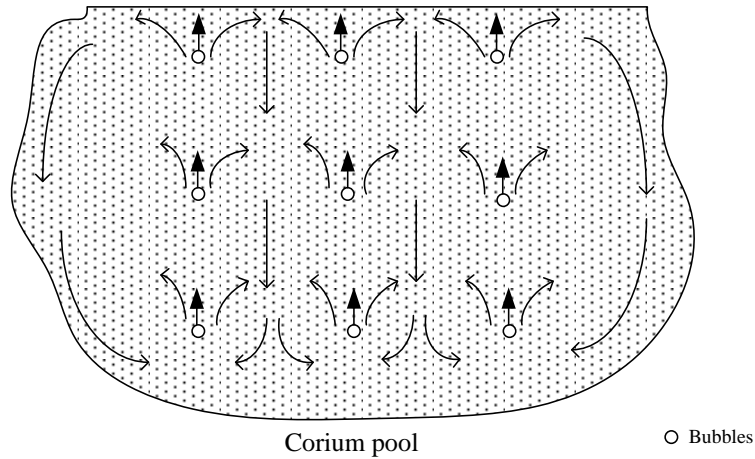
Figure 4-31. Stirring effect provided by the moving bubbles.
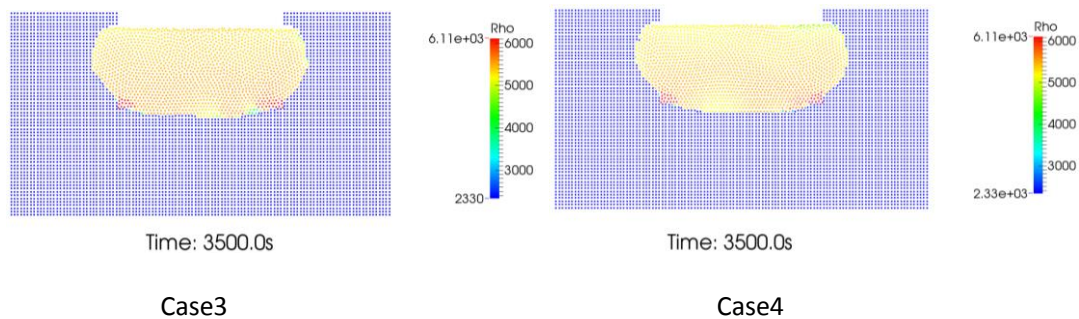
Figure 4.32. Comparison of stirring conditions between Case3 and Case4.

> **2-dimentional ablation.**

A good match with experimental results on North sidewall's ablation rate can be seen from the Figure4-19. Besides, the rapid erosion after the crust breach was confirmed in the simulation. Case2 shows a slower ablation due to the more thermal resistance provided by the crust.

On the other hands, similar rapid erosion as North sidewall was obtained from the simulation, which is not observed in the experiment. No stable crust formed in the South sidewall in the experiment, so that no liquid concrete can aggregate separately from the corium pool. Thus, it shows a gradually increase profile at the South wall in the experiment, which is closer to the Case2's condition.

For axial ablation, similar trend can be observed from the picture. Like north

sidewall, a rapid ablation is shown at around 40 minutes in the experiment. However, this time scale of crust breach in the simulation is much later than the experiment, which is around 51 minutes. The possible reason is the generated gases underneath the basemat crust. Since limestone concrete was applied in CCI-2 experiment, which has a big potential to generate the steam and carbon dioxide. Besides, the crust at the bottom is more stable than that at the sidewall due to the lower temperature caused by the natural convection. Thus, the generated bubble might aggregate in the enclosure between the crust and the solid concrete with big pressure inside and provide stress to the crust. Once the stress reach the limit, a possible volcano eruption may take place, which break the crust (depict in Figure 4-33). Unfortunately, the stress model is not included in this research. CCI-3[67] experiment may support this theory since siliceous concrete generate few gas bubbles and no crust breach was observed in the test.
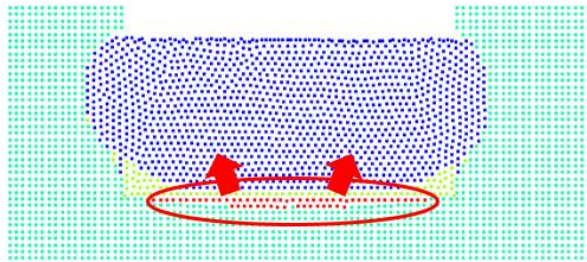
Figure 4-33. Curst break due to the stress from the gas below.

> **Corium composition.**

The corium composition varies with the concrete mix into the melt pool. By analyzing ten samples from the corium, the final constituent after the ablation can be shown in Table 4-6. We can see from the table that the concrete mass fraction increase from 8.07% at the beginning to 58.2% at the end (300min of dry cavity condition). as shown in the pictures of Figure 4-18, the concrete mass fraction also increases with the process proceed. Quantitatively, it increase to about 36.4% at 145min. This value is approaching the final data of the experiment.

Table 4-6. Corium constituent of both experiment and simulation

Constituent	Original (Wt%)	Eventually (Wt%) (experiment)	145min (Wt%) (simulation)
UO_2	60.97	27.5	63.6
ZrO_2	24.90	10.55	
Cr	6.41	3.75(including Cr_2O_3)	
Concrete	8.07	58.2	36.4

4.5.　　　Conclusion of the chapter

Conclusion of this chapter is mainly depart from two parts. One is the physical founding of MCCI process, while another part is the discussion about the effectivity of the multi-physics model.

1. In the dry cavity process, there is stable crust formed at the interface between both basemat and sidewall's surface from the beginning of the process. Based on the simulation results, the thickness of the crust under the CCI-2 experimental condition is maximum around 3cm near sidewall and 4cm at the bottom. The concrete underneath would be heated up by the crust and gradually melt in some position before the crust breach.

2. Due to the simulant decay heat inside, the corium is heated up and the crust is gradually melt. The time scale is about 30 min.

3. There is a rapid erosion around 30min in both experiment and simulation. From the simulation results, we could conclude that it is because the hot corium replaced the liquid concrete after the crust breach. This fit the explanation from the CCI experiment report.

4. Comparing Case1, Case2 shows a slight quicker ablation due to the less crust thermal resistance. Which suggests it is important to consider the change of

corium solidus temperature in the simulation. It should be considered in the other CFD code in the future.

5. By comparing Case2 and Case3, different ablation behaviors were obtained. In Case2, the mixing process is assumed to be infinity, which causes the direct conversion of liquid concrete particle into crust when they mix into the corium since their temperature is lower than the solidus temperature of the mixture. New crust will keep resisting the heat transfer between the corium and concrete, and the rapid erosion which is observed in the experiment will not be take place. Therefore, for MPS method, we can conclude the mass diffusion model is required for MCCI analysis.

6. By comparing Case3 and Case4, we can see the average temperature of the corium increased after insert chemical reaction model, which due to the thermal release from the redox reaction. However, it doesn't shows big differ on the ablation kinetic until the end of the simulation time. It suggest in this experiment, the chemical reaction heat release plays a limit role on erosion compare to the inside source power.

7. By the effect of gas rising, the mixture is much more stirred than before. However, more developed gas generation model is required in the future work.

8. The time scale for the sidewall crust breach match the experiment. However, it shows slower re-melt near the basemat. Combining the results of CCI-3 experiment, where siliceous concrete was utilized, the possible reason might be explained like this: The limestone concrete generate much more gas bubbles compare to siliceous concrete during the decomposition process, which pressurize the enclosure underneath the basemat crust. Once the pressure of the enclosure space reach the limit, an analogous eruption like volcano might take place, which breach the basemat crust. This theory can be supported by the CCI-3 experimental results, where have almost no axial ablation due to stable crust at the bottom. More evidence is required to confirm this theory

5. Conclusion and future work

5.1. Conclusion

Multi-physics models based on MPS method were developed to investigate the phenomena during the MCCI process. These models were validated against experiments in this paper. Based on the discussion from the previous chapters, we can mainly make the conclusion as following:

1. Heat transfer and phase change models were validated applicable for MCCI simulation by wax experiment. U-alloy and gel wax were used to emulate the molten metal and ablated materials. By comparing the simulation and experimental results, good match can be observed on the ablation behavior, deformation profile of the molten metal and the temperature history, which suggests that the MPS method may be a proper tool to calculate the heat transfer and phase change of the moving molten metal pool.

2. Natural convection model was validated by Tin and gallium experiments were simulated to discuss the natural convection behavior of in the case of MPS calculation. Although the perfect data can be obtained from pure heat conductive and low Rayleigh number natural circulation simulation, there is some Deviation on high Rayleigh number flow condition' simulation because of the possible reason of the limitation of particle size.

3. CCI-2 experiment is simulated with multi-physics models. Some phenomena observed from the experiment can be confirmed by the simulation. Specifically, it could be concluded like below:

➢ In the dry cavity process, there is stable crust formed at the interface between both basemat and sidewall's surface from the beginning of the process. The thickness of the crust is maximum around 3cm near sidewall and 4cm at the bottom. The concrete underneath would be heated up by the crust and gradually melt in some position before the crust breach.

➢ Due to the simulant decay heat inside, the corium is heated up and the crust is gradually melt. The time scale is about 30 min.

➢ There is a rapid erosion around 30min in both experiment and simulation. From the simulation results, we could conclude that it is because the hot corium invade the liquid concrete region (potential solutal convection) and keep heating up the solid concrete after the crust breach. This fit the explanation from the CCI experiment report.

4. Four cases with different models combinations were performed to discuss how the multi-physics models affect the ablation behavior. Based on the comparison of different cases, we can conclude that:

➢ An obvious thinner crust was observed after implemented the composition dependence corium solidus temperature due to the less thermal resistance, which suggests the importance of considering the variation of the corium solidus temperature in the MCCI simulation, even the other CFD code in the future.

➢ Totally different ablation behavior was obtained after considering the mass diffusion model. In Case2, the mixing process is assumed to be infinity, which causes the direct conversion of liquid concrete particle into crust when they mix into the corium since their temperature is lower than the solidus temperature of the mixture. New crust will keep resisting the heat transfer between the corium and concrete, and the rapid erosion which is observed in the experiment will not be take place. Therefore, for MPS method, we can conclude the mass diffusion model is required for MCCI analysis.

➤ The average temperature of the corium increased slightly after implemented the chemical reaction model, which due to the thermal release from the redox reaction. However, it doesn't shows big differ on the ablation kinetic until the end of the simulation time. It suggest in this experiment, the heat release from the chemical reaction plays a limit role on ablation behavior compare to the inner source heat. However, since almost all the uranium and zirconium were oxidized before the beginning in this experiment, which is somehow different from the real condition. Thus, additional research on the chemical reaction with more metallic materials is needed to discuss how the chemical reaction affect the ablation kinetics and thermal history during the MCCI process.

➤ By the effect of gas rising, the mixture is much more stirred than before. However, more developed gas generation model is required in the future work.

Besides, the time scale of the sidewall crust breach match the experiment. However, it shows slower re-melt near the basemat. Combining the results of CCI-3 experiment, we made a conjecture that it may due to the pressure provided by the gas release from the decomposed concrete was not considered in the simulation, but it may affect the crust condition since the limestone concrete has potential to produce more gas bubbles compare to siliceous concrete.

All in all, the multi-physics models based on MPS method were validated as a proper tool on investigating the MCCI phenomena. However, further improvement on chemical reaction and gas generation model were needed in the future.

5.2. Future work

The research resolved some issues of MCCI process by using multi-physics model. Most phenomena can be emulated in the calculation and results seems reasonable. However, it still have a lot of space to improve.

1. Although the gas generation is considered in this research, the model is too simple to simulate precisely. To specific, there are two field need to improve: 1) the gas movement in the liquid pool and the interactive force with liquid particles; 2) the stress of the crust due to the gas aggregate should be considered since it will affect the time of breach.

2. Due to the limitation of the extreme long simulation time, present calculation didn't reach the end of the experiment, but focus on the duration around the crust breach. The analysis of ablation behavior for a long term is required in the future.

3. In order to focus on the ablation behavior, present research is concentrating on the dry cavity condition. However, the flooding from the top is also important for the MCCI analysis, which need to be explored in the future.

Acknowledgement

Firstly, I would like to thank my supervisor Professor Okamoto for giving me an opportunity to do the doctor thesis at Okamoto Laboratory. The weekly meetings with them along with the regular feedbacks played a very important role towards completion of the thesis. His constant encouragement even at difficult times was something which I am really thankful for.

I am also greatly thank Dr. Ishiwatari to give me the opportunity to come here as the Ph.D student. He helped me a lot and give me the confidence for the research, especially in the first year after I arrived.

I am highly grateful for the help from Dr. Erkan and Dr. Kondo. When I have obstacle, they can always give me some very good suggestions to resolve the problems. Without them, I could not finished my experiment and simulation under the schedule.

Finally, I would also like to express my highest gratitude to other members of Okamoto Laboratory. Without their help, I finish my work smoothly and enjoy the life in Japan.

References

1. M. Nie, "Temporary melt retention in the Reactor Pit of the European Pressurized water Reactor (EPR)," Doctoral Thesis, University of Stuttgart, 2004.

2. Chemical reaction and equilibrium software with extensive thermochemical database. [Online].

3. C. Spengler, H.-J. Allelein, M. Cranga, F. Duval, and J.-P. V. Dorsselaere, "Assessment and Development of Molten corium concrete interactino models for the integral code ASTEC," 2005.

4. Z.P.Bazant and M.F.Kaplan, "Concrete at High Temperatures: Material Properties and Mathematical Models," Essex: Longman Group ISBN 0-582-08626-4, 1996.

5. H. Alsmeyer et al, "Molten corium/concrete interaction and corium coolability - A state of the art report," European Commission Report EUR 16649, 1995.

6. D.H. Thompson, M.T. Farmer, J.K. Fink, D.R. Armstrong, B.W. Spencer, and Compilation, "analysis and interaction of ACE Phase C and MACE experimental data," Argonne National Laboratory, Chicago, IL, USA Report ACEX TRC-14, 1997.

7. M.T.Farmer, B. W. Spencer, D. J. Kilsdonk, and W. Aeschlimann, "Status of large scale MACE Core Coolability experiments," presented at the OECD Workshop on Ex-Vessel Debris Coolability, Karlsruhe, Germany, 1999.

8. E. R. Copus, "Sustained Uranium dioxide Concrete interaction tests: The SURC test series, 2nd OECD (NEA) Spec. Mtg. on Molten Core DebrisdConcrete Interactions," Karlsruhe1992.

9. E. R. Copus, R. E. Blose, J. E. Brockmann, R. B. Simpson, and D. A. Lucero, "Core-Concrete Interactions using Molten UO2 with Zirconium on a Basaltic Basemat: The SURC-2 Experiment," Sandia Nat. Lab, United States Report NUREG/CR-5564, 1990.

10. D.H. Thompson, M.T. Farmer, J.K. Fink, D.R. Armstrong, B.W. Spencer, and Compilation, "Core-Concrete Interactions Using Molten Urania With Zirconium on a Limestone Concrete Basemat, The SURC-1 Experiment," Sandia National Lab1992.

11. R. E. Blose, D. A. Powers, E. R. Copus, J. E. Brockmann, and R. B. Simpson, "Core- Concrete Interactions with Overlying Water Pools - The WETCOR-1 Test," Sandia Nat. Lab, U.S.A. Report NUREG/CR-5907, SAND92-1563, 1993.

12. M.T.Farmer, S.Lomperske, and D.J.Kilsdonk, "OECD MCCI Project 2-D Core Concrete Interaction (CCI) Tests: Final Report," Argonne National Laboratory2006.

13. Y. Maruyama, Y. Kojima, M. Tahara, H. Nagasaka, M. Kato, A. A. Kolodeshnikov, *et al.*, "A study on concrete degradation during molten core/concrete interactions," *Nuclear Engineering and Design,* vol. 236, pp. 2237-2244, 10// 2006.

14.   H. Alsmeyer, T. Cron, B. Fluhrer, G. Messemer, A. Miassoedov, S. Schmidt-Stiefel*, et al.*, "The COMET-L3 Experiment on long-term melt-concrete interaction and cooling by surface flooding," 2006.

15.   G.Sdouz, R.Mayrhofer, H.Alsmeyer, T.Cron, B.Fluhrer, J.J.Foit*, et al.*, "The COMET-L2 experiment on long-term MCCI with steel melt," 2006.

16.   H.Alsmeyer, A. Miassoedov, M.Cranga, R.Fabianelli, I.Ivanow, and G.Doubleva, "The

COMET-L1 experiment on long-term concrete erosion and surface flooding," presented at the NURETH, France, 2005.

17.   M. T. Farmer, S. W. Lomperski, and S. Basu, "The Results of the CCI-3 Reactor Material ExperimentInvestigating 2-D Core-Concrete Interaction and Debris Coolability with a Siliceous Concrete Crucible,"   Advanced Nuclear Power Plants (ICAPP' 06), 2006.

18.   C. Journeau, P.Piluso, and J.F.Haquet, "Behaviour of nuclear reactor pit concretes under severe accident conditions," presented at the CONSEC' 07, France, 2007.

19.   J.M.Veteau, "Experimental investigation of interface conditions between oxidic melt and ablating concrete during MCCI by means of simulating material experiments: the Artemis program," presented at the NURETH-11, Avignon, France., 2005.

20.   T. Sevón, T. Kinnunen, J. Virta, S. Holmström, T. Kekki, and I. Lindholm, "HECLA experiments on interaction between metallic melt and hematite-containing concrete," *Nuclear Engineering and Design,* vol. 240, pp. 3586-3593, 10// 2010.

21.   M. Cranga, R. Fabianelli, F. Jacq, M. Barrachin, and F. Duval, "The MEDICIS code, a versatile tool for MCCI modelling," presented at the ICAPP, Seoul, KOREA.

22.   B. SPINDLER and E. DUFOUR, "Simulation of CCI-2 test with TOLBIAC-ICB: modelling and sensitivity studies," presented at the MCCI Project Seminar 2007, Cadarache, 2007.

23.   B. Spindler, K. Atkhen, M. Cranga, J. J. Foit, M. Garcia, W. Schmidt*, et al.*, "Simulation of Molten Corium Concrete Interaction in a Stratified configuration: the COMET-L2–L3 Benchmark," 2007.

24.   M.T.Farmer, S.W.Lomperski, and S.Basu, "The results of the CCI-2 reactor material experiment investigating 2-D core-concrete interaction and debris coolability," presented at the NURETH-11, Avignon, France, 2005.

25.   J.M.Bonnet, "Thermal hydraulic phenomena in corium pools for ex-vessel situations: the BALI experiment," presented at the ICONE8, Baltimore, USA, 2000.

26.   S.S.Kutateladze and I.G.Malenkov, "Boiling and bubbling heat transfer under the conditions of free and forced convection," presented at the 6th International Heat Transfer Conference, Toronto, 1978.

27.   G.A.Greene and T. F. Irvine, "Heat transfer between stratified immiscible liquid layers driven by gas bubbling across the interface," presented at the ANS Proceedings of the National Heat Transfer Conference, Houston, 1988.

28. H.Werle, "Enhancement of heat transfer between two horizontal liquid layers by gas injection at the bottom," *Nuclear Technology,* vol. 59, pp. 160-164, 1982.

29. B.Tourniaire, J.M.Seiler, and J.M.Bonnet, "Study of the mixing of immiscible liquids: results of the BALISE experiments," presented at the NURETH-10, Seoul, Korea, 2003.

30. S.Koshizuka and Y.Oka, "Application of Moving Particle Semi-implicit Method To Nuclear Reactor Safety," *Advanced Methods for Conputational Fluid Dynamics,* vol. 9, pp. 366-375, 2001.

31. R. E. Blose, J.E.Gronager, A.J.Suo-Anttila, and J.E.Brockmann, "SWISS: Sustained Heated Metallic Melt/Concrete Interactions with Overlying Water Pools," 1987.

32. X. Li and Y. Oka, "Numerical simulation of the SURC-2 and SURC-4 MCCI experiments by MPS method," *Annals of Nuclear Energy,* vol. 73, pp. 46-52, 11// 2014.

33. V.Strizhov, V.Kanukova, and T.Vinogradova, "An Assessment of the CORCON-MOD3 Code Part I: Thermal-Hydraulic Calculations," Office of Nuclear Regulatory Research U.S., Washington, DC1996.

34. S. Koshizuka, A. Nobe, and Y. Oka, "Numerical Analysis of Breaking Waves Using the Moving Particle Semi-implicit Method," *INTERNATIONAL JOURNAL FOR NUMERICAL METHODS IN FLUIDS,* vol. Meth. Fluids 26, pp. 751-769, 1998.

35. S. Koshizuka and Y. Oka, "Moving-particle Semi-implicit Method for Fragmentation of Incompressible Fluid," *Nuclear Science and Engineering,* vol. 123, pp. 421-434, 1996.

36. T. SAKAI and H. GOTOH, "LAGRANGIAN SIMULATION OF BREAKING WAVES USING PARTICLE METHOD," *Coastal Engineering Journal,* vol. 41, pp. 303-326, 1999.

37. T. W. H. Sheu, C. Chiao, and C. Huang, "Development of a Particle Interaction Kernel Function in MPS Method for   Simulating Incompressible Free Surface Flow," pp. 1-16, 2011 2011.

38. K. M. K. F. N. S. Shuai Zhang, "SIMULATION OF THE INCOMPRESSIBLE FLOWS WITH THE MPS METHOD " *13th International Conference on Nuclear Engineering* vol. 13-50166, May 16-20, 2005 2005.

39. R. Chen and Y. Oka, "Numerical analysis of freezing controlled penetration behavior of the molten core debris in an instrument tube with MPS," *Annals of Nuclear Energy,* vol. 71, pp. 322-332, 9// 2014.

40. W. Tian, Y. Ishiwatari, S. Ikejiri, M. Yamakawa, and Y. Oka, "Numerical computation of thermally controlled steam bubble condensation using Moving Particle Semi-implicit (MPS) method," *Annals of Nuclear Energy,* vol. 37, pp. 5-15, 1// 2010.

41. R. Chen, Y. Oka, G. Li, and T. Matsuura, "Numerical investigation on melt freezing behavior in a tube by MPS method," *Nuclear Engineering and Design,* vol. 273, pp. 440-448, 7/1/ 2014.

42. K. Shibata, S. Koshizuka, M. Sakai, and K. Tanizawa, "Lagrangian simulations of ship-wave interactions in rough seas," *Ocean Engineering,* vol. 42, pp. 13-25, 3// 2012.

43. S. Koshizuka, H. Ito, R. Shino, T. Okura, I. Morito, and T. Kikuchi, "Moving Particle Simulation for Medical Application " presented at the APCOM & ISCM, Singapore 2013.

44. T. Kawahara and Y. Oka, "Ex-vessel molten core solidification behavior by moving particle semi-implicit method," *Journal of Nuclear Science and Technology,* vol. 49, pp. 1156-1164, 2012/12/01 2012.

45. H. Ikeda, S. Koshizuka, Y. Oka, H. S. Park, and J. Sugimoto, "Numerical Analysis of Jet Injection Behavior for Fuel-Coolant Interaction using Particle Method," *Journal of Nuclear Science and Technology,* vol. 38, pp. 174-182, 2001/03/01 2001.

46. S. Koshizuka, H. Ikeda, and Y. Oka, "Numerical analysis of fragmentation mechanisms in vapor explosions," *Nuclear Engineering and Design,* vol. 189, pp. 423-433, 5/11/ 1999.

47. F. D. PIN, "A Lagrangian Approach based on the Natural Neighbor Interpolation," 2000.

48. M. Kondo, S. Koshizuka, K. Suzuki, and M. Takimoto, "Surface Tension Model Using Inter-Particle Force in Particle Method," presented at the ASME/JSME 2007 5th Joint Fluids Engineering Conference, San Diego, California, USA, 2007.

49. A. P. A. Mustari and Y. Oka, "Molten uranium eutectic interaction on iron-alloy by MPS method," *Nuclear Engineering and Design,* vol. 278, pp. 387-394, 10/15/ 2014.

50. A. P. Andi Mustari, Y. Oka, M. Furuya, W. Takeo, and R. Chen, "3D simulation of eutectic interaction of Pb–Sn system using Moving Particle Semi-implicit (MPS) method," *Annals of Nuclear Energy,* vol. 81, pp. 26-33, 7// 2015.

51. T. G. Theofanous, M. Maguire, S.Angelini, and T.Salmassi, "The first results from the ACOPO experiment.," *Nuclear Engineering and Design,* vol. 169, pp. 49-57, 1997.

52. J. M.Bonnet and J.M.Seiler, "Thermal hydraulic phenomena in corium pools: The BALI experiment," presented at the 7th International Conference on Nuclear Engineering, Tokyo, Japan., 1999.

53. V. Asmolov, N. N.Ponomarev-Stepnoy, V.Strizhov, and B. R.Sehgal, "Challenges left in the area of in-vessel melt retention," *Nuclear Engineering and Design,* vol. 209, pp. 87-96, 2001.

54. L. Zhang, Y. Zhou, Y. Zhang, W. Tian, S. Qiu, and G. Su, "Natural convection heat transfer in corium pools: A review work of experimental studies," *Progress in Nuclear Energy,* vol. 79, pp. 167-181, 3// 2015.

55. S. Zhang, K. Morita, K. Fukuda, and N. Shirakawa, "An improved MPS method for numerical simulations of convective heat transfer problems," *International Journal for Numerical Methods in Fluids,* vol. 51, pp. 31-47, 2006.

56. J.P.Holman, *Heat Transfer*, 2010.

57. J. Stefan, "S.B. Wien Akad," *Mat.Natur.,* vol. 98, 1889.

58. F. Neumann, "Die Paruellen," *Differentialgleichungen der Mathematischen Physik,* vol. vol 2, 1912.

59. G. De Vahl Davis, "Natural convection of air in a square cavity: A bench mark numerical solution," *International Journal for Numerical Methods in Fluids,* vol. 3, pp. 249-264, 1983.

60. P. W. Cleary, "Modelling confined multi-material heat and mass flows using SPH," *Applied Mathematical Modelling,* vol. 22, pp. 981-993, 12// 1998.

61. M. Akgün, O. Aydın, and K. Kaygusuz, "Experimental study on melting/solidification characteristics of a paraffin as PCM," *Energy Conversion and Management,* vol. 48, pp. 669-678, 2// 2007.

62. N. Ukrainczyk, S. Kurajica, and J. Šipušiæ, "Thermophysical Comparison of FiveCommercial ParaffinWaxes as Latent Heat StorageMaterials," *Chemical & Biochemical Engineering Quarterly,* vol. 24, 2009.

63. L. Yuanyuan and C. Xiaoming, "Review on the low melting point alloys for thermal energy storage and heat transfer applications," *Energy Storage Science and Technology,* vol. 2, pp. 189-198, 2013.

64. F. Wolff, C. Beckermann, and R. Viskanta, "Natural convection of liquid metals in vertical cavities," *Experimental Thermal and Fluid Science,* vol. 1, pp. 83-91, 1// 1988.

65. C.Gau and R.Viskanta, "Melting and Solidification of a Pure Metal on a Vertical Wall," *Journal of Heat Transfer-transactions of The Asme,* vol. 108, 1986.

66. Stefan and X.Cheng, "Title," unpublished|.

67. M. T. Farmer, S. Lomperski, D. J. Kilsdonk, R. W. Aeschlimann, and S. Basu, "OECD/MCCI 2-D Core Concrete Interaction (CCI) tests : final report February 28, 2006," OECD/MCCI-2005-TR05; TRN: US1102884 United States10.2172/1014855TRN: US1102884Thu Jun 23 07:34:53 EDT 2011ANLENGLISH, 2011.

68. U. Schneider, "Concrete at high temperatures — A general review," *Fire Safety Journal,* vol. 13, pp. 55-68, 4/7/ 1988.

69. V.G.Asmolov, V.N.Zagryazkin, E.V.Astakhova, V.Vishnevskii, D'yakokE.K, A.Yu.Kotov, *et al.*, "The Density of UO2–ZrO2 Alloys," *High Temperature,* vol. 41, pp. 627-632, 2003.

70. I. N. S. Center. Thermal Conductivity and Diffusivity of Liquid UO_2. [Online].

71. I. N. S. Center. Enthalpy and Heat Capacity of Liquid UO_2 [Online].

72. R.O.Gauntt, R.K.Cole, C.M.Erickson, R.G.Gido, R.D.Gasser, S.B.Rodriguez, *et al.*, "MELCOR Computer Code Manuals," Sandia National Laboratories2000.

73. M. Epstein, "Thermal Hydraulics of Molten Core–Concrete Interactions: A Review and Comparison of Heat Transfer Models with Data, Interpretation of Rheologigal Data, and a Theory for the Onset of Concrete Spallation," Palo Alto: Electric Power Research Institute1998.